SYSTEM DEVELOPMENT AND CLINICAL APPLICATIONS OF THE HANDHELD PA/US DUAL MODE IMAGING SYSTEM

A Dissertation
Presented to
The Academic Faculty

by

Lingyi Zhao

In Partial Fulfillment
of the Requirements for the Degree
Doctor of Philosophy in the
School of College of Engineering

Georgia Institute of Technology and Emory University
August 2020

COPYRIGHT © 2020 BY LINGYI ZHAO

SYSTEM DEVELOPMENT AND CLINICAL APPLICATIONS OF THE HANDHELD PA/US DUAL MODE IMAGING SYSTEM

Approved by:

Dr. Changhui Li, Advisor
Department of Biomedical Engineering
Peking University

Dr. Meng Yang
Department of Ultrasonography
Peking Union Medical College Hospital

Dr. Stanislav Emelianov
Department of Biomedical Engineering
Georgia Institute of Technology and Emory University

Dr. Jianwen Luo
Department of Biomedical Engineering
Tsinghua University

Dr. Peng Xi
Department of Biomedical Engineering
Peking University

Date Approved: June 14th, 2020

Acknowledgements

I would like to express my deep and sincere gratitude to my research advisors, Dr. Changhui Li, from Peking University and Dr. Stanislav Emelianov, from Georgia Institute of Technology for their patient guidance and full support in my pursuit of a doctorate degree. Dr. Changhui Li's vision, consideration, and preciseness have deeply inspired me from the first day of graduate study. He has taught me the methodology to research from scratch and helped me cultivate priceless rigorous habits. During my study at Georgia Institue of Technology, I have been highly motivated by Dr. Stanislav Emelianov's productivity, generosity, and critical thinking. With his help, I have learned how to present research works clearly and have gained a valuable mindset of independent thinking. It was a great privilege and honor to work and study under Dr. Changhui Li and Dr. Stanislav Emelianov's guidance. I am incredibly grateful for what they have offered me.

I exceptionally appreciate my collaborators: Dr. Meng Yang from Peking Union Medical College Hospital and Dr. Fang Yang from Mindray Medical International Limited. Their efforts are indispensable for the clinical studies presented in this thesis. I appreciate the opportunity to participate in clinical studies together with them. In these clinical studies, I am lucky enough to get closer to doctors and patients, and as a result, learn their challenges at first hand.

I am genuinely thankful to Dr. Tao Han, Wenzhao Li, Guangjie Zhang, Chenyao Wen, Dr. Zijian Deng, Dr. Ning Wu, Dr. Kaiye Xia, Dr. Xiaoyi Zhu, Guangjie Zhang, Chenyao Wen from Peking University, for their full support during the completion of the thesis and during the years in Peking University.

I sincerely appreciate the guidance provided by Don Vanderlaan, Dr. Jingfei Liu, Dr. Andrei Karpiouk, Dr. Yiying Zhu, Dr. Heechul Yoon, Dr. Kristina Hallam, Dr. V.S. Jisha, and Dr. Kelsey Kubelic from Georgia Institute of Technology. Without them, my research in Atlanta would not go so smoothly.

I want to thank my venerable collaborators from Peking Union Medical Colledge Hospital, including but not limited to Dr. Yuxin Jiang, Dr. Ming Wang, Dr. Na Su, Dr. Hewen Tang, Chenyang Zhao, Rui Zhang, for their enthusiastic participation in clinical studies presented in this thesis. As doctors in one of the best hospitals in China, they have to utilize their break time to conduct clinical research most of the time. I genuinely appreciate their dedication.

I am extending my thanks to all those people and institutions who helped in every aspect of the thesis, especially Jialei Luo from Peking University and Kristen M Laquidara from Georgia Institute of Technology. For financial support, I would like to thank the National

Natural Science Foundation of China, National Institutes of Health, China Scholarship Council, and Friends of Bobby Jones Fund. Furthermore, I want to thank my joint Ph.D. program for providing me such a unique and enjoyable experience.

Finally, I would like to say thanks to my family. I am incredibly grateful to my parents, who fully support me as ever for the past five years. Their love, caring, and sacrifices deeply move me. I enjoyed their company so much while writing this thesis. I am very thankful to my husband, Dr. He Wang, for his love, understanding, and continuing support to complete this research work. He keeps enlightening me with his wisdom in every aspect of my graduate life. With his company in the past five years, life is full of sweetness.

TABLE OF CONTENTS

ACKNOWLEDGEMENTS ..... **iii**

LIST OF TABLES ..... **viii**

LIST OF FIGURES ..... **ix**

LIST OF SYMBOLS AND ABBREVIATIONS ..... **xii**

SUMMARY ..... **xiii**

Chapter 1 Clinical Translational Studies of Photoacoustic Imaging **1**

1.1 The mechanism of PAI **1**

1.1.1 Generation of PA signals 2

1.1.2 PA wave equation 3

1.1.3 Propagation of light and PA signals in tissue 6

1.1.4 Clinical applications of PAI 8

1.2 Clinical PAI systems **9**

1.2.1 Clinical PAI systems based on straight linear arrays 10

1.2.2 Clinical PAI systems based on curved linear arrays 17

1.2.3 Clinical PAI systems based on volumetric arrays 21

1.2.4 Current challenges of clinical PAI systems 26

1.3 The outline of this thesis **29**

Chapter 2 PA/US Dual Modality Imaging Based on Handheld Clinical Ultrasound **31**

2.1 PA/US dual mode imaging system **31**

2.2 Phantom study for validation of the PA/US imaging ability of the system **38**

2.3 In vivo study on the forearm of a healthy adult **40**

2.4 Summary **45**

Chapter 3 Optical Fluence Compensation for Handheld PA/US Dual Modality System **46**

3.1 Introduction to the optical fluence compensation for PAI **46**

3.2 Optical fluence compensation on tissue mimicking phantom **49**

3.3 A preclinical study with the optical fluence compensation applied **56**

3.4 Summary and discussion **63**

Chapter 4 An Initial Clinical Study of Thyroid Cancer with Handheld PA/US Imaging

system **66**
4.1 Background **66**
4.2 System setup **68**
4.3 Patients enrollment and PA/US imaging procedure **69**
4.4 Preclinical study results **70**
4.5 Summary and discussion **75**

Chapter 5 3D PA/US Functional Imaging of Breast Cancers **78**
5.1 Background **78**
5.2 3D PA/US functional imaging system **81**
5.3 Quantification analysis strategy **86**
5.4 Patients enrollment and imaging procedure **88**
5.5 Statistical analysis **89**
5.6 Results **91**
5.6.1 Statistical results 91
5.6.2 PA/US imaging results 95
5.7 Summary and discussion **98**

Chapter 6 A Comparison between Surface Acoustic Waves Induced by Laser and by ARF **104**
6.1 Background **104**
6.2 Materials and methods **106**
6.3 Results **113**
6.4 Summary and discussion **120**

Chapter 7 Conclusion **122**
7.1 The major novelties of this thesis **124**
7.2 The future of PA/US dual mode imaging in clinical applications **126**

Appendix A.1 ..... **128**
Detailed information of 24 breast tumors **128**

References **129**

LIST OF TABLES

Table 2.1	Detailed information of our PA/US dual mode imaging system	32
Table 2.2	Detailed information of our 3D PA/US imaging system	43
Table 3.1	Comparison of PA values before and after compensation	55
Table 3.2	Comparison of PA values before and after compensation	62
Table 4.1	The clinical information, comparison between PAI and CDFI, and histology results	73
Table 5.1	Tumor size and correspondent sample size	91
Table 6.1	Detailed information of the imaging system	112

LIST OF FIGURES

Figure 1.1	The PA waves detected by a point detector	6
Figure 1.2	Schematic diagram of the PA/US dual mode transducer by Seno Medical Inc	12
Figure 1.3	Schematic diagram of the dual-mode PA and US imaging system developed by Garcia-Uribe et al	13
Figure 1.4	Photographs of the components of the PA/US system developed by Irisawa K et al	14
Figure 1.5	The PA/US probe showing the light delivery window developed by Pim J. van den Berg et al	16
Figure 1.6	Photograph of the handheld MSOT probe and schematic diagram of MSOT scanning breast tissue	18
Figure 1.7	Schematic diagram of PAI on Crohn's disease	19
Figure 1.8	Co-registered total hemoglobin and US images of a benign mucinous cystadenoma and a high-grade serous carcinoma	21
Figure 1.9	Schematic diagram of the photoacoustic mammoscope by Twente University	23
Figure 1.10	PAM-03 system developed by Canon Inc	24
Figure 1.11	SBH-PACT system developed by Li Lin et al	25
Figure 1.12	Photograph of the clinical hand-held MSOT system	26
Figure 1.13	Configuration of the hybrid PA/US imaging probe suggested by Xosé Luís Dean-Ben et al	27
Figure 1.14	Schematic diagram of slit-based system suggested by Yuehang Wang et al	28
Figure 2.1	Schematic diagram of the PA/US dual mode imaging system	32
Figure 2.2	Customized fiber head to match the size of the probe	33
Figure 2.3	Schematic diagram of the PA/US dual mode transducer	34
Figure 2.4	The ultrathin white film made from TiO_2 particles	35
Figure 2.5	System setup for measurement of illumination area	36
Figure 2.6	Illumination area of the fiber bundle on the front side of the probe	37
Figure 2.7	Work flow of data acquisition for PA/US dual mode imaging	38
Figure 2.8	System setup for phantom study with the 2D PA/US imaging system	39
Figure 2.9	Dual-modality imaging results of a carbon rod hanged in intralipid solution with different orientation angles	40
Figure 2.10	Imaging results of human forearm cutaneous vein with longitude section and transverse sections	42

Figure 2.11	Photograph of the 3D imaging device	44
Figure 2.12	The photograph of the 3D PA/US functional imaging system	44
Figure 3.1	The schematic diagram of imaging setup and three layers for optical fluence compensation study	50
Figure 3.2	The schematic of the imaging system for the phantom study	51
Figure 3.3	The shapes of two layers of the phantom with intra lipid added were assumed to be two cuboids in COMSOL simulation	52
Figure 3.4	Optical fluence rate map of the central cut plane in phantom study of optical fluence compensation	54
Figure 3.5	PA images of phantom without and with optical fluence compensation	55
Figure 3.6	Schematic of breast tissue in COMSOL simulation	58
Figure 3.7	Relative fluence rate map at the central cut plane in breast imaging	60
Figure 3.8	Relative fluence rate along the dark dotted line in Fig3.7	61
Figure 3.9	PAI results of a healthy breast with and without optical fluence compensation	62
Figure 3.10	PA/US dual mode imaging results of a healthy breast with and without optical fluence compensation	63
Figure 4.1	Schematic diagram and photograph of the PA/US dual mode imaging system	69
Figure 4.2	Imaging results from a healthy right thyroid	71
Figure 4.3	Imaging results from a left lobe papillary thyroid cancer	72
Figure 4.4	Imaging results from a right lobe PTC with the largest diameter of 13 mm	72
Figure 4.5	Imaging results from a left lobe papillary thyroid cancer	73
Figure 5.1	Spectra of Hb and deHb between 700 nm and 900 nm	82
Figure 5.2	Energy-wavelength curve of the OPO laser	83
Figure 5.3	3D PA/US dual mode imaging system and 3D scanning device	83
Figure 5.4	Design of 3D imaging device in SOLIDWORKS	84
Figure 5.5	Schematic diagram of 3D scanning device and 3D rendering of vascular networks co-registered with the tumor surface	85
Figure 5.6	Representation for definitions of tumor and tumor surrounding regions	88
Figure 5.7	Flow chart of the imaging procedure	89
Figure 5.8	Box plots of volumetric mean SO_2 values of the benign, normal and malignant groups in tumor regions and tumor surrounding regions	91
Figure 5.9	ROC for differentiating malignant tumors from benign tumors by varying the SO_2 threshold in both tumor regions and tumor surrounding regions	93

Figure 5.10	Vascular density in tumor regions and tumor surrounding regions	94
Figure 5.11	2D SO_2/US imaging results of an invasive breast cancer and a breast fibroadenoma	95
Figure 5.12	X-ray mammography results of the same invasive breast cancer and breast fibroadenoma as in Figure 5.7	96
Figure 5.13	3D vascular networks of the same invasive breast cancer and breast fibroadenoma as Fig5.11 showed	97
Figure 5.14	Average SO_2 variation curve within different slices of a malignant tumor	102
Figure 6.1	The system setup for the first experiment, where the imaging target was a rubber phantom with graphite powder inside to provide optical absorption	107
Figure 6.2	System setup for the third experiment	111
Figure 6.3	Combined US (grayscale map) and PA image of the tissue-mimicking gelatin phantom	113
Figure 6.4	Displacement maps at four different time points obtained using ultrafast US imaging for laser induced SAWs and ARF-based SAWs	113
Figure 6.5	SWV measurements (n=4) in gelatin phantoms of different gelatin concentrations and, therefore, different degrees of stiffness	115
Figure 6.6	Displacement-time curves and spectrums of SAWs at 2.5 mm and 3.3 mm away from laser/ARF excitation region	116
Figure 6.7	Imaging results of the phantom with a photoaborber located 3.3 mm below the surface	118

LIST OF SYMBOLS AND ABBREVIATIONS

US	ultrasound
PA	photoacoustic
CDFI	color Doppler flow imaging
PAI	photoacoustic imaging
SO_2	oxygenation saturation
Hb	oxygenated hemoglobin
deHb	deoxygenated hemoglobin
SAW	surface acoustic wave
ARF	acoustic radiation force

SUMMARY

As an emerging technology, photoacoustic (PA) imaging (PAI) has gained lots of progresses in the past two decades. By combing optical contrast with ultrasound detection, PAI can maintain high spatial resolution in deeper regions. Furthermore, with the aid of multispectral imaging, PAI can reveal functional information such as oxygenation saturation (SO_2), which is closely related to tumor malignancy. With the above advantages, nowadays PAI has gained lots of progresses in clinically translatable research. These research shows that PAI has the potential to complement existing imaging techniques such as ultrasound (US) imaging for cancer detection, disease evaluation and prognosis monitoring.

This thesis mainly discusses the clinical application of PAI, including system design and clinical research. Particularly, it presents several studies including the development of PA/US imaging system and the clinical evaluation of PA/US imaging in diagnosis of superficial cancer. The main research results and the major novelties of this thesis include:

1) The collaborative development of the PA/US imaging system for clinical studies, where the author was mainly responsible for the design of optical path and the trigger method between the laser and the US system.
2) The design of optical fluence compensation strategy based on clinical US structural imaging. This strategy first identifies the tissue type based on US structural imaging,

and then utilizes the known optical absorption and scattering parameters to simulate optical fluence map in the imaging region. The simulated optical fluence map can then be used for correction of original PA images. The effectiveness of this strategy has been verified based on clinical PAI data. The proposed method can improve the accuracy of quantification PAI and restore PA signals in deeper regions.

3) The collaborative study of PA/US imaging on thyroid nodules with the self-developed 2D PA/US handheld imaging system. By comparing PAI results with color Doppler flow imaging (CDFI) results from 10 thyroid nodules, we found that PAI can reveal more abundant vessels than CDFI, and can thus provide valuable information in diagnosis of thyroid cancer.
4) The design of the method for quantification analysis of 3D PA/US imaging on breast cancer. Specifically, this method first calculates the ellipse enclosing the tumor region with the minimum volume and then automatically segments the tumor regions and tumor surrounding regions. Next, the volumetric mean SO_2 of tumor regions and tumor surrounding regions were calculated for quantification analysis. Our results demonstrate that quantification analysis of 3D functional PA/US imaging on breast cancers has the potential to improve the specificity in diagnosis of breast cancer.

In Chapter 1, the mechanism of PAI and its recent clinical translational progresses are

first reviewed. Next, in Chapter 2, the development of a clinical PA/US imaging system based on handheld US imaging is presented. The imaging ability of the newly developed system was verified with the phantom study as well as the in vivo study. After then, in Chapter 3, the optical fluence compensation method for handheld PA/US imaging based on tissue structural information provided in US imaging is introduced. The clinical result demonstrates that important tissue structures such as vessels in deeper tissue can be restored after fluence compensation based on the proposed method. Chapter 4 and Chapter 5 introduce the clinical studies based on the self-developed PA/US imaging systems, including 2D PA/US imaging of thyroid nodules, 3D PA/US imaging of breast cancer, and quantification analysis of the imaging results. The quantification analysis demonstrates that 3D functional PA/US imaging has the potential to improve the diagnosis specificity of breast cancer.

In Chapter 6, the author presented the research conducted in Georgia Institute of Technology. In this chapter, the laser induced surface acoustic waves (SAWs) and acoustic radiation force (ARF) induced SAWs were compared. The results demonstrate that laser-induced SAW imaging is able to perform stiffness evaluation and has the potential to provide higher spatial resolution.

In Chapter 7, the author summarized the major novelties in this thesis and discussed research directions in the future work.

CHAPTER 1 CLINICAL TRANSLATIONAL STUDIES OF PHOTOACOUSTIC IMAGING

Since late 1990s, the photoacoustic (PA) imaging (PAI) has evolved into a clinically translatable imaging platform. PAI can not only provide both functional and molecular information, but also allow noninvasive soft-tissue characterization. PAI is being translated into the clinic with various clinical studies underway, including imaging of breast, joints, prostate, and ovarian, and it has the potential to complement existing imaging techniques such as ultrasound (US) for detecting cancer, characterization of diseases, prognosis and treatment monitoring. In this chapter, the mechanism of PAI is introduced. Then, several PAI systems as well as typical clinical applications are reviewed and discussed.

1.1 The mechanism of PAI

Photoacoustic effect was first introduced by Alexander Graham Bell in late 1800s[1]. However, it was until 1990s that PAI gains much progress owing to the development in laser, ultrasound detection and computer technologies. Studies have been carried out exploring this mechanism for clinical purposes since then[2-4]. Typically, nanosecond pulsed laser light is used to irradiate biological tissues, in which some tissue constituents absorb light and cause thermal expansion. The thermal expansion will then generate ultrasound waves (also called PA waves) which propagate outwardly from the absorber and can be detected by ultrasound transducers.

PA image can be reconstructed based on appropriate algorithms[2,5,6]. Because the PA wave is ultrasound that has a much lower scattering coefficient in the soft tissue, PAI allows deeper tissue imaging while at the same time provides optical contrast which is closely related to inherent molecular information.

1.1.1 Generation of PA signals

On laser excitation, the fractional volume expansion dV/V can be expressed as[2]:

$$\frac{dV}{V} = -\kappa p + \beta T \tag{1.1}$$

In this equation, κ represents for the isothermal compressibility; β represents for the thermal coefficient of volume expansion; p and T represent for small changes in pressure (Pa) and temperature (K), respectively. For the typical short laser pulse, the following two conditions are generally met: 1) the thermal confinement; 2) the stress confinement. Equation (1.2) describes the thermal confinement, where τ is the laser pulse width, d_c is the characteristic dimension of the heated region, and α_{th} is the thermal diffusivity (m^2/s). The stress confinement is described in Eq. (1.3), where v_s is the speed of sound.

$$\tau < \tau_{th} = \frac{d_c^2}{\alpha_{th}} \tag{1.2}$$

$$\tau < \tau_s = \frac{d_c}{v_s} \tag{1.3}$$

If the laser pulse width meets both of the thermal and stress confinements, the fractional

volume expansion is negligible ($dV \approx 0$ in Eq. (1.1)) and the local pressure change p_0 after the laser pulse can be rewritten as the following equation:

$$p_o = \frac{\beta T}{\kappa} \tag{1.4}$$

For soft tissue, κ is about $5 \times 10^{-10} Pa^{-1}$, and β is about $4 \times 10^{-4} K^{-1}$. p_0 is thus linearly related to T. Temperature rise T caused by optical absorption can be derived from

$$T = \frac{\eta_{th} A_e}{\rho C_V} \tag{1.5}$$

where A_e is the specific optical absorption (J/m^3), C_V is the specific heat capacity at constant volume, and η_{th} is the percentage of the absorbed energy converted to heat. Given the definition of Grüeneisen parameter (Eq. (1.6)), Eq. (1.4) can then be rewritten as Eq. (1.7).

$$\Gamma = \frac{\beta}{\kappa \rho C_V} \tag{1.6}$$

$$p_o = \Gamma \eta_{th} A_e \tag{1.7}$$

Given $A_e = F \times \mu_a$, where F is the optical fluence (J/m^2), and μ_a is the optical absorption coefficient, Eq. (1.7) becomes Eq. (1.8):

$$p_o = \Gamma \eta_{th} \mu_a F \tag{1.8}$$

1.1.2 PA wave equation

In an infinite and inviscid medium, the PA wave generation and propagation can be

described by the following wave equation[2]:

$$\left(\nabla^2 - \frac{1}{v_s^2}\frac{\partial^2}{\partial t^2}\right) p(\boldsymbol{r}, t) = -\frac{\beta}{C_P}\frac{\partial H(\boldsymbol{r},t)}{\partial t} \tag{1.9}$$

The right-hand side of this equation represents the source term and the left-hand side of this equation describes the wave propagation. $p(\boldsymbol{r}, t)$ is the acoustic pressure at location $\boldsymbol{r}$ and time t. C_p is the specific heat capacity at constant pressure. $H(\boldsymbol{r}, t)$ is the heating function defined as the thermal energy converted per unit volume and per unit time. As shown in Eq. (1.10), H is related to the η_{th}, the optical absorption coefficient μ_a, and the optical fluence rate Φ.

$$H = \eta_{th}\mu_a\phi \tag{1.10}$$

It's worth noticing that the PA source term in Eq. (1.9) is the time derivative of $H(\boldsymbol{r}, t)$, indicating that only time-variant heating can produce a US pressure wave.

The wave equation can be solved by using a Green function approach[2]. The Green function in an infinite homogeneous and non-viscous medium is as follows:

$$\left(\nabla^2 - \frac{1}{v_s^2}\frac{\partial^2}{\partial t^2}\right) G\left(\boldsymbol{r}, t; \boldsymbol{r}', t'\right) = -\delta(\boldsymbol{r} - \boldsymbol{r}')\delta(t - t') \tag{1.11}$$

where $\boldsymbol{r}'$ and t' represent for the source location and time, respectively. In an infinite space,

the solution of Eq. (1.11) is:

$$G(\boldsymbol{r},t;\boldsymbol{r}',t') = \frac{\delta(t-t'-\frac{|\boldsymbol{r}-\boldsymbol{r}'|}{v_s})}{4\pi|\boldsymbol{r}-\boldsymbol{r}'|} \tag{1.12}$$

With the above Green function, the PA wave equation can then be solved as Eq. (1.13)

$$p(\boldsymbol{r},t) = \frac{\beta}{4\pi C_p}\frac{\partial}{\partial t}\int d\boldsymbol{r}'\frac{1}{|\boldsymbol{r}-\boldsymbol{r}'|}H(\boldsymbol{r}',t-\frac{|\boldsymbol{r}-\boldsymbol{r}'|}{v_s}) \tag{1.13}$$

For a short pulse width which is within the acoustic stress confinement, the heating process can be treated approximately as Dirac delta function[7] as the following equation:

$$H(\boldsymbol{r}',t') \approx p_0(r')/\Gamma \times \delta(t') \tag{1.14}$$

Substituting the above equation into Eq. 1.13, $p(\boldsymbol{r})$ can be rewritten as Eq. (1.15):

$$p(\boldsymbol{r},t) = \frac{1}{4\pi v_s^2}\frac{\partial}{\partial t}[\frac{1}{v_s t}\int d\boldsymbol{r}' p_0(\boldsymbol{r}')\,\delta(t-\frac{|\boldsymbol{r}-\boldsymbol{r}'|}{v_s})] \tag{1.15}$$

This expression denotes that the detected pressure at $\boldsymbol{r}$ and time t comes from sources over a spherical shell which has a radius of $v_s t$ and is centered at $\boldsymbol{r}$ (Fig1.1).

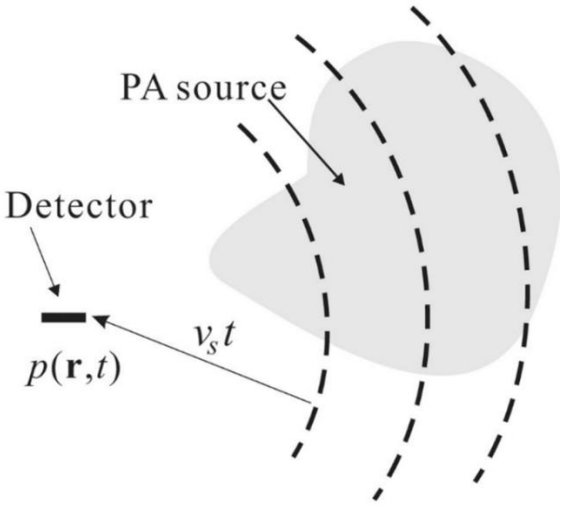

Fig1.1 The PA waves detected by a point detector at a certain time t come from sources over a spherical shell centered at the detector position and a radius of $v_s t$.[7]

1.1.3 Propagation of light and PA signals in tissue

In tissue, light propagation is related to the scattering coefficient μ_s, the absorption coefficient μ_a, the anisotropy factor g, as well as the light wavelength. It can be modeled by the radiative transfer equation (RTE)[2]. In general, RTE does not have an exact analytical solution but can be solved by numerical calculation, including Monte Carlo simulations and other modeling methods based on different ways of diffusion approximation[2]. For the strongly scattering medium, such as the living tissue, the reduced scattering coefficient $\mu_s' = (1-g)\mu_s$ is a more appropriate parameter instead of the scattering coefficient. With planar illumination, the equation of the fluence rate in a uniform diffusive medium is as follows:

$$\Phi(z) \approx \Phi_0 e^{-\mu_{eff} z} \tag{1.16}$$

where ϕ_0 is the illumination fluence, z is the depth, and $\mu_{eff} = \sqrt{3\mu_a(\mu_a + \mu_s')}$. Based on Eq. (1.16), the absorption of the tissue plays an important role in the transportation depth. According to the absorption spectra of tissue components such as water, blood and melanin[8], the near infrared (NIR) light generally penetrates much deeper than visible light.

Different from light propagation, which suffers from strong scattering during propagation, PA waves (acoustic waves) have much lower scattering effects which are almost negligible in soft tissue. However, at high frequencies or in highly heterogeneous tissue such as the skull, the attenuation and wave distortion effect cannot be ignored. Besides, because the ultrasound attenuation coefficient increases with frequency, PAI systems detecting higher frequency ultrasound signals always have shallower detection depth.

Due to the attenuation of both light and ultrasound, compensations are usually important especially for quantitative PAI. In addition, since PA signals have a broad bandwidth, it is also important to choose acoustic detectors with appropriate detection bandwidth.

PAI is a scalable imaging modality, with the imaging depth varying from micrometers to centimeters. In general, the shallower the imaging depth is, the higher the spatial resolution can reach. For instance, the photoacoustic microscopy can image blood capillaries, but at the depth less than 1 mm. In this thesis, we focus on the PAI clinical applications for deep tissues, i. e., targets locating at about 1 cm or deeper in depth.

1.1.4 Clinical applications of PAI

The optical absorption is closely related to the molecular structure of chromophores. Therefore, PAI has great potential for molecular imaging. The PA signal is directly correlated with the concentrations of the chromophores such as melanin, hemoglobin, fat, water, etc. Except for melanin in the skin, hemoglobin dominates the absorption in tissue due to its high optical absorption coefficient and concentration, and thus becomes the endogenous target of most PAI studies. In addition, the oxygenated hemoglobin (HbO_2) and de-oxygenated hemoglobin (Hb) have a very different absorption behavior, so the oxygenation saturation (SO_2) which represents for the concentration ratio of HbO_2 to the total hemoglobin can be determined by using multiple PA illumination wavelengths. It is known that SO_2 is very important for clinical diagnosis especially for cancer detection. For instance, a tumor with lower SO_2 is considered more likely cancerous due to cancer's hypoxic hallmark[9,10]. PAI has potential to provide this important physiological parameter to enhance the diagnostic accuracy in differentiating malignant tumors from benign ones[11]. In addition to the endogenous tissue contrast, PAI also has other advantages such as nonionizing, ease of integration into clinical US imaging systems, as well as affordability. By complementing existing imaging techniques such as US imaging, PAI can play an important role in the diagnosis of diseases[6].

1.2 Clinical PAI systems

Clinical PAI systems are mainly composed of three elements: lasers, ultrasonic transducer (UST) array system, as well as data acquisition/processing systems. Because both the bulk absorption and scattering coefficients of tissue are low in the NIR region, light within this region can penetrate deeper into tissue[12]. Therefore, the NIR pulsed lasers with the wavelengths ranging from 650 to 1100 nm are commonly used. In addition, specific wavelengths can be chosen for imaging specific components such as endogenous photo-absorbers including hemoglobin, water, fat and exogenous photo-absorbers such as methylene blue[13,14]. In practice, to have enough laser power with satisfied spatial resolution, lasers with short pulse width less than 100 nanoseconds are commonly employed. These lasers normally can output high pulse energy (several tens to hundreds of mJ/pulse at 700-1,100 nm) to achieve a high signal-to-noise ratio (SNR)[6]. However, the pulse repetition rates (PRFs) of these lasers are usually several tens of Hz, limiting the frame rate of PAI. Besides, high-powered lasers are expensive and bulky. Alternatively, small laser diodes and light emitting diodes (LEDs) also have the potential to be used as the excitation source for PAI of shallower regions (such as skin) because they have high PRFs of several kHz, which allow signals to be averaged by multiple times to improve the SNR[15,16]. In terms of UST arrays, the linear array is most commonly used in clinical PAI systems, including both straight and curved linear arrays[17]. Moreover, for acquiring 3D PA images, volumetric arrays can be used with the aid of parallel

processing and beamforming technologies[18]. Due to the inherent similarities, some existing commercially available US systems can be modified for laser integration, PA beamforming and PA display to become a clinical PAI system[19]. To acquire PA signals from multiple transducers, multi-channel parallel data acquisition systems need to be employed[13,20,21].

In the following sections, the clinical PAI systems with three types of imaging array including straight linear arrays, curved linear arrays, and volumetric arrays are introduced.

1.2.1 Clinical PAI systems based on straight linear arrays

The combination of PAI with handheld linear arrays attracts lots of interest these years due to its ability to perform conventional US imaging and PAI simultaneously. Due to the light penetration limitation, handheld PA/US systems generally use the linear arrays with frequencies ranging from 5 MHz to 20 MHz, which are usually used in clinical ultrasound imaging for small and shallow structures including blood vessel, breast, and thyroid. In this section, PAI systems with straight linear arrays for multiple clinical applications including detecting breast cancer[11,14], fine needle aspiration biopsy of sentinel lymph nodes[14] and evaluating arthritis[15,22] are reviewed. In these systems, handheld US probes are usually combined with angled optical fiber bundles placed along two sides of US probe. The angles between fiber bundles and the transducers are adjusted so that the two light beams coming out of the two optical fibers can converge at a desired depth below the transducer. Depending on

the imaging targets and depths, the center frequency of the transducer in these platforms varies as well.

The clinical study of PA/US imaging enrolling the most human subjects was carried out by Neuschler et al[11]. This clinical study aimed at exploring the diagnostic value of PA/US imaging on breast cancers. Over two thousand subjects with breast tumors were enrolled for PA/US imaging in multiple study centers. US imaging was carried out independently with PA/US imaging. Traditional Breast Imaging Reporting and Data System (BI-RADS) grading was performed first, followed by independent PA scores grading. The system used in this study (Seno Medical, San Antonio, TX, USA) can perform both stand-alone gray-scale US imaging and dual mode PA/US imaging. A 128-element transducer with a one-to-two fiber bundle placed along the probe was used for dual mode imaging, as shown in Fig1.2 (a). This system used two wavelengths: 757 nm and 1064 nm, provided by an Alexandrite laser and a 1064 nm Nd: YAG laser respectively. The functional information including relative concentration of total hemoglobin and SO_2 calculated from PAI at these two wavelengths were color-coded and shown overlaid with US imaging. To compare the diagnostic efficiency with the stand-alone US imaging, five PA scores including vessel score, blush score, hemoglobin score, boundary zone score, peripheral zone score were graded independently by seven physicians (Fig1.2 (b)). The comparison between BI-RADS grading and PA scoring shows that PA/US exceeds US by 14.9% (43.0% versus 28.1%) in specificity.

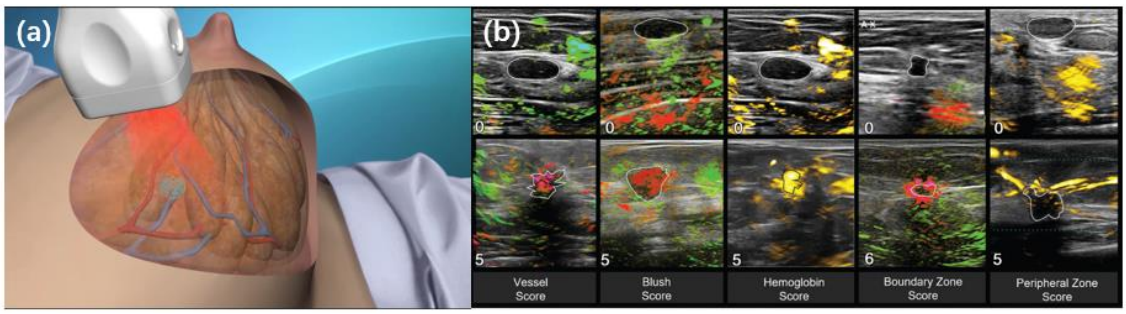

Fig1.2 (a) Schematic diagram of the PA/US dual mode transducer; (b) Examples of minimum and maximum scores for each PA feature. The top row is an example of the lowest score in each category and the bottom row is an example of the highest score in each category.[11]

Alejandro Garcia-Uribe et al. proposed a method using PA/US imaging to guide fine needle aspiration biopsy of a sentinel lymph node for staging of breast cancers[14]. In their study, a modified clinical US system (iU22, Philips Healthcare) and two straight linear arrays (L12-5 and L8-4, Philips Healthcare) were used for acquisition of PA/US signals (Fig1.3 (a)). A tunable laser (PrecisionScan-P, Sirah, Kaarst, Germany) pumped by an Nd: YAG laser (QuantaRay PRO-350-10, Spectra-Physics, Santa Clara, CA) was employed to provide 667 nm laser pulse with a pulse duration of 6.5 ns at a repetition rate of 10 Hz. 1064 nm laser pulse was provided directly by an Nd: YAG laser. As seen in Fig1.3 (b)i-ii, at 650 nm wavelength, PA signals came from both methylene blue inside lymphatic vessels as well as other blood vessels, while at 1064 nm wavelength, PA signals only came from blood vessels. By taking the fractional change, the methylene blue was highlighted (Fig1.3 (b)iii), and as a result, the imaging specificity for methylene blue was improved.

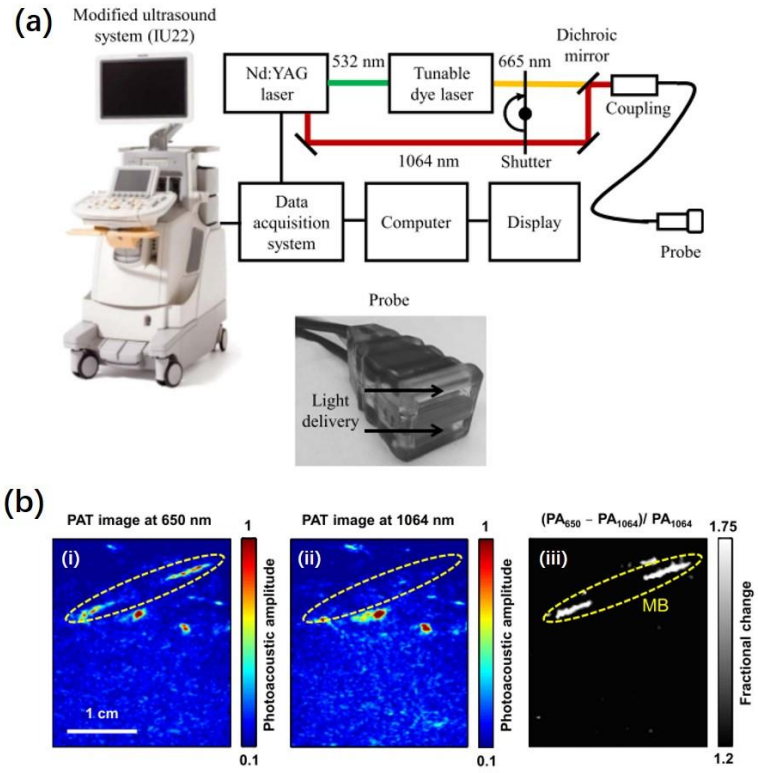

Fig1.3 (a) Schematic diagram of the dual-mode PA and US imaging system developed by Garcia-Uribe et al; (b) Photoacoustic image acquired at (i) 650nm, (ii) 1064 nm, (iii) the fractional change between 650 nm and 1064 nm.[14]

Clinical PA/US imaging with straight linear arrays has also been studied for vessel visualization[23,24]. For example, Kaku Irisawa et al. performed a feasibility study on diabetic foot patients[23]. Their system employed a light weight Alexandrite laser and a commercial portable US system (FUJIFILM FCI, FUJIFILM Medical Co., Ltd) equipped with a probe of 9 MHz (Fig1.4 (a)). It's worth noticing that the white-colored acoustic lens was used on the imaging transducer to reflect light scattered to the transducer surface (Fig1.4 (a)ii). Lower PA

signal amplitudes were found in the diabetic foot patient compared to the healthy volunteer (Fig1.4 (b)). In another experiment where a linear scanning stage was used to scan the transducer, they successfully visualized small vessels with low flow velocity in 3D PAI, which complemented the information provided by US Doppler imaging (Fig1.4 (c)).

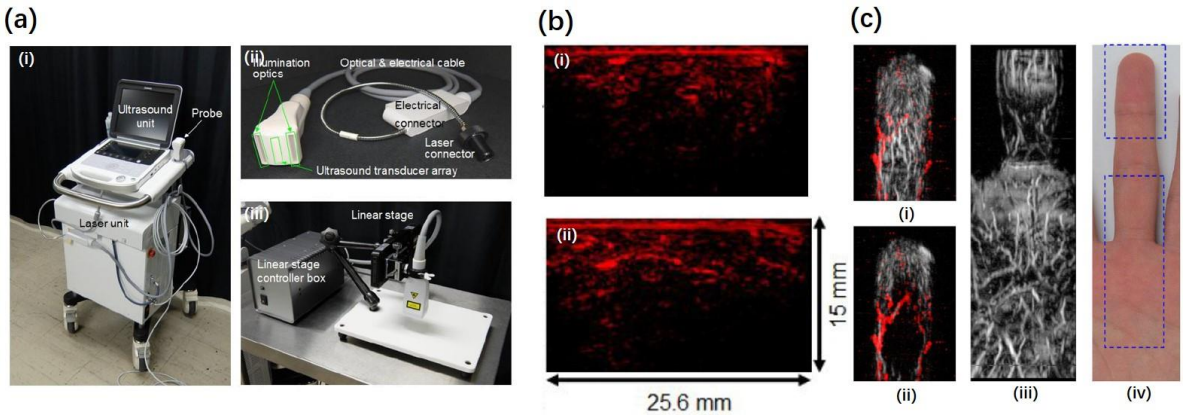

Fig1.4 (a) Photographs of the components of the PA/US system including (i) PA/US system (ii) PA/US dual mode probe (iii) linear stage scanner for 3D imaging; (b) Comparison of PA images of the foot dorsum from (i) a diabetic foot patient and (ii) a healthy volunteer; (c) 3D images of a finger acquired by scanning the transducer: (i) Maximum-intensity-projection image of the fingertip. US Doppler and PA signals are shown in red and gray scale, respectively. (ii) Sliced image showing the bow-shaped artery in the fingertip. (iii) Maximum-intensity-projection PA image of the palm. (iv) Photograph and imaged area of the finger and the palm.[23]

Another study aiming at measuring vascular compliance by PA/US imaging was carried out by Pengfei Hai et al.[24]. The commercial PAI system Vevo LAZR (Visualsonics Inc.) together with a 21 MHz straight linear array were used. PAI before and after applying an external compression force on human arm revealed the absolute Young's modulus of the imaged arm up to 6 mm depth.

In addition to the above applications, straight linear arrays are also investigated for diagnosis of arthritis[15,22]. Early symptoms of inflammation including hyper-vascularity and hypoxia can be well identified with PA/US imaging. In a study reported by Pim J. van den Berg et al[15]. A commercial 128-element linear array (SL 3323, ESAOTE) with a center frequency of 7.5 MHz was integrated with a size-comparable diode laser module, as shown in Fig1.5 (a). A modified US system (MylabOne, ESAOTE) was employed for data acquisition and reconstruction. The 808 nm wavelength was chosen because it is the isosbestic point of oxygenated and deoxygenated hemoglobin and thus is independent of SO_2. The patient's hands were submerged in water for US coupling (Fig1.5 (b)). US Doppler and PA/US imaging were performed. Their results show that the inflamed joints have higher PA amplitudes than non-flamed joints, and thus demonstrate that the system has the potential of detecting synovitis (Fig1.5 (b)).

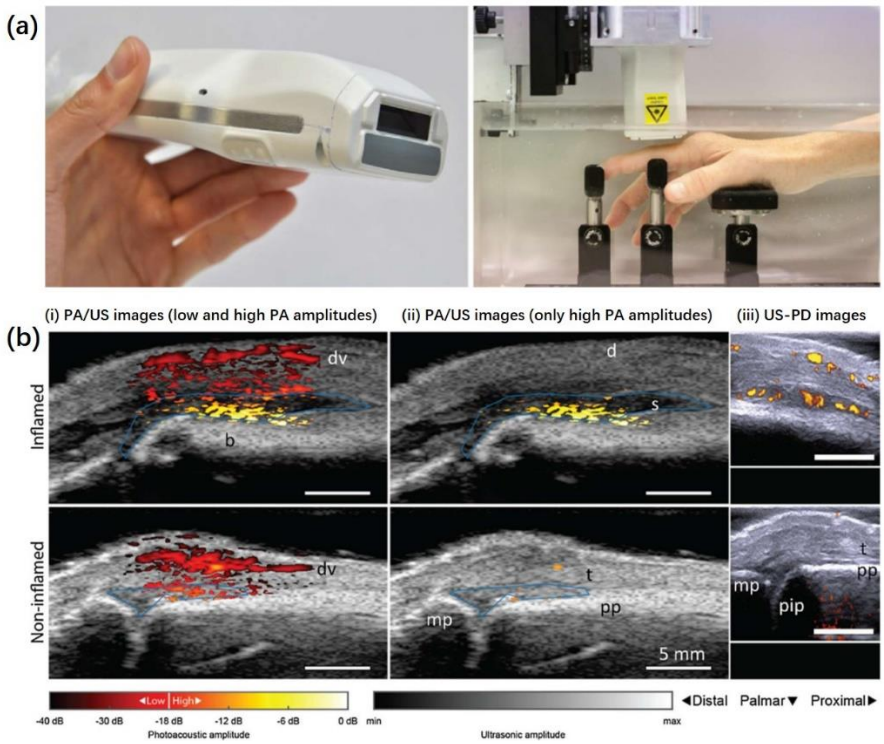

Fig1.5 (a) The PA/US probe (left) showing the light delivery window (dark aperture). The patient's hand is submerged in water (right) where it rests on a series of supports. (b) PA/US and US/Power Doppler images of an inflamed (upper row) and non-inflamed contra-lateral joint (bottom row) of a rheumatoid arthritis patient. PA/US images in (i) show an increase in amplitude levels in the inflamed joint. When discarding low PA amplitudes as shown in (ii), only features in the inflamed joint are visible. Corresponding US/PD images are shown in (iii). d=dermis; dv=dorsal vein; pp=proximal phalanx; pip=proximal interphalangeal joint; mp=middle phalanx; s=synovium; t=extensor tendon.[15]

Similarly, in another study for identifying inflammatory arthritis with PAI reported by Janggun Jo et al., SO_2 values obtained from functional PAI were found to be lower in arthritis patients' joints than in healthy joints[22]. In this study, 576 nm and 584 nm wavelengths laser pulses provided by a tunable dye laser (ND6000, Continuum) were used for imaging oxy-hemoglobin and deoxy-hemoglobin respectively. A US platform (V1, Verasonics) commercially available for research together with a straight linear array with a center

frequency of 8 MHz were employed for data acquisition.

1.2.2 Clinical PAI systems based on curved linear arrays

Typically, there are two types of curved linear arrays: convex and concave. In clinical US applications, the convex arrays are commonly used for endo-cavity applications such as urology and ovary imaging due to its advantages in providing large field of view (FOV) and deep imaging depth[25]. On the contrary, concave arrays are more commonly used for increasing PA acquisition angles, such as in PA carotid imaging[20]. Clinical PAI platforms using concave and convex arrays are summarized in this section.

Clinical applications based on concave arrays include imaging of breast cancer[13], carotid[20], vasculatures of extremities[26], and Crohn's disease[27]. For example, in the clinical study on breast cancer conducted by Gael Diot et al.[13], they aimed at identifying photoacoustic patterns of breast cancer and noncancerous breast tissue (**错误!未找到引用源。**). 10 females with malignant nonspecific breast cancer or invasive lobular carcinoma as well as three healthy volunteers were enrolled. The imaging system was based on the Multi-Spectra Optoacoustic Tomography (MSOT) platform developed previously[28]. Laser pulses with wavelengths ranging from 700 nm to 970 nm were used to illuminate breast tissues consecutively. The concave array (5 MHz center frequency) employed in this study had 256 elements, a spanning range of 174 degrees, and a diameter of 120 mm. GPU was employed

for acceleration of real-time imaging. PA signals from four main optical absorbers including oxygenated hemoglobin, deoxygenated hemoglobin, lipid, and water were linearly unmixed to reconstruct individual component maps (错误!未找到引用源。 (c)). Their results show that healthy breast tissues and cancerous breast tissues have distinctive features in terms of the distribution of four components. Specifically, they found that total blood volume in breast cancers are significantly higher than total blood volume in healthy tissue, while water and lipid layers provide weaker contrast although these two components appear disrupted in cancerous tissue.

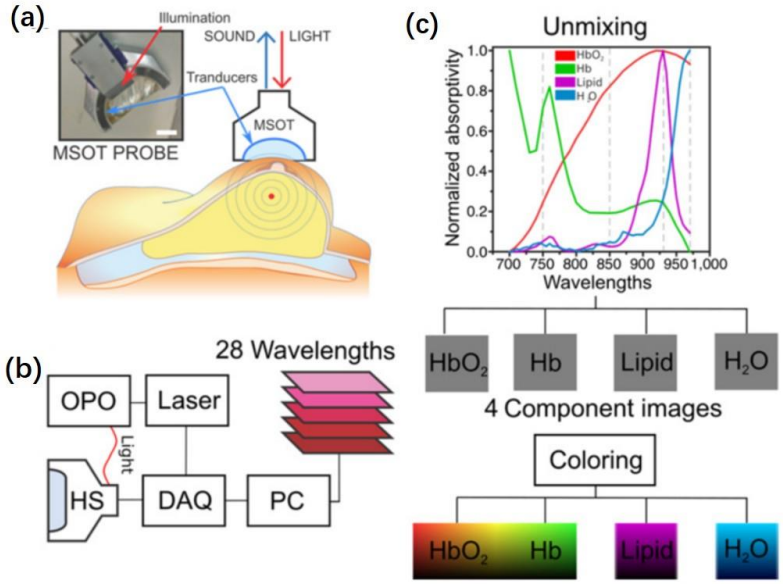

Fig1.6 (a) Photograph of the handheld MSOT probe and schematic diagram of MSOT scanning breast tissue. (b) Hardware components for image acquisition. HS=handheld scanner; DAQ=data acquisition unit; PC=personal computer. (c) Normalized absorptivity of four main absorbers in the breast tissue.[29]

In another clinical study based on the MSOT system (MSOT Acuity Echo, iThera

Medical), 108 patients with Crohn's disease were enrolled (Fig1.7)[27]. Six different wavelengths including 700, 730, 760, 800, 850, and 900 nm were used for PAI. Their results suggest that there are significant differences between active disease and nonactive disease in the relative concentrations of total hemoglobin, deoxygenated hemoglobin, and oxygenated hemoglobin.

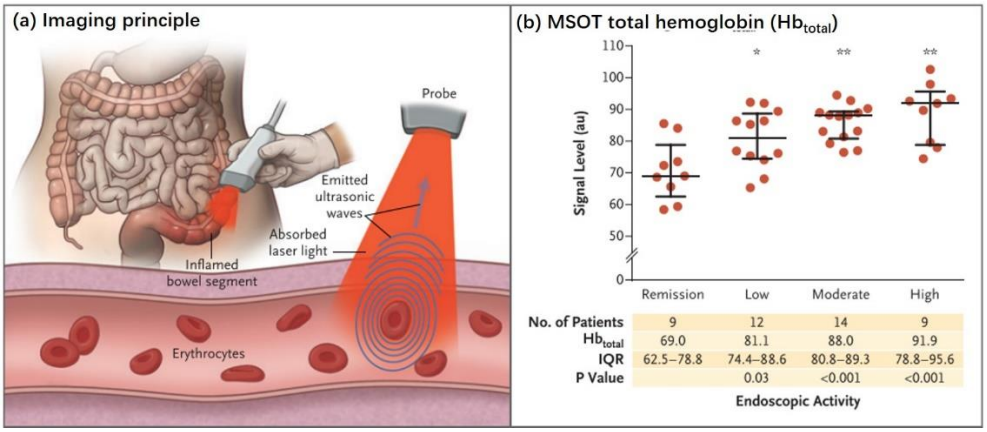

Fig1.7 (a) Schematic diagram of PAI on Crohn's disease; (b) There is a significant difference in relative concentrations of total hemoglobin between patients with nonactive disease and active Crohn's disease.[27]

Besides the studies with concave linear array based on MSOT systems, other PAI clinical studies with concave transducers mainly include imaging of fingers[21,30]. For instance, in a study reported by Milan Oeri et al.[21], four arc-shaped capacitive micromachined ultrasound transducers (CMUT) forming a ring shape were employed for imaging human fingers. Compared to piezoelectric crystal normally used in traditional UST, CMUT has the advantage of having a broad detection bandwidth and high directivity. Two of the four CMUTs had larger

arcs and each of them consisted of eight 32-element linear CMUT arrays, while the other two CMUTs had smaller arcs and each of them consisted of four 32-element linear CMUT arrays. The central frequencies for PA reception were 11 MHz for smaller arcs and 14 MHz for larger arcs. Regarding to light delivery, six laser beam outputs were integrated with each arc. The laser source was a tunable OPO laser pumped by an Nd: YAG laser. In addition to a phantom study, the feasibility of the system was also tested on a volunteer finger. The results demonstrate that the system could provide PA microvasculature images with the FWHM resolution of 160 μm.

In clinical PA/US imaging, convex arrays are mostly used for endo-cavity imaging[17,31,32]. The convex array usually has a large FOV because the elements are aligned divergently. Imaging regions of endo-cavity transducers include prostate[17], uterine cervical[32], and ovary[31]. Conventionally, US Doppler imaging is used to evaluate angiogenesis, an indicator for suspicious cancer. With the aid of PAI, higher resolution can be achieved, which may potentially increase diagnosis specificity. For example, in the studies conducted by Miya Ishihara , et al.[17,32], a micro-convex array was used for prostate cancer imaging and uterine cervical cancer imaging, respectively. The results demonstrate that PA signals near the tumor lesions may increase due to angiogenesis.

In another study reported by Eghbal Amidi, et al.[31], researchers utilized a convex transvaginal transducer and a commercial ultrasound system (EC-12R, Alpinion Medical

Systems) to image ovarian cancer. The imaging results were shown in Fig1.8. Patients were imaged at four wavelengths (730, 780, 800, and 830 nm). PA functional features (SO_2) combined with PA spectrum features were analyzed with classifiers including generalized linear model (GLM) and support vector machine (SVM). With these two classifiers, they achieved an area under ROC curve (AUC) of 0.92 and 0.93, respectively in distinguishing benign/normal lesions from ovary cancers. As shown Fig1.8, the vascular distribution of the malignant ovary is more localized and intense than that in the benign lesions.

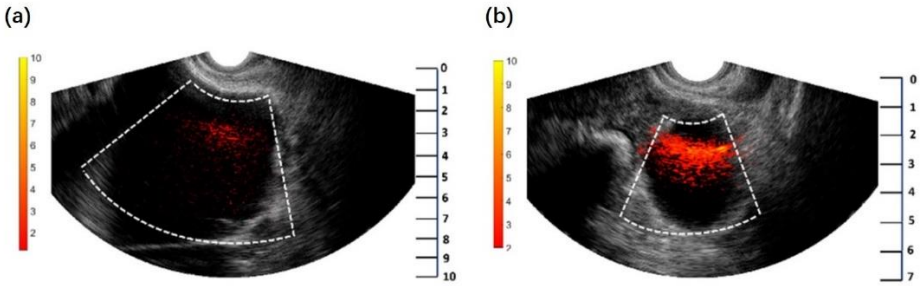

Fig1.8 Co-registered total hemoglobin and US images of (a) a benign mucinous cystadenoma and (b) a high-grade serous carcinoma.[31]

1.2.3 Clinical PAI systems based on volumetric arrays

To acquire 3D volumetric PAI data from the regions of interest, a volumetric array is usually employed, which is composed of hundreds of UST elements aligned in a 2D or a 3D surface. Because PA signals usually propagate iso-tropically, the volumetric transducer with wide detection angle is very suitable for reception of PA signals. Different from acquisition systems with linear arrays, volumetric arrays always require acquisition systems with the

capability of acquiring data from a large number of channels and high computing power to process 3D imaging data. The three common arrangements for UST elements of volumetric arrays are 2D plannar array[33-35], hemispherical array[18,36-38] and ring array[39].

The Twente Photoacoustic Mammoscope[34] is one of the first developed systems using a 2D plannar array. The array was made with a single 90 mm diameter circular polyvinylidene fluoride (PVDF) sheet. 590 independent PVDF elements with a center frequency of 1 MHz were achieved by activating 590 gold electrodes arranged on this PVDF sheet. A custom-made light delivery system comprised of prims was used for light delivery. To illuminate the whole imaging region, a scanning stage was used to move the delivery system in two axes Fig1.9 (a). In their recent upgrade systems, parallel acquisition was realized with the aid of 10 Application Specific ICs (ASICs) and two 8-channel 60 M Samples/s digitizers (NI PXI 5105, National Instruments). For an imaging area of 90 × 85 mm, it took less than 10 minutes for the data acquisition. The recent results shown in the study conducted by Michelle Heijblom et, al.[35] revealed that the Twente Photoacoustic Mammoscope was able to identify lesions in suspect breasts in 28 out of 29 cases. Results of magnetic resonance imaging (MRI) and correspondent PAI of three cases were shown in Fig1.9 (b).

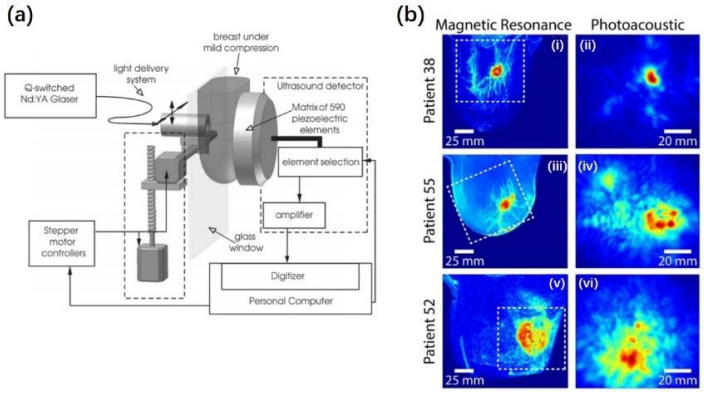

Fig1.9 (a) Schematic diagram of the photoacoustic mammoscope.[34] (b) MR (left) and PA (right) cranio-caudal (CC) average intensity projections (AIP) of the breast for three cases. (i-ii) Patient P38, having and IDC, grade 3 of 19mm;(iii-iv) Patient P55, having and IDC, grade 2 of 34 mm; (v-vi): Patient P52, having an IDC of more than 50mm. The dashed box in the MR image indicates the area from which the PA image was acquired.[35]

In addition to plannar 2D array, photoacoustic mammography can also be achieved with hemispherical array[36,37]. In the study reported by Masakazu Toi et al.[36], they employed the PAM-03 system developed by Canon Inc. The system was equipped with a 127 mm diameter hemispherical array with 512 elements (Fig1.10 (a)). The center frequency was 2 MHz and the bandwidth was 70%. The hemisphere was punctured to deliver the light at 755 nm and 795 nm wavelengths provided by a Q-switched alexandrite laser. To move the transducer in a spiral pattern for a large FOV, the transducer was placed on a 2D motorized stage. The imaging area can be chosen from 50, 70, 100 mm radius. The number of acquisitions per scan also can be selected as 1024 or 2048. The total scan time of dual wavelengths PAI with 2048 acquisitions was four minutes. The results demonstrate that the PAM-03 system is capable of visualizing fine vasculature structures of breast, and showing abnormal blood vessel structures which

matched the overlaid MRI results Fig1.10 (b).

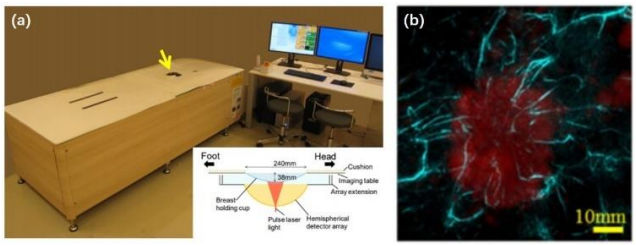

Fig1.10 (a) Photograph of PAM-03. (b) Overlaid PAI (cyan)/MRI (red) results of a breast tumor lesion.[36]

To overcome the limitation of long scanning time (~ 4 minutes) in the system presented by Masakazu Toi et al.[36], Li Lin et, al. developed a single-breath hold photoacoustic computed tomography (SBH-PACT)[39], which utilized a full-ring 512-element array as shown in Fig1.11 (a). Combined with 1064 nm light illumination, the SBH-PACT system can achieve up to 4 cm imaging depth and a 225 μm in-plane resolution. With the aid of four sets of 128-channel data acquisition systems, SBH-PACT can obtain a volumetric 3D image of the entire breast by fast elevational scanning within a single breath-hold (~15 s). To highlight tumor regions, they also developed an automatic algorithm. Tumors in all of the seven breast cancer patients enrolled were clearly revealed by the system. The X-ray mammogram and the depth-encoded PA angiogram from one of the seven tumors were shown in Fig1.11 (b).

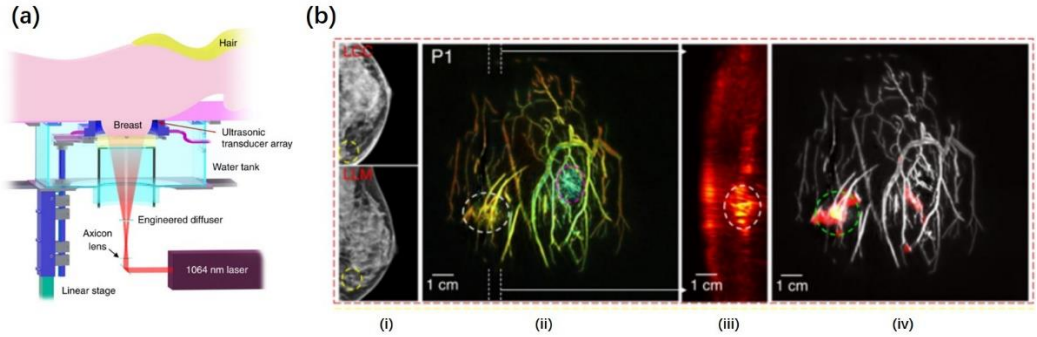

Fig1.11 (a) Schematic diagram of the SBH-PACT system. (b) (i) The X-ray mammogram of an affected breast. (ii) The depth-encoded angiogram of the affected breasts acquired by SBH-PACT (iii) Maximum amplitude projection (MAP) images of thick slices in sagittal planes marked by white dashed lines in (ii). (iv) Automatic tumor detection on vessel density maps. The tumor is identified by green circles.[39]

Instead of arranging hundreds of transducer elements in the form of large hemisphere or ring, Razansky et, al.[18] developed a real-time handheld volumetric transducer based on MSOT system for PAI of relatively small FOV. The array consisted of 256 piezocomposite elements with a 4 MHz center frequency and 100% bandwidth. These elements were arranged in a hemispherical pattern with 40 mm radius and 90° angle. To provide acoustic coupling, the cavity of the hemisphere was filled with water and sealed with transparent polyethylene membrane (Fig1.12). The spatial resolutions of the system were 300-500 μm along axial direction and 200-400 μm along lateral direction. The system was able to distinguish arteries and veins by the difference of SO_2 in these two types of vessels.

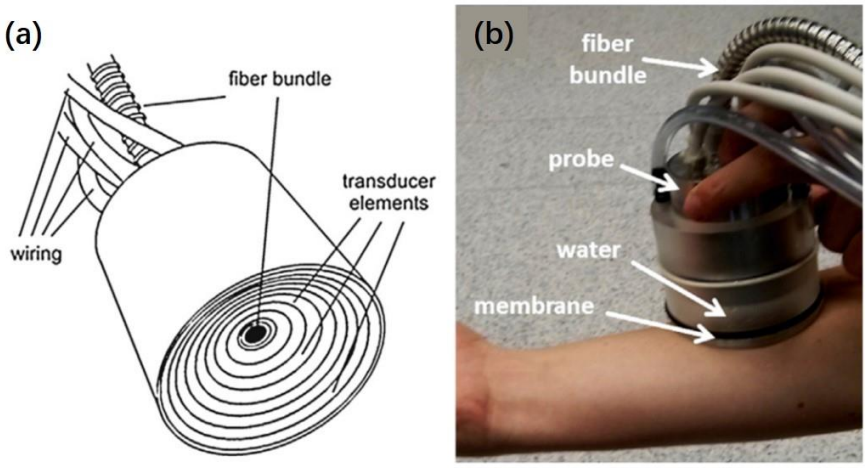

Fig1.12 (a) Layout and (b) photograph of the clinical hand-held MSOT system for high resolution 3D imaging at video rate.[18]

Regarding to clinical study, Sai Yee Chuah et, al. employed the MSOT system with the handheld volumetric transducer for skin cancer imaging[38]. Their results demonstrate that the system has the capability of 3D reconstruction of skin tumors in three patients with good histological correlation.

1.2.4 Current challenges of clinical PAI systems

Among current clinical PAI systems, combining conventional US systems with traditional US straight linear array attracts lots of interest due to its ability to provide co-registered PA/US dual mode imaging and its operational convenience for physicians. However, due to limited reception angle and limited bandwidth, commercial straight linear array is not the most suitable one for PAI[40]. In contrast, convex transducers have a large reception angle and can thus mitigate the issue of limited view. However, only small areas located at the center

of the arc can be imaged with high resolution. To overcome this challenge, Xosé Luís Dean-Ben et al. proposed a hybrid-array-based transducer, which combined the advantage of both straight linear array and convex array[41]. As shown in Fig1.13, a concave array was arranged at two ends of the intermediate linear array. A wide FOV of 40 mm × 40 mm together with minimized limited-view effect was achieved. In another study, Mathias Schwarz et al. proposed a rotation scanning method, which can extend the receiving angles of the linear array[42].

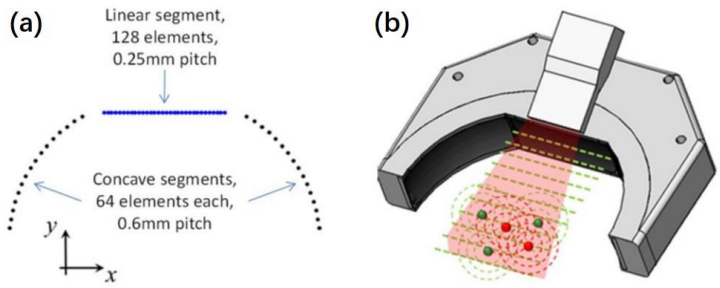

Fig1.13 Suggested configuration of the hybrid PA/US imaging probe. (a) Distribution of the array elements in the imaging plane. (b) 3D rendering of the hybrid imaging probe, including the fiber bundle.[41]

Compared with 2D PA/US imaging, 3D PA/US imaging is attractive for the ability to image the whole lesion and to give out a more comprehensive evaluation. A feasible way is to scan the 1-D linear array across regions of interest but the elevation resolution is usually poor. To address this issue, Yuehang Wang et al. introduced a method of placing a stainless steel slit at the front line of the 1D transducer[43,44] as shown in Fig1.14. Their results reveal that the slit can greatly diffract the acoustic wave and thus increase the acoustic numerical aperture in the elevational direction. The elevation resolution of the transducer was improved to 330 μm and the SNR was enhanced by around

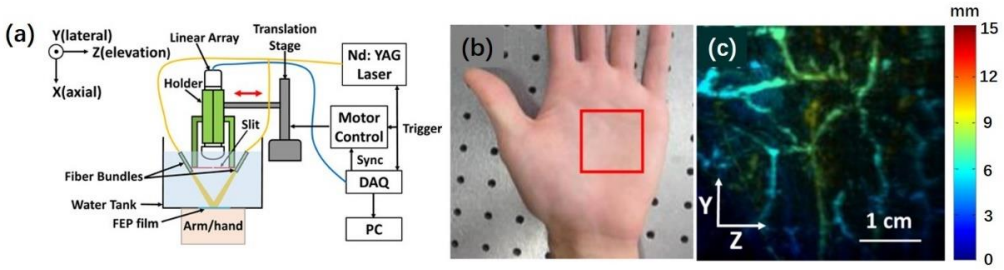

four times.

Fig1.14 (a) Schematic diagram of slit-based system. (b) Photograph of the palm of a volunteer. (c) Depth-encoded palm vascular image of the volunteer.[44]

With the proposed system, rich vascular structures could be clearly seen in the PA image of the palm from a volunteer (Fig1.14 (c)). But the slit sacrifices the US imaging capability.

Another challenge of using traditional US linear array for PAI is that PA signals have a very broad bandwidth, which can range from 1 to 100 MHz[45]. However, the bandwidth of traditional US linear array is very limited. The unmatched bandwidth can result the loss of sensitivity and spatial resolution. To overcome this issue, besides modification of traditional PZT transducer, another promising way is to use capacitive micromachined ultrasound transducers(CMUT)[21,45,46]. The CMUT transducer has wider detection bandwidth than traditional PZT transducers. As mentioned earlier, Milan Oeri et al. reported a system using a CMUT array with 15 MHz bandwidth for detection of inflammatory arthritis in fingers[21].

To summarize, with the potential of evaluating cancers and other diseases, PAI has been intensively studied clinically. In this section, several representative clinical PAI studies based on different types of transducers have been reviewed. Moreover, the limitations of current PAI

systems are also discussed. Although PAI has shown its great potential in multiple clinical applications, to add considerable values to the clinical diagnosis, its clinical efficacy still needs to be further verified with large-scale clinical studies. Besides, a versatile PAI to multiple clinical applications is also of vital importance considering the cost-effectiveness.

1.3 The outline of this thesis

In this thesis, the author first introduced the mechanism of PAI, and reviewed several representative clinical PAI systems reported so far in the first chapter.

Next, in the second chapter, the development of PA/US dual mode imaging system is presented. The imaging ability of the system was verified with both of the phantom study and the in vivo study. In the third chapter, the author first reviewed the concept and the necessity of optical fluence compensation in PAI. After then, the proposed method of fluence compensation for hand held PA/US imaging is introduced. The effectiveness of the proposed method was first verified on a tissue mimicking phantom and then verified on the breast tissue in vivo. After then, in the fourth chapter, the clinical study of PA/US imaging on thyroid cancer is presented. PAI results of thyroid cancer was compared with traditional US Doppler imaging.

In the fifth chapter, the updated PA/US imaging system with the ability of 3D PA/US functional imaging is introduced first. The clinical study of 3D PA/US functional imaging on breast cancer is presented after then. With the proposed quantification method for

differentiating malignant tumors from benign ones, 3D PA/US imaging results of breast tumors were analyzed.

After then, in the sixth chapter, the author introduced the research conducted in Georgia Institute of Technology. The aim of this research was to compare the differences between surface acoustic waves induced by laser excitation and surface acoustic waves induced by acoustic radiation force. Ultrafast US imaging was used for tracking wave propagations in both of excitation methods. Differences were investigated in terms of propagation velocity and frequency spectrum. The relationship between laser-induced shear wave amplitude and optical fluence was also investigated.

In the final chapter, the author concluded the novelty of this thesis and discussed the future of PA/US imaging in clinical applications.

CHAPTER 2 PA/US DUAL MODALITY IMAGING BASED ON HANDHELD CLINICAL ULTRASOUND

PA/US dual modality imaging based on handheld clinical ultrasound has been studied by several institutes due to its feasibility in clinical imaging process. In this chapter, our self-developed PA/US dual mode imaging system based on a handheld clinical ultrasound is presented first. Then, the imaging ability of the developed system is demonstrated through the phantom study and the in vivo study on the human forearm.

2.1 PA/US dual mode imaging system

The PA/US dual modality system was developed based on a high-end commercial clinical US system (Resona7, Mindray Bio-Medical Electronics Co., Ltd., China)[47] (Fig2.1). The system was able to perform all US imaging functions and had the ability to perform parallel data acquisition, which was required by PAI. When performing PAI, the system worked on receiving-only mode. A 192-element clinical linear probe with a center frequency of 5.8 MHz (L9-3U, Mindray Bio-Medical Electronics Co., Ltd., China) was employed for PA/US imaging. The laser source was a Q-switched Nd: YAG laser (LS-2137/2, LOTIS TII, Minsk, Belarus). This laser could generate 1064-nm laser pulses with a PRF of 10 Hz.

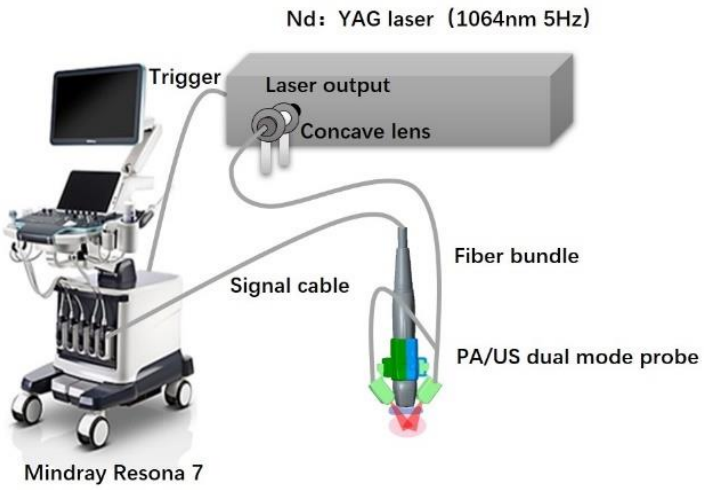

Fig2.1 Schematic diagram of the PA/US dual mode imaging system[47]

The parameters of our system have been summarized as the following table:

Table2.1 Detailed information of our PA/US dual mode imaging system

Ultrasound system	Model	Resona 7, Mindray
	Sampling rate	50 MHz
	Frame frequency for PA/US imaging	10 Hz
	PAI reconstruction method	Delay and sum
	Imaging speed	Non real-time imaging
Transducer	Model	L9-3U
	Element numbers	192
	Center frequency	5.8 MHz

	Element size	0.23 mm
Laser source	Model	LS-2137/2, LOTIS TII
	Wavelength	1064 nm
	PRF	10 Hz
	Pulse duration	10 ns

For light delivery, we customized a one-two bifurcate optical fiber bundle from Nanjing Chunhui Science and technology Industrial Co. Ltd as shown in Fig2.2. The size of the fiber head was 46 mm×25 mm to match the size of the probe.

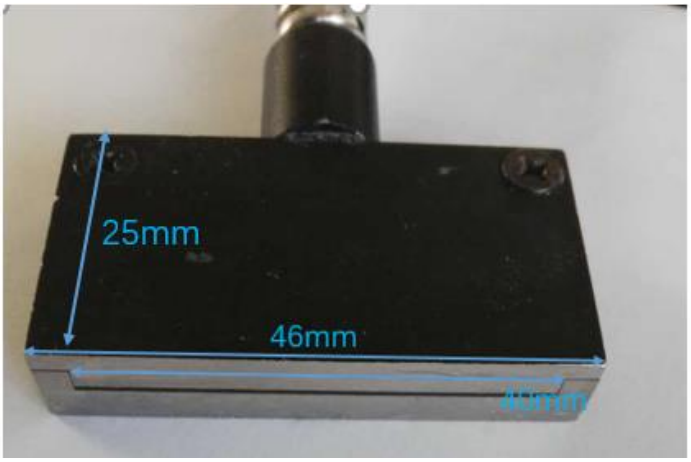

Fig2.2 Customized fiber head to match the size of the probe.

To stabilize the fiber bundle along the two sides of the probe, a holder was designed and 3D printed. The fiber bundle was inserted into two slots of the 3D-printed holder as following

figure shows.

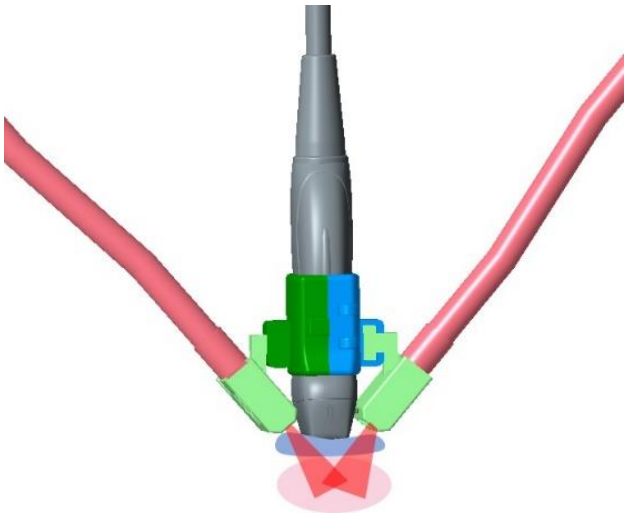

Fig2.3 Schematic diagram of the PA/US dual mode transducer.

The angle between the fiber head and the transducer was set to be 45° to make sure that the light bands from two optical fibers were close enough on the surface of the imaging target for high imaging contrast.

Besides, the shape of the dual mode probe was also within our consideration. For handheld probe, the size should be controlled to make sure it was easy to use when performing imaging especially in clinical studies. To allow light illuminating onto the surface of the imaging area below the transducer, we put a transparent soft gel pad between the probe and the imaging surface.

The thickness of the gel pad was 7 mm. Additionally, an ultrathin white film (Fig2.4)

made of silica gel and TiO_2 particles was placed at the front surface of the transducer. To make this film, we first mix the TiO_2 particles together with silica gel on a piece of glass. After then, we used another piece of glass to flatten the semi-solid mixture to make sure the mixture becomes an even layer as thin as possible.

After drying for 24 hours, the mixture would become a membrane, which we could then peel off from the glass. The aim of placing this white film was to avoid unwanted PA signals generated by the grey surface of the transducer.

The film was tested with ultrasound imaging and the acoustic attenuation inside the film was acceptable for both PAI and US imaging.

Fig2.4 The ultrathin white film made from TiO_2 particles.

To make sure the optical fluence on the skin surface was well below the ANSI recommendation for maximum permissible exposure (MPE) at 1064 nm, which is 100 mJ/cm^2[48], we first measured the area of illumination with the CCD camera as seen Fig2.5. The CCD was focused at the front surface of the gel pad during the acquisition of images.

Fig2.5 System setup for measurement of illumination area

After obtaining the illumination area (as shown below), which was 10 cm^2, we adjusted the pulse energy to make sure that the optical fluence is within ANSI limitation[48]. and the optical fluence on the imaging surface was 5.5 mJ/cm^2.

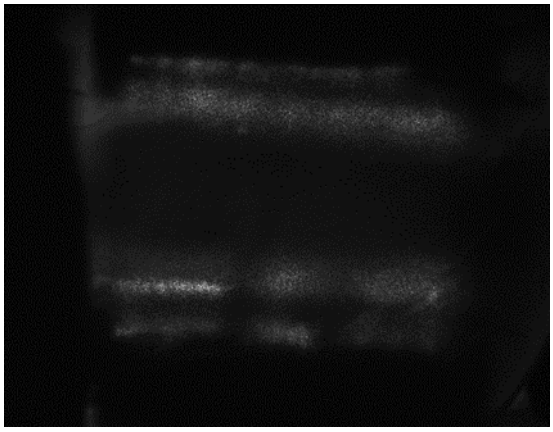

Fig2.6 Illumination area of the fiber bundle on the front side of the probe.

To guarantee that PAI and US imaging were performed on the same area, 500 μs after US imaging, the data acquisition system sent out a trigger signal to the laser to trigger the laser pulse. This delay can also make sure that the US signals will not affect acquisition of PA signals. A photo diode placed near the output of the laser source was used to provide synchronization signals for PA data acquisition (see Fig2.7). The reason we used the photodiode was that we found the delay between Q-switch trigger out signal of the laser system and laser illumination varied from pulse to pulse. After the acquisition of PA signals, PA images were reconstructed with the delay and sum algorithm and were co-registered with US images. For this version of the dual mode imaging system, it was not capable of reconstruction of PA images online. To improve the signal to noise ratio (SNR), each PA image was averaged five times and thus the total acquisition time for one PA/US dual mode frame was one second given that the PRF of laser pulse was 10 Hz. To further improve the SNR, a band-pass filtering centered at 5.5 MHz was applied to original PA signals before PA image reconstruction.

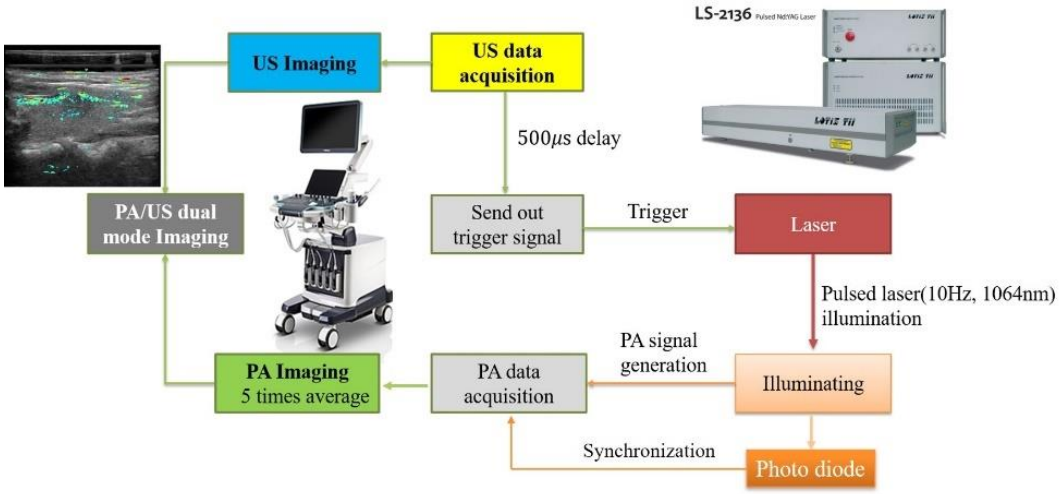

Fig2.7 Work flow of data acquisition for PA/US dual mode imaging

2.2 Phantom study for validation of the PA/US imaging ability of the system

To validate the performance of the system and the reconstruction algorithm, we did phantom experiments with a carbon rod[47]. The system setup can be seen in Fig2.8.

The carbon rod had a length of 3 cm and a diameter of 0.5 mm. To mimic the optical properties of tissue, the carbon rod was immersed into the solution of 1% intralipid. The carbon rod was first set at different inclination angles including 30°, 15°, and 0° to test the imaging ability of the system with PA signals from different directions. Besides, we also adjusted the depth of the carbon rod to test the imaging ability of the system at different depths. All PAI results were shown in linear a scale, and a threshold of 8% of the maximum PA signals was set to minimize the noise.

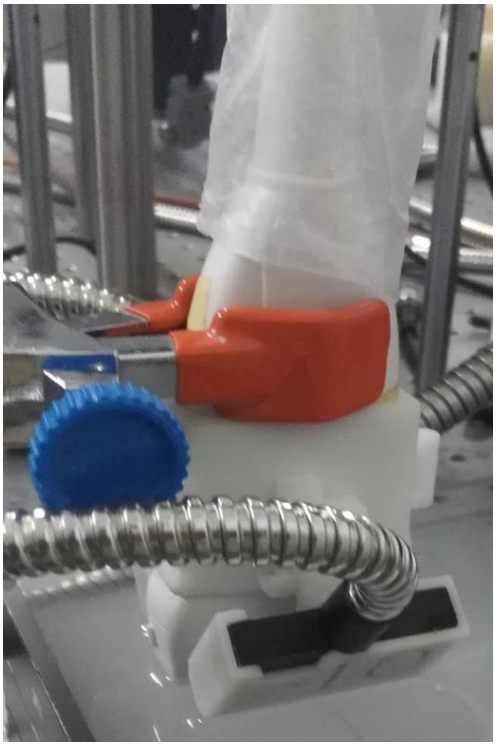

Fig2.8 System setup for phantom study with the 2D PA/US imaging system

From the PA/US imaging results of the carbon rod at different angles of inclination (Fig2.9 (a)-(c)), we could see that the shape and the position of the carbon rod shown in PAI were well matched with those shown in US imaging. These results demonstrated that the system was capable of performing PA/US dual mode imaging. Besides, we could also see that PA signals decreased with the increase of the inclination angle. This was due to the fact that the PA waves generated from the carbon rod propagated in the direction that was perpendicular to the surface of the carbon rod. Because the linear array has a limited reception angle, the sensitivity of the transducer decreases when the relative angle between the propagating direction of PA waves and the norm of the probe surface becomes larger. As a result, less

amounts of PA signals were received by the transducer when the inclination angle of the carbon rod increased.

PAI results of carbon rods at different depths were shown in Fig2.9 (d-f). We could see that due to the attenuation of the optical fluence at deeper regions, amplitudes of PA signals decreased when the imaging depths increased.

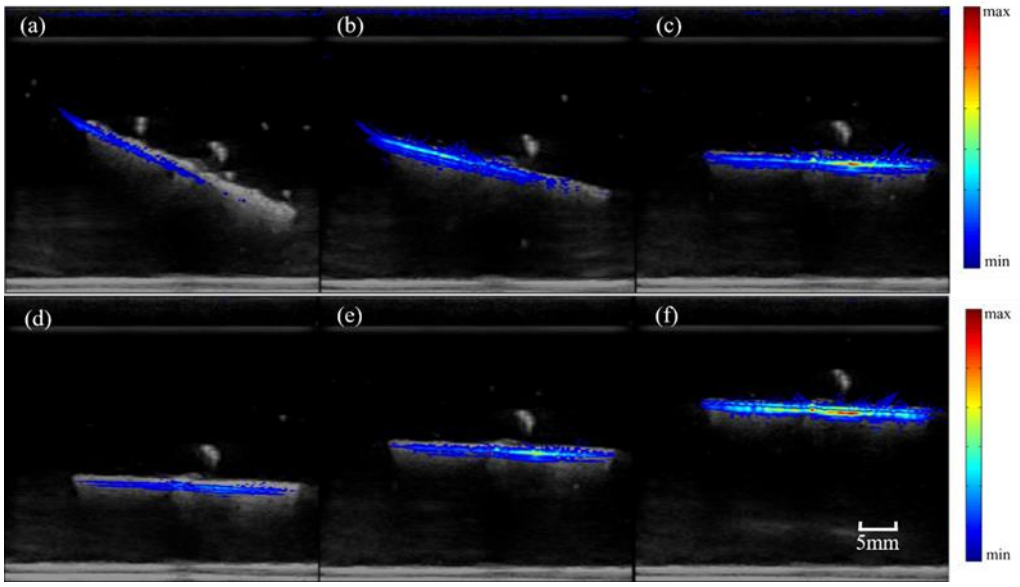

Fig2.9 Dual-modality imaging results of a carbon rod hanged in intralipid solution with different orientation angles (a-c), and different depths (d-f). US results are in gray, and PAI results are in pseudo-color (color bar shown at right).[47]

2.3 In vivo study on the forearm of a healthy adult

After validating the imaging ability of the PA/US dual mode imaging system with the phantom study, we further verified the imaging capability of the system on the forearm of a

healthy adult[47]. The protocol of this study was approved by the institutional ethics committee of Peking Union Medical College Hospital.

First, we imaged the vein in the forearm of the healthy volunteer with the probe parallel to the vein. In addition to PA/US dual mode imaging, pure US imaging results and color Doppler flow imaging (CDFI) results of the same region were acquired for comparison. After then, we rotated the transducer to image the cross section of the vein. The imaging results where the probe was parallel to the vein were shown in Fig2.10 (a)-(c), and the imaging results of the cross section of the vein were shown in Fig2.10 (d)-(f).

From CDFI results shown in Fig2.10 (a) and (d), the vein structure and the blood flow were clearly revealed. PAI results in color scale were overlaid with US imaging results (grey scale) as shown in Fig2.10 (c) and (f). The upper wall of the vein shown in PAI results were well matched with the upper wall shown in US imaging results and CDFI results. Additionally, we could also see PA signals from the skin due to the strong optical absorption of melanin in skin cells. It was worth noted that due to the large size of the imaged vein and the strong absorption of the blood, much of the light was absorbed before it went deeper into the vein. As a result, the upper wall of the vein showed up more clearly than the bottom wall in PAI results. Additionally, due to the limited reception angle of the linear array[49], the two side walls of the vein could hardly be seen in PAI results (see Fig2.10 (f)).

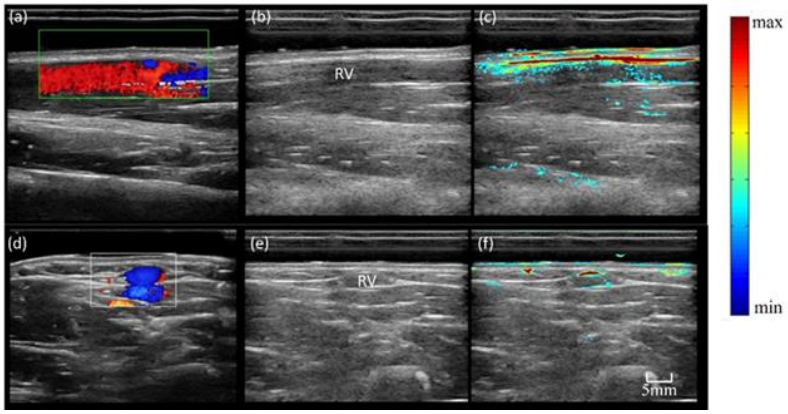

Fig2.10 Imaging results of human forearm cutaneous vein with longitude section and transverse sections. (a) CDFI result with longitude section; (b) gray scale US B-scan with longitude section; (c) PA/US imaging with longitude section; (d) CDFI result with transverse section; (e) gray scale US B-scan with transverse section; (f) PA/US imaging with transverse section;[47]

2.4 System development of 3D PA/US imaging system

After we verified the imaging capability of 2D PA/US imaging system. We moved forward to system development of 3D PA/US imaging system. Instead of reconstruction of PAI results offline, the updated system was able to perform real time imaging at 10 Hz, which was essentially limited by the PRF of laser system. Additionally, for functional PAI, we replaced the Nd: YAG laser with a tunable OPO laser, which can generate laser pulse at wavelengths from 700 to 850 nm at 10 Hz. There was a power meter inside the OPO laser, which was placed near the output of laser light. For functional PAI, we normalized each frame with the energy measured at that pulse. Normalization is of vital importance especially for functional imaging, where the optical absorption coefficient was linear to PA signals normalized by optical fluence. More detailed information can be found in Table2.2.

Table2.2 Detailed information of our 3D PA/US imaging system

Ultrasound system	Model	Resona 7, Mindray
	Sampling rate	50 MHz
	Frame frequency for PA/US imaging	10 Hz
	PAI reconstruction method	Delay and sum
	Imaging speed	10 Hz
Transducer	Model	L9-3U
	Element numbers	192
	Center frequency	5.8 MHz
	Element size	0.23 mm
Laser source	Model	Spitlight 600-OPO, Innolas laser GmbH
	Wavelength	700-850 nm
	PRF for functional PAI	5 Hz
	Pulse duration	10 ns

For 3D imaging, we designed a 3D scanning device as shown in Fig2.11. In this photograph, a human forearm lay below the 3D scanning device to indicate the location of imaging target for 3D imaging. .During the 3D imaging, we placed the 2D linear array used for 2D imaging on an electric motor, which moved at the speed of 1mm/s. During the scanning,

a set of 2D PA images and US images were acquired in turn. The total scanning length was 4 cm. With an PRF of 5 Hz for functional PAI, the total frame number for each imaging modality after one scanning was 200.

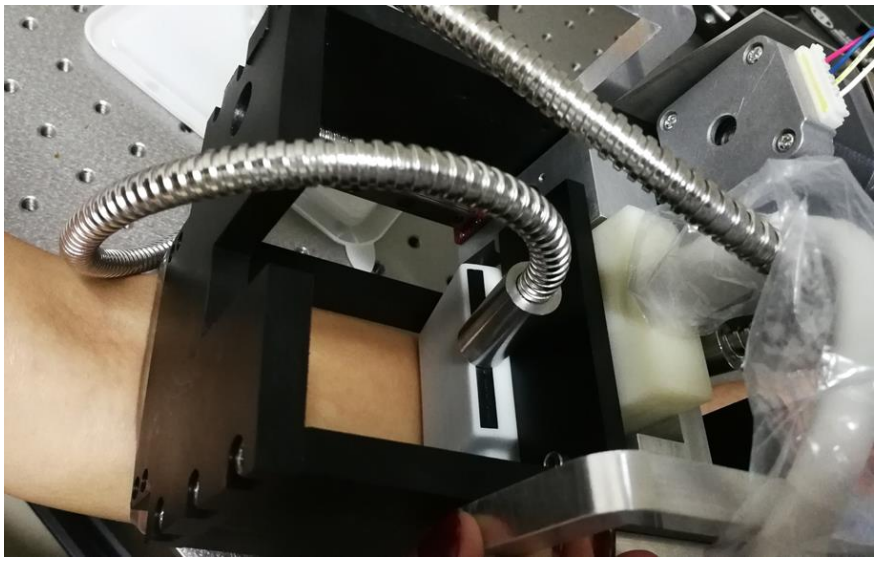

Fig2.11 Photograph of the 3D imaging device

The photograph of the 3D PA/US functional imaging system was shown below:

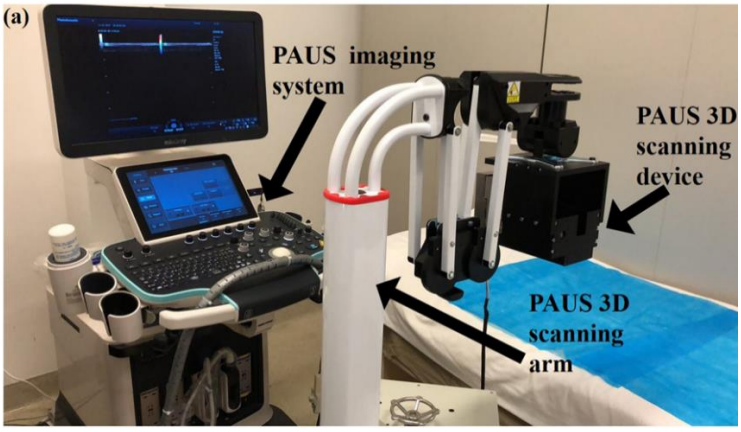

Fig2.12 The photograph of the 3D PA/US functional imaging system.

2.5 Summary

In this chapter, the development of the 2D PA/US imaging based on a high-end clinical ultrasound system is presented. Particularly, the system parameters, the setup for laser delivery as well as the workflow of data acquisition are introduced. The imaging capability of the system was verified by both of the phantom study and the in vivo study. The imaging results demonstrate that our self-developed 2D PA/US imaging system is able to perform PA/US dual modality imaging in vivo and the reconstructed PA images are well matched with US images spatially.

CHAPTER 3 OPTICAL FLUENCE COMPENSATION FOR HANDHELD PA/US DUAL MODALITY SYSTEM

Due to the optical absorption and scattering in tissue, optical fluence decays quickly as depth increases. Because the initial PA pressure is dependent on the product of the local fluence and the optical absorption coefficient, it is important to perform fluence compensation especially for quantitative PAI[50]. Although PA/US dual mode imaging with handheld probes have been investigated in previous studies[26,51], few research has been carried out on fluence compensation based on handheld PA/US dual mode imaging systems. In this chapter, the author first reviewed current methods for optical fluence compensation including Monte Carlo simulation and diffusion theory. Next, an optical fluence compensation method for the handheld PA/US imaging system was developed based on diffusion theory. After then, the proposed fluence compensation method was applied to PAI results from the tissue mimic phantom and the human breast. The comparison between PAI results before and after optical fluence compensation demonstrated that the proposed method was able to effectively improve the imaging quality especially in deeper tissue.

3.1 Introduction to the optical fluence compensation for PAI

According to the mechanism of PA effect, the initial PA pressure p_0 can be calculated from Eq. 3.1[2],

$$p_o(\boldsymbol{r}) = \frac{\beta v_s^2}{C_p} A(\boldsymbol{r}) = \Gamma A(\boldsymbol{r}) \tag{3.1}$$

where v_s is the sound speed, β is the volume thermal expansivity, C_p is the constant pressure specific heat capacity, and A is the absorbed energy density (specific optical absorption). Γ is the Grüeneisen coefficient, which represents for efficiency of the conversion of heat to pressure. $A(\boldsymbol{r})$ can be calculated by the product of the absorption coefficient μ_a and the optical fluence F at point $\boldsymbol{r}$ as shown in Eq. (3.2).

$$A(\boldsymbol{r}) = \mu_a(\boldsymbol{r}) \times F(\boldsymbol{r}) \tag{3.2}$$

In general, the Grüeneisen coefficient Γ is constant in PAI. Thus based on Eq. (3.1) and Eq. (3.2), the initial pressure $p_o(\boldsymbol{r})$ is proportional to the product of $\mu_a(\boldsymbol{r})$ and $F(\boldsymbol{r})$. Due to the strong optical scattering and absorption of tissue, $F(\boldsymbol{r})$ is nonuniform. Hence, the distribution of absorption coefficient $\mu_a(\boldsymbol{r})$ could not be accurately represented by the reconstructed initial pressure $p_o(\boldsymbol{r})$ from original PA signals. Specifically, in deeper tissue, imaging contrast can decrease significantly because $F(\boldsymbol{r})$ decreases greatly.

However, if the optical parameters of the tissue are known, one can calculate the optical fluence by solving the photon diffusion equation using the finite element method[52,53] or by numerically simulating photon transport with Monte Carlo method[2]. Both of these two methods depend on the assumption that photons propagating through tissue can be treated as neutral particles and that wave phenomena can be disregarded[54]. When applying the Monte

Carlo method, no additional assumptions are required. The trajectory of a photon is modeled as a persistent random walk. The direction of each step depends on the direction of the previous step. Given the optical properties of tissue, optical fluence can be estimated by tracking a sufficient number of photons. Although the accuracy of Monte Carlo simulation has been tested experimentally, it requires tracing a large number of photons to obtain an acceptable variance and thus is computationally heavy[55]. Different from the Monte Carlo simulation, diffusion theory is based on solving the diffusion equation. The diffusion equation is the approximation of radiative transfer equation (RTE). RTE is considered equivalent to the numerical Monte Carlo method and is difficult to solve, thus the diffusion equation is employed to obtain a fast solution[2]. The additional condition required by the diffusion theory is that the scattering coefficient in tissue is much larger than the absorption coefficient[56]. Although the diffusion theory is less accurate than the Monte Carlo simulation, it is much more computationally efficient[2]. It should also be noted that although the diffusion theory provides a fast approach to simulating fluence distribution, it is not valid near the photon source.

In the study presented in this chapter, the diffusion theory was applied to perform fluence compensation for the following reasons: 1) The interested area in PA/US dual mode imaging is beyond several millimeters depth, thus the analysis in the super shallow region of the tissue where diffusion theory is not accurate is avoided; 2) The diffusion theory is computationally

effective. Hence, it's more appropriate for clinical study, where shorter imaging time can increase diagnosis efficiency. After the optical fluence distribution is known, the relative absorption coefficient $\mu_a(\boldsymbol{r})$ can then be calculated from Eq. (3.2) through dividing the original PA signals by local fluence values.

3.2 Optical fluence compensation on tissue mimicking phantom

To evaluate the performance of the proposed compensation method, we first did a phantom study[57]. Two 0.6 mm diameter carbon rods were placed in an agar phantom to provide the optical absorption. The agar phantom was made up of three layers. Both of the first layer and the second layer were made of cuboid agar phantoms with intra lipid (IL) added, while the third layer was made of pure agar phantom. The IL added in the first layer had a weight concentration of 3.3% and the IL added in the second layer had a weight concentration of 1.8%. According to the reduced optical scattering coefficient of 0.1% IL, which was measured to be 0.832 cm^{-1} at 1064 nm wavelength, the reduced optical scattering coefficient of the first layer and the second layer were 27.5 cm^{-1} and 15.0 cm^{-1}, respectively. Because the main absorptive component of the agar phantom was water, the absorption coefficients of the first layer and the second layer were treated as same with water, which was 0.12 cm^{-1}[58] at 1064 nm. After preparing the phantom, we used the PA/US dual mode imaging system described in Chapter 2 to image the phantom with both US mode and PA mode. The angle between the transducer and the illumination direction was 45° (see Fig3.1). Similarly, a gel

pad was placed between the surface of the phantom and the surface of the transducer to allow light illuminating directly on the phantom surface below the transducer. Both of the gel pad laser and the bottom pure agar layer were considered optical transparent mediums. The schematic diagram of the imaging setup is shown in Fig3.1.

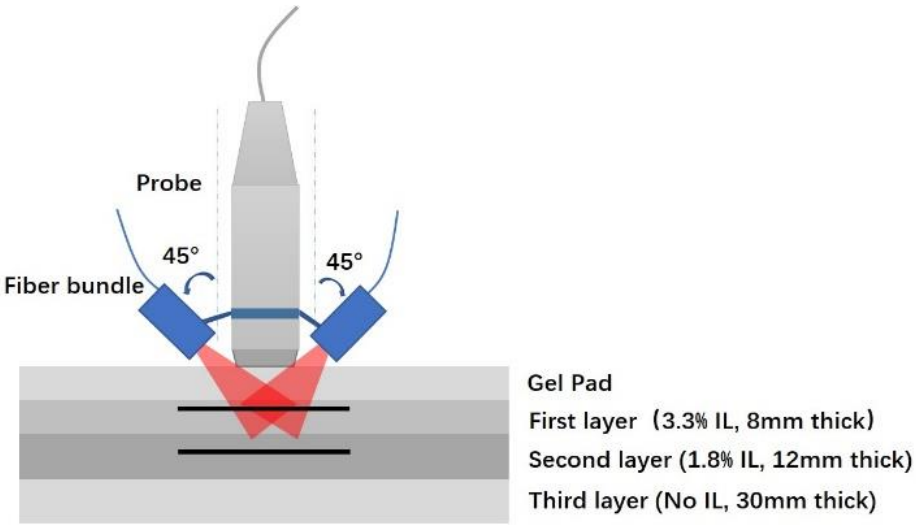

Fig3.1 The schematic diagram of imaging setup and three layers.[57]

The schematic of the imaging system was shown in Fig3.2. The laser source was an Nd:YAG laser which can generate 1064 nm wavelength laser pulse at 10 Hz. The imaging transducer we used had a center frequency of 5.8 MHz, which had an imaging depth beyond 4 cm. The system we used was based on Mindray Resona 7, the detail of which has been given in Chapter 2.

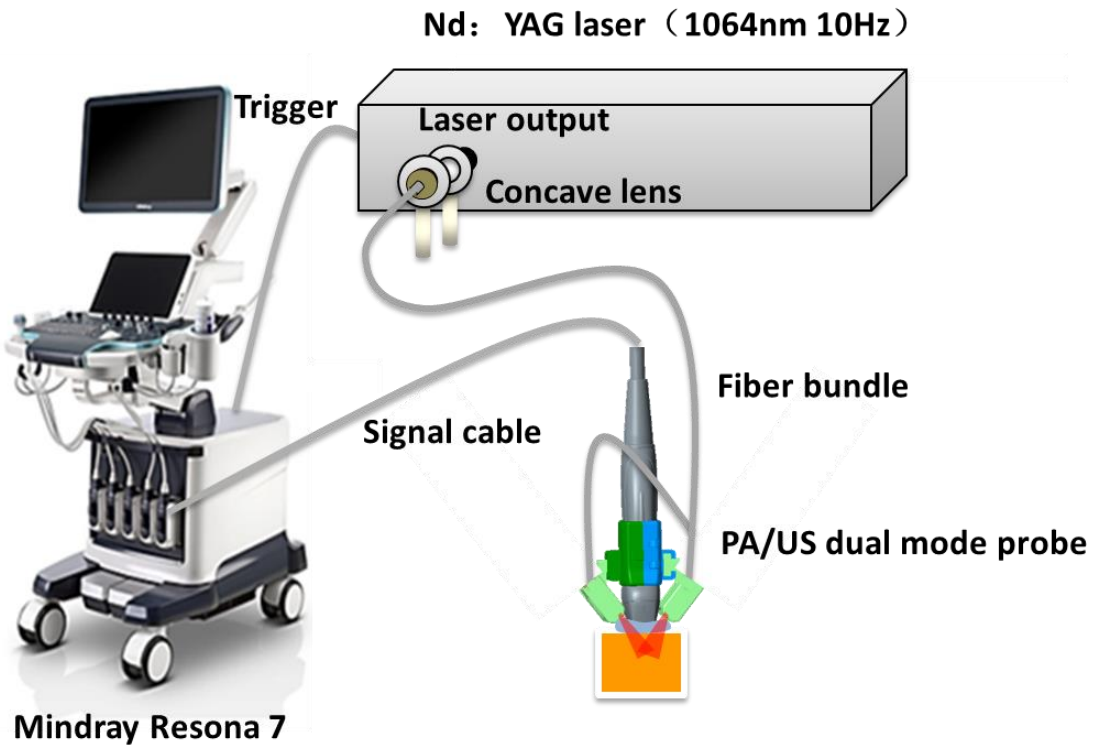

Fig3.2 The schematic of the imaging system for the phantom study

To obtain the fluence map in the imaging area based on diffusion theory, we performed the numerical simulation to solve the diffusion equation with COMSOL (COMSOL Inc., Sweden). The shapes of the two layers of the phantom with intra lipid added were assumed to be two cuboids in the COMSOL simulation (see Fig3.3). The phantom was modeled as a cuboid in our COMSOL simulation. The horizontal size was set to be 162 mm, which matched the size of the phantom itself. Additionally, the large horizontal size can make sure that the optical fluence decreased to zero at side boundaries. As a result, the boundary condition of the four lateral sizes can be set to zero fluence at COMSOL simulation. The red part shows the imaging plane of the probe, and z direction indicated the direction at depth.

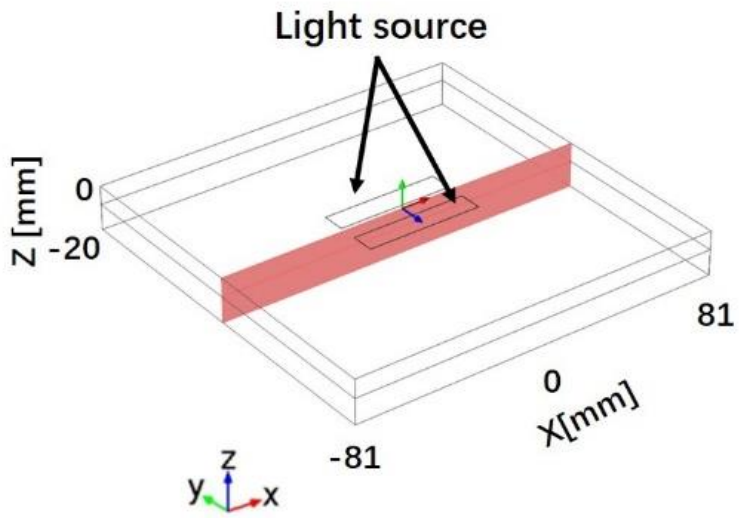

Fig3.3 The shapes of two layers of the phantom with intra lipid added were assumed to be two cuboids in COMSOL simulation.[57]

As shown in Fig3.3, in the diffuse approximation, the light source was equivalent to two bands lying dz beneath and parallel with the phantom surface with the setup shown in Fig3.1, where dz can be calculated from Eq. (3.3):

$$dz = l_t' \times \cos 31^\circ \tag{3.3}$$

Here, $l_t' = 0.19cm$ was the transport mean free path in the first layer. Each band had a dimension of 5 cm × 1 cm. The diffusion equation for global region was set as Eq. (3.4),

$$-\frac{1}{\mu_{eff}^2}\nabla^2\Phi + \Phi = 0 \tag{3.4}$$

where μ_{eff} is the effective attenuation coefficient, Φ is the fluence rate. μ_{eff} can be calculated from the absorptive coefficient and the diffusion coefficient based on Eq. (3.5).

$$\mu_{eff} = \sqrt{\mu_a / D} \tag{3.5}$$

The diffusion coefficient D is related to the absorptive coefficient μ_a, the reduced scattering coefficient μ_s' according to Eq. (3.6)

$$D = 1/(3\times(\mu_a + \mu_s')) \tag{3.6}$$

Because that the refractive index of the gel pad was similar to that of the phantom, and the refractive index for each layer of the phantom was nearly the same, the boundary between gel pad layer and the boundary between each layer of the phantom were treated as refraction-index-matched ones[2] as shown in Eq. (3.7),

$$\Phi(\boldsymbol{r}) - 2D\nabla\Phi(\boldsymbol{r}) \cdot \boldsymbol{n} = 0 \tag{3.7}$$

with $\boldsymbol{n}$ representing for the unit normal vector of the boundary pointing into the phantom layer. The source conditions of two light bands were set to be Eq. (3.8):

$$\frac{1}{\mu_{eff}^2}\nabla\Phi \cdot \boldsymbol{n} = S \tag{3.8}$$

Here, S was the optical source. Because the dimension of the cuboid was large enough for the optical fluence to attenuate to zero at the side boundary, the boundary conditions of these four side walls were set to be zero fluence. After solving the diffusion equation with COMSOL simulation, we obtained the map of optical fluence rate at the imaging plane as shown in Fig3.4. From the optical fluence rate map, we could see that the optical fluence decreased fast with

the increase of depth after 1 cm. Besides, we could also learn that, the optical fluence also decreased when the locations were away from the center region.

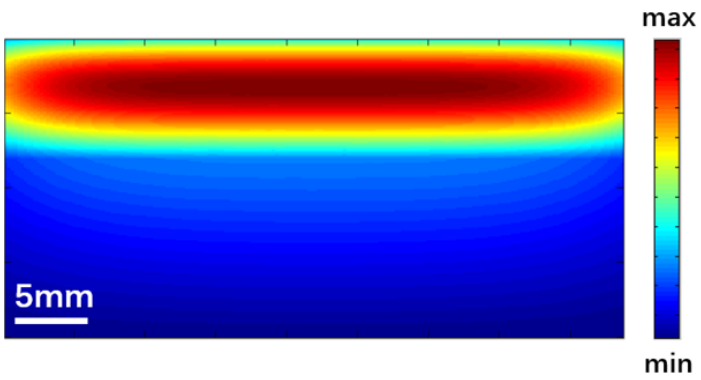

Fig3.4 Optical fluence rate map of the central cut plane.[57]

Next, we divided the original PAI result of the phantom with the optical fluence rate map obtained above to achieve the optical fluence corrected PAI result according to Eq. (3.2). The original PAI result, the optical fluence corrected PAI result, and the US imaging result of the phantom were shown in Fig3.5. Before the optical fluence compensation, only the carbon rod in the top layer of the phantom showed up (Fig3.5 (a)), and the carbon rod in the second layer of the phantom could hardly be seen. After the optical fluence compensation (Fig3.5 (b)), the carbon rod in the second layer of the phantom was as clear as the carbon rod in the first layer. US imaging results (Fig3.5 (c)) verified that the location of the second carbon rod was correctly reconstructed. It should also be noted that some noise signals were also amplified after optical fluence compensation at the bottom of the second layer.

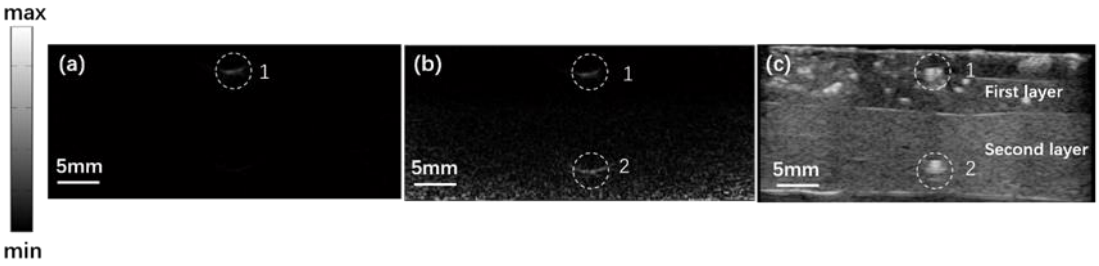

Fig3.5 (a) (b)PA images of phantom without and with optical fluence compensation; (c) US images of the same phantom.[57]

To quantitatively evaluate the proposed optical fluence compensation method, we compared the normalized values before and after compensation as shown in Table3.1.

Table3.1 Comparison of PA values before and after compensation[57]

Carbon rod number	Depth (mm)	Before compensation	After compensation
1	3.0	1	1
2	14.5	0.142	1.30

Before the optical fluence compensation, the PA signal coming from the carbon rod 2 was only around tenth of the carbon rod 1. Theoretically, the absorption coefficients of these two carbon rods are same and thus after optical fluence compensation, PA values from two carbon rods should be same. From the above table, we could see that the corrected PA value of the bottom carbon rod was much closer to the PA value of the upper carbon rod. These results demonstrate that the proposed optical fluence compensation method is able to improve the imaging quality in deeper regions of the tissue-mimic phantoms. From quantitative analysis, we could learn that before optical fluence compensation, the difference between PA values

before and after compensation was nearly 86%, while after optical fluence compensation, this difference decreased to only 30%, suggesting that our optical fluence compensation strategy has the potential to reveal deeper information. However, it should be noted that, the optical absorption coefficient from the carbon rod at the first layer and the second layer should be same. Thus, the PA signals after compensation should be exactly same with the PA signals before compensation. There might be several potential reasons why PA signals after compensation was not good enough. First, when setting optical parameters in the phantom, we might induce some errors, which may as a result, affect the accuracy of the optical fluence compensation. Second, it could be seen from our US imaging results that there were several scattering objects distributed randomly at the first layer. This can affect the both of the fluence compensation in COMSOL and the acquisition of PA signals.

3.3 A preclinical study with the optical fluence compensation applied

In the following preclinical study, we applied the proposed optical fluence compensation method to the PAI results of a healthy breast[57]. The protocol of this study was approved by the institutional ethics committee of PUMCH. PA/US dual mode imaging was carried out to obtain the PA/US imaging results of a healthy breast from a 47 years old woman with the PA/US dual mode imaging system introduced in Chapter 2. A 4 mm gel pad was placed between the breast surface and the transducer surface to allow the light illuminating directly on the breast surface right below the transducer. The angle between the illuminating direction

and the imaging plane was 30°. As mentioned before, the set of angles between illumination direction and the imaging plane should be considered with the total size of the probe. For the application in this study, because that the imaging target is human breast, the size of the probe should be small enough so that physicians can hold it very easily. As a result, the angle was adjusted from 45° in phantom study to 30° in this clinical study. The laser source was a Q-switched Nd: YAG laser (LS-2137/2, LOTIS TII, Minsk, Belarus) and could generate 1064 nm laser pulses at 10 Hz. At these wavelengths, the light can penetrate much deeper than at other wavelengths such as NIR region. The imaging contrast in tissue at this wavelength mainly comes from blood, where the oxygenated hemoglobin and deoxygenated hemoglobin are the main component and have strong absorption coefficients.

The breast tissue was assumed to have two layers including the skin layer and the breast adipose layer. This simplification was used because, first, the tissue components in breast is relatively simple, where most was adipose. Second, the skin layer was set because the skin layer has a very different optical parameters than other types of tissue. The absorption coefficient of skin layer can be ten times of other types of tissue, such as adipose. Besides, we also referred to US imaging results of the breast in this study when setting multilayer models for COMSOL simulation. Based on our US imaging results, the breast tissue also mainly concludes the skin layer which was around 3 cm thick, and the adipose layer.

To set appropriate optical parameters for solving diffusion equation, we first imaged the

breast area by US imaging to obtain the structure of the imaged area. Similar with the phantom study introduced in the previous section, we performed the proposed optical fluence compensation method by numerical simulation with COMSOL (COMSOL Inc., Sweden). In the COMSOL simulation, the breast was treated as a semi-infinite medium for two reasons: 1) the footprint of the transducer was around 4 cm length, which was much smaller than the breast; 2) The optical fluence decreases quickly as the imaging depth increases.

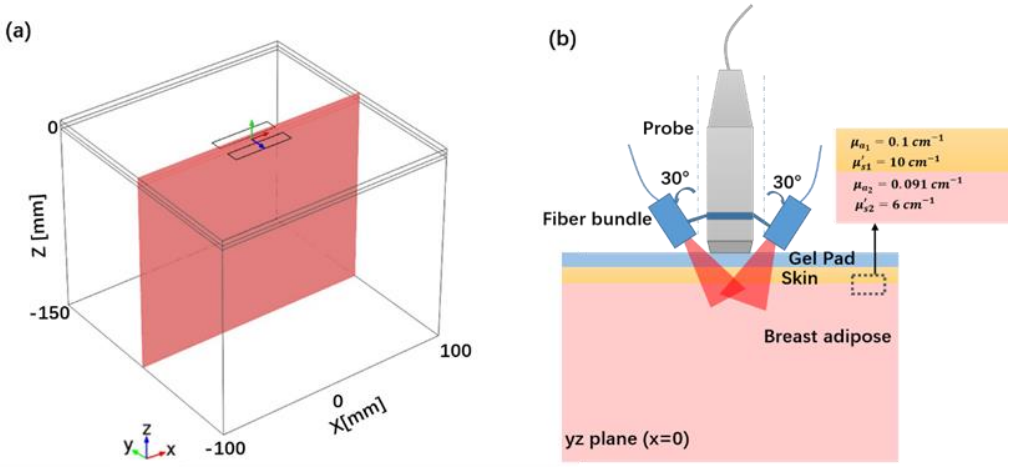

Fig3.6 (a) The shape of breast tissue was assumed to be a cuboid, (b) The schematic diagram of the detection setup.[57]

As shown in Fig3.6 (a), the breast was modeled as a cuboid with a dimension of 200 mm × 200 mm × 154 mm in COMSOL. The cuboid consisted of three layers: a 4 mm-thick gel layer, a 3 mm-thick skin layer, and a 147 mm-thick breast adipose layer. The schematic

diagram of the imaging setup for this model is shown in Fig3.6 (b)[57]. The absorption and scattering coefficients of the transparent gel pad layer were all set to be zero. Based on previous studies, the skin layer has an absorption coefficient of $\mu_{a_1} = 0.1\ cm^{-1}$and a reduced scattering coefficient of $\mu'_{s1} = 10\ cm^{-1}$[59], respectively. The adipose layer has an absorption coefficient of $\mu_{a_2} = 0.091\ cm^{-1}$ and a reduced scattering coefficient of $\mu'_{s2} = 6\ cm^{-1}$[60], respectively.

In the diffuse approximation, the light source is equivalent to two bands lying dz beneath and parallel with the skin surface, which can be calculated as

$$dz = l'_t \times cos21^{\circ} \tag{3.9}$$

where $l'_t = 0.1\ cm$ was the transport mean free path, and 21° was the incident angle on skin surface due to the light refraction from air to the gel pad. The dimension of each band was 5 cm × 1 cm. Similar with the equations applied in the phantom study, the diffusion equation for the breast region was set to be Eq. (3.4), and the source condition of two light bands was Eq. (3.8). The boundary condition between the gel pad layer and the skin layer was set to be Eq. (3.7) because the refractive index of the gel pad was similar to the refractive index of tissue. Since the distances from the optical source to the other surfaces of the model were large enough for optical fluence to attenuate to zero, boundary conditions of the four side walls and the bottom surface of the cuboid were set to be zero fluence. In COMSOL simulation, the

cuboid was meshed into free tetrahedral elements. The element size was set to be extra fine defined by COMSOL to balance the computational efficiency and the simulation accuracy. The cuboid was segmented into 1012184 elements in total. After solving the diffusion equation in COMSOL, we obtained the optical fluence rate of the cuboid. The optical fluence rate map in the imaging plane was shown in Fig3.7 (a). The fluence rate variance along the centerline (dashed line shown in Fig3.7 (a)) was plotted in Fig3.7 (b). From the fluence rate variance curve, we could see that with the imaging setup in this study, the maximum fluence rate appeared at the depth of 5 mm approximately.

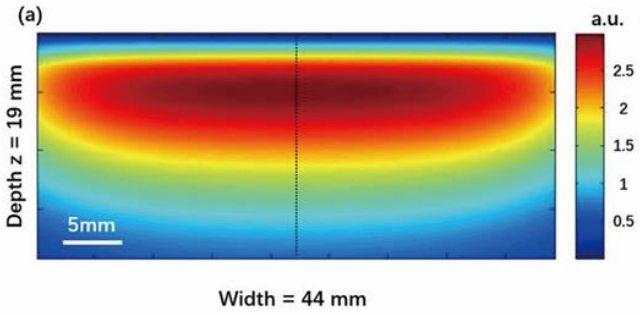

Fig3.7 (a) Relative fluence rate map at the central cut plane. (b) Relative fluence rate along the dark dotted line in (a).[57]

To compare the change of optical fluence along depth more intuitively, we plotted the relative fluence rate along the dark dotted line in Fig3.7. We could see that the maximum of the optical fluence rate showed up at around 5 mm. After then, the optical fluence decreased quickly and only to one thirds of the maximum at the depth of 19 mm. This difference between optical fluence at different depths can induce huge errors when performing functional PAI.

Because the functional PAI was closely related to PA signals normalized by local fluence. Without fluence compensation, it would be hard to restore absorption coefficients, which are contributed from the product of the concentrations and the molar extinction coefficients of photoabsorbers.

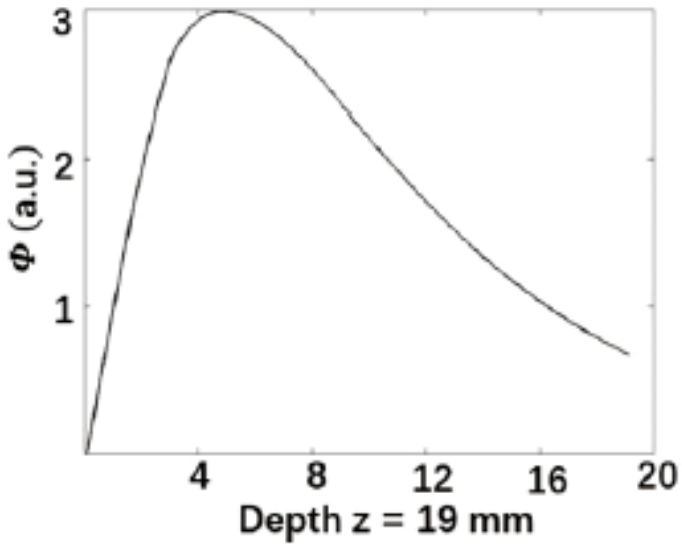

Fig3.8 Relative fluence rate along the dark dotted line in Fig3.7[57].

The relative fluence rate map shown in Fig3.7 (a) was then applied to compensate the PAI results according to Eq. (3.2). The imaging results before and after compensation were shown in Fig3.9. The original PA image was shown in Fig3.9 (a). Because the main optical absorptive component at 1064 nm in tissue is blood, the primary PA sources in the breast are vessels. From Fig3.9 (a), we could see four vessels at different depths marked with white dashed circles values. Due to the attenuation of optical fluence in deeper tissue, the PA signals from the No. 4 vessel were much weaker than PA signals from other vessels. After dividing

the original PAI result with the fluence rate map (Fig3.7 (a)), we obtained the fluence corrected PAI results as shown in Fig3.9 (b). PAI results before and after compensation were both normalized to their maximum values.

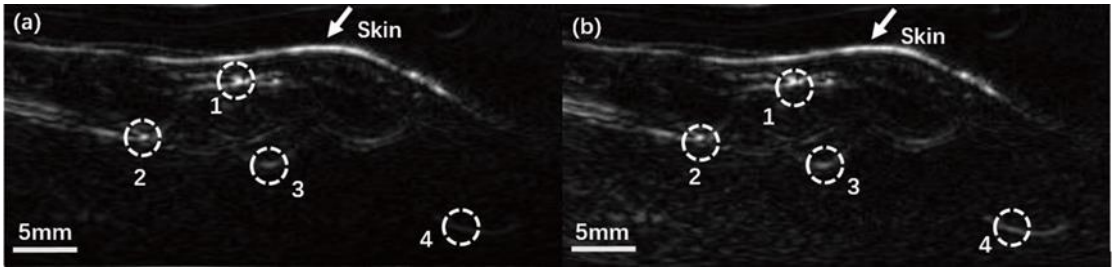

Fig3.9 (a) PAI results of a healthy breast without optical fluence compensation. (b) PAI results of the breast with optical fluence compensation.[57]

Table3.2 summarized the normalized PA values of the marked four vessels before and after compensation.

Table3.2 Comparison of PA values before and after compensation[57]

Vessel number	Depth (mm)	Before compensation	After compensation	Relative fluence
1	3.0	1	1	2.7379
2	7.3	0.8386	0.8971	2.5749
3	9.6	0.3428	0.4300	2.1830
4	14.4	0.1172	0.2908	1.1031

From the above table we could see that PA values of the reconstructed vessels in deeper regions were significantly increased. Specifically, the PA signals from No.4 vessel increased

by around ten folds and became much more prominent in Fig3.9 (b).

For the PA/US dual mode imaging in this study, 15% of the maximum value of PA signals was set as the threshold. Fig3.10 (a) and Fig3.10 (b) showed the PA/US dual mode imaging results before and after optical fluence compensation respectively.

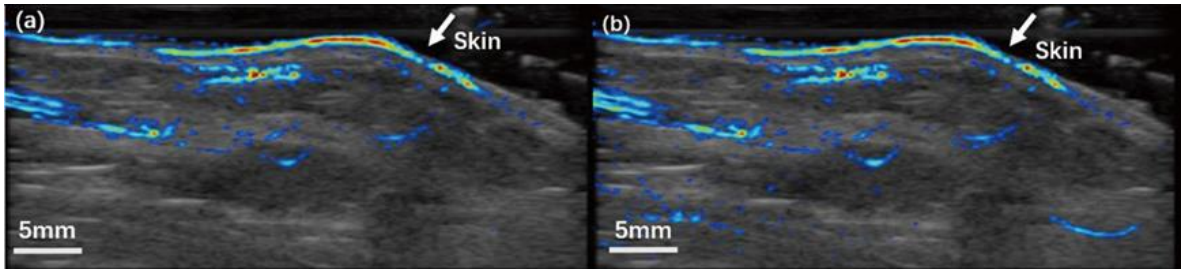

Fig3.10 (a) PA/US dual mode imaging result without compensation of optical fluence. (b) PA/US dual mode imaging result with compensation of optical fluence.

Similar with pure PAI results, PA signals from vessels in deeper regions were much weaker and can be missed before the fluence compensation. However, it should also be noted that the noise signals in deeper regions were also amplified after the optical fluence compensation (see scattered patterns in the left bottom of Fig3.10 (b)).

3.4 Summary and discussion

In this chapter, we proposed an optical fluence compensation method for the handheld PA/US dual mode imaging system. The proposed method was based on the diffusion theory and was performed with COMSOL simulation. We first verified our method with the phantom study and then applied the method to the preclinical study case, where the imaging target was

healthy breast tissue. The comparison of PA signals before and after the fluence compensation reveals that the proposed method could restore more PA sources especially in deeper regions.

However, it should be noted that the proposed method is still based on a simplified model. For example, the skin surface in the US imaging is not as even as the simplification model. To apply the method for real tissue imaging, more factors need to be considered. For example, breasts and other organs usually consist of different types of tissues including fat, muscle, water, etc. Thus, to obtain an accurate optical fluence map, optical parameters from different types of tissues should be included in the simulation model. US imaging can aid in obtaining more information of tissue types in imaging regions.

It also should be mentioned that, for the fluence compensation strategy in this study, the main challenge is to identify the optical parameters of real tissue. This can change from case to case. Besides, although US can provide anatomy information, sometimes it is still hard to identify every type of tissue with pure US imaging. In this case, approximating optical parameters based on previous studies is necessary, although this may include errors.

The uncertainty of the optical parameters of the imaged targets could also generate errors in functional PAI even after optical fluence compensation. For example, the calculation of SO_2 is very sensitive to the optical fluence and thus very sensitive to the optical absorption and scattering coefficients of tissue. In this case, the relative difference between fluence instead of

the absolute difference is important. Thus, when performing functional PAI, one potential method to increase the accuracy for calculation of concentrations of the photo-absorbers is utilizing wavelengths where the optical absorption and scattering are similar is important

Besides, the proposed method was only applied to 2D imaging in this study. In the future, it could also be extended to 3D PA/US imaging. It should be noted that the optical properties of the same type of tissue can also vary, which increases the difficulties in obtaining an accurate fluence map of real tissue. Finally, the noise signals in deeper regions are amplified as well after the fluence compensation. Thus, the distinguishing between real PA signals and the noise signals is also important to improve the imaging quality in deeper tissues.

In conclusion, our study demonstrates that based on the anatomy information provided by US imaging, the proposed optical fluence compensation method could aid in regaining important information from deeper regions in PA/US imaging. In the future, the proposed method can potentially be applied to quantitative PAI, where the accurate calculation of absorption coefficients in imaging areas is an essential step.

CHAPTER 4 AN INITIAL CLINICAL STUDY OF THYROID CANCER WITH HANDHELD PA/US IMAGING SYSTEM

A clinical study of human thyroid with PA/US dual mode imaging is presented in this chapter. We imaged both healthy and cancerous thyroids and compared PAI results with color Doppler US imaging results. PAI of thyroids revealed more blood vessels than color Doppler US imaging, demonstrating that PAI could provide important complementary information to traditional US examinations of thyroids.

4.1 Background

As an endocrine gland, thyroid is located at the front of neck and consists of two connected lobes. The primary function of the thyroid is to produce hormones that regulate body's metabolic rate, heart and digestive function, brain development, etc. Thyroid nodules are solid or fluid-filled lumps that form within thyroids. Only a small percentage of thyroid nodules are cancerous, with the malignant cases of all the discovered thyroid nodules being around 10%[61]. The malignant cases of thyroid nodules mainly include papillary thyroid cancer and follicular cancer[62]. The treatment of thyroid nodules highly relies on the early detection of malignant cases with high accuracy[63].

US detection is recommended as a routine examination of thyroids based on the American

Thyroid Association (ATA) guidelines[61]. To further improve the diagnosis accuracy of thyroid cancer, novel imaging techniques have emerged recently. For example, shear wave elastography and contrast-enhanced ultrasound (CEUS) have been investigated for evaluation of thyroid nodules[64,65]. Although these new imaging techniques have shown great potential in diagnosis of thyroid nodules, they still have limitations. For example, shear wave elastography can reveal the stiffness information of the thyroid nodules but cannot provide functional information such as micro-vascularization of thyroid carcinomas. CEUS can provide micro-vascularization information of thyroid cancers but is invasive due to the requirements of the intravenous injection of contrast agents. Thus, noninvasive imaging modalities, with the capability of providing morphological, structural and microvascular information are highly desired for the diagnosis of thyroid cancer.

In the following study, we carried out a preclinical study of thyroid cancer with the self-developed dual-mode PA/US imaging system[47]. Both of the healthy and cancerous nodules were imaged with PA, US and color Doppler US imaging modalities. By comparing PAI results with the US imaging and the color Doppler US imaging results, we found that PAI could provide important complementary information to traditional ultrasound examinations of thyroids.

4.2 System setup

The system employed in this study has been introduced in Chapter 2. As seen in Fig4.1, the PA/US dual mode system was based on a high-end ultrasound imaging system (Resona 7, Mindray Bio-Medical Electronics Co., Ltd., China), which was capable of performing parallel data acquisition while preserving all US imaging functions including color Doppler imaging. The transducer used for receiving US and PA signals had 192 elements with a center frequency of 5.8 MHz. When performing PAI, the system was set in the receiving-only mode. The laser source was an Nd: YAG laser, which could generate 10 Hz laser pulse at 1064 nm. At 1064nm, the main absorptive component in tissue is hemoglobin. The laser was triggered 500 μs after the US imaging to make sure that the US signals in US imaging did not affect PA signals acquisition. A customized fiber bundle together with a 3D-printed holder were used for light delivery. A gel pad was placed between the transducer surface and the skin surface to make sure that light can illuminate directly onto the skin surface underneath the transducer. To avoid unwanted PA signals generated from the transducer surface, we made a thin film made out of silica gel and TiO_2 to cover the transducer surface. The optical fluence on the skin surface was measured to be 5.5 mJ/cm^2, well below the ANSI recommended maximum permissible exposure (MPE), which is 100 mJ/cm^2 for 1064nm. PA images were reconstructed with the delay and sum algorithm, and each PA image was averaged by 5 frames to improve the SNR. To show PAI results more clearly, all PA images were normalized to the maximum value.

Because the reconstructed PA values had a large dynamic range, which was around 30 dB, the PA images were presented in log scale. To suppress the noise level, we set a threshold of 10% of the maximum reconstructed PA values.

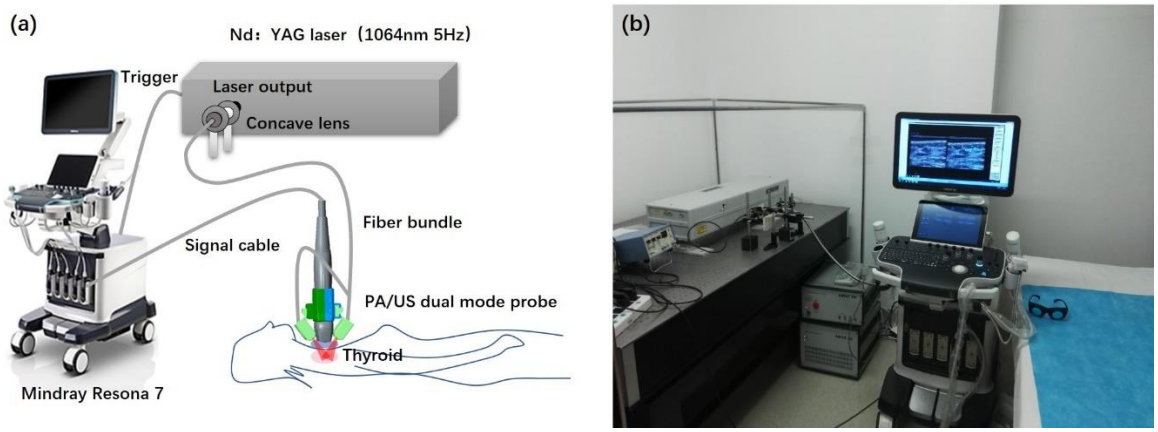

Fig4.1 (a) Schematic diagram and (b) photograph of the PA/US dual mode imaging system.[47]

4.3 Patients enrollment and PA/US imaging procedure

Patients for the preclinical study were enrolled from the outpatients and inpatients of surgery department at Peking Union Medical College Hospital (PUMCH) from Dec. 15th, 2016 to Jan. 5th, 2017. The enrollment criteria included[47]: (1) Ultrasound suspicious malignant thyroid nodules with indication for fine needle aspiration biopsy (FNAB); (2) Histology proved malignant thyroid nodules. All patients together with 3 volunteers underwent US examinations including both traditional US imaging and color Doppler flow imaging (CDFI). The structural information, including the margin, position, intramodular structure as well as

the blood flow patterns were obtained through US imaging and CDFI. After then, PA/US dual mode imaging was performed on the thyroid nodules. The patient enrollment and the imaging procedure were approved by the institutional ethics committee of PUMCH. Informed consent was signed by all patients before performing the PA/US imaging.

4.4 Preclinical study results

PA, US and CDFI imaging results from one normal and three cancerous cases are presented in this section. The CDFI and the PA/US dual mode imaging results of each case were compared. After presenting PA/US images, detailed information from all of the ten patients, including age, sex, depth and size of lesion, as well as the histological diagnosis results are provided[47] in Table4.1.

Imaging results from a healthy right thyroid are shown in Fig4.2[47]. The middle panel is the pure US imaging result, while the left panel is the CDFI result and the right panel is the PAI result. Anatomical structures including skin, muscle, carotid, thyroid, trachea, and vertebrae were marked in Fig4.2 (b). Compared with sporadic blood flow signals in the thyroid region from CDFI results, PAI results reveal much more abundant PA signals, demonstrating that PAI is more sensitive to vessels in the thyroid parenchyma. However, the PA signals from the carotid artery could hardly be seen. This may be due to the strong absorption of the muscle layer locating right above the carotid artery.

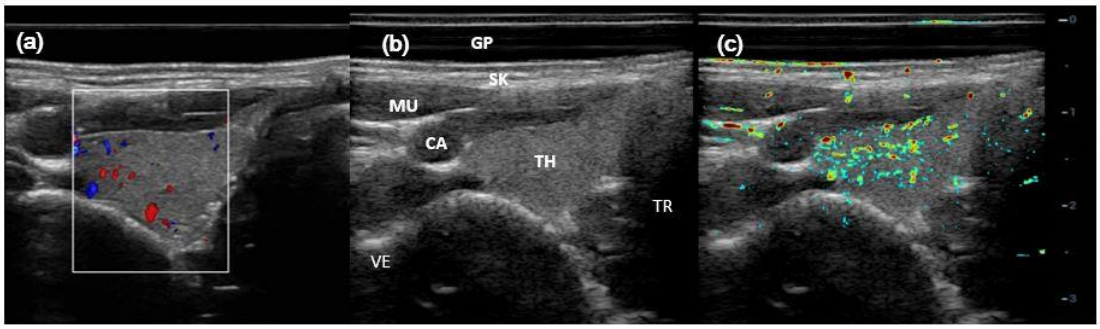

Fig4.2 Imaging results from a healthy right thyroid. (a) CDFI result; (b) gray scale US B-scan; and (c) PA/US imaging result. GP (gel pad), SK (skin), MU (muscle), CA (carotid), TH (thyroid), TR (trachea), VE (vertebrae).[47]

Imaging results of three thyroid cancerous cases are shown next. Results from a left lobe papillary thyroid cancer (PTC) (case No.8 in Table4.1) is first shown in Fig4.3[47]. The thyroid nodule had the largest diameter of 9 mm with the center lying about 1.3 cm beneath the skin. Both of the intra-nodular and peripheral vessels are clearly revealed by either CDFI or PAI results. Additionally, from PAI results, we could see that there were two highly suspected feeding vessels locating near the upper boundary of the thyroid (white dashed arrows). The pathological results of this case show that the anterior capsular of the thyroid and the peripheral muscle was infiltrated by the tumor. From the results of H&E and immune histochemical evaluation, strong CD34 showed up in the thyroid anterior capsular area. These histological results demonstrate the existence of the vessels in the thyroid anterior capsular. Besides, VEGF +, and Ki67 1% were also detected in and around the tumor area.

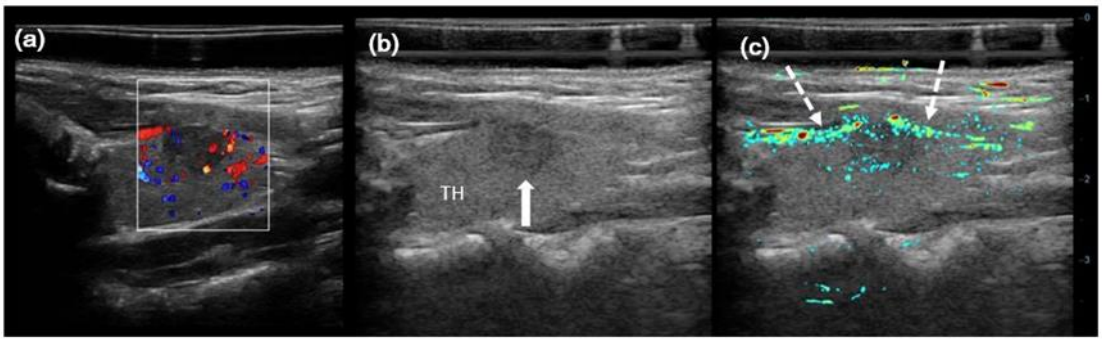

Fig4.3 Imaging results from a left lobe papillary thyroid cancer (PTC, Follicular variation) with the largest diameter of 9 mm. (a) CDFI result; (b) gray scale US B-scan; and (c) PA/US imaging result. Solid white arrow indicates left lobe PTC, and dashed white arrows indicate suspected feeding vessels.[47]

Imaging results from a right lobe PTC (case No.9 in Table4.1) are shown in Fig4.4[47]. The largest diameter of the nodule was 13 mm and the center of the lesion was around 1.5 cm beneath the skin. In CDFI results, strong vascular signals only showed up surrounding the lesion, while PA/US imaging results showed more abundant PA signals in other parts of the thyroid. Histological diagnosis demonstrates that invasion existed in thyroid capsular and peripheral tissues.

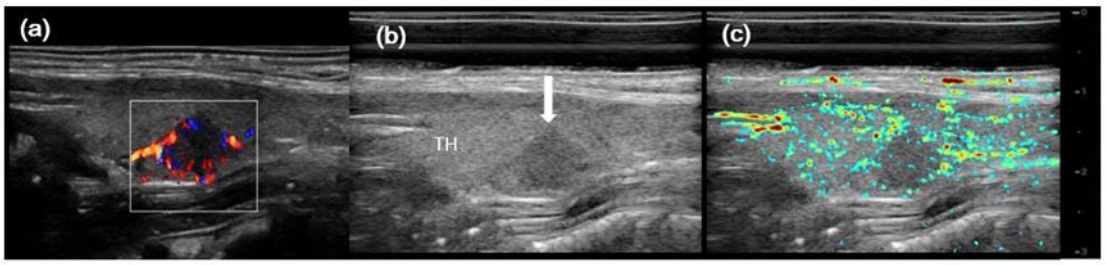

Fig4.4 Imaging results from a right lobe PTC with the largest diameter of 13 mm. (a) CDFI result; (b) gray scale US B-scan; and (c) PA/US imaging result. White arrow indicates right lobe PTC.[47]

Another left lobe PTC (case No.6 in Table4.1) with the largest diameter of only 3 mm is shown in Fig4.5. The center of the lesion was about 1.0 cm beneath the skin. PAI results (Fig4.5 (c)) showed plenty of PA signals in both the lesion region and the surrounding thyroid parenchyma, while CDFI results only showed few blood signals in the same regions.

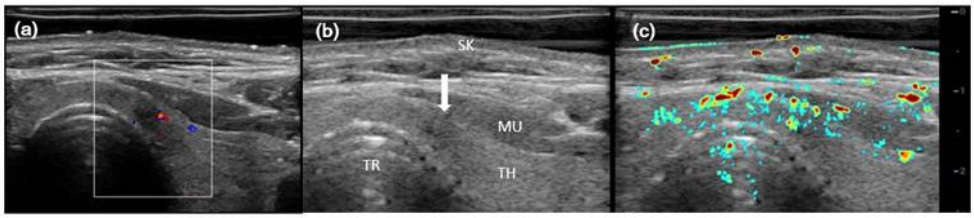

Fig4.5 Imaging results from a left lobe papillary thyroid cancer (PTC, Follicular variation) with the largest diameter of 3 mm. (a) CDFI result; (b) gray scale US B-scan; and (c) PA/US imaging result. White arrow indicates the left lobe PTC.[47]

In the three cases presented above, PAI shows the capability to reveal both the peripheral and intra-nodular vessels of human thyroid. The following table presents detailed information of 10 cases with thyroid cancers. Three types of information are provided: 1) Basic information including sex and age of patients; 2) Lesion information including lesion size, and lesion depth; 3) Imaging results including PAI results, CDFI results; 4) Histological results.

Table4.1 The clinical information, comparison between PAI and CDFI, and histology results[47]

Case No.	Sex	Age	Lesion Depth (cm)	Size (mm)	PA vs CDFI	Histological diagnosis
1	F	51	1.5	7	PAI showed more signals than CDFI	Left lobe papillary thyroid micro-carcinoma (PTMC), with peri-thyroid tissue invasion

2	F	54	1.3	5	PAI showed more intra-nodular signals than CDFI	Left lobe PTMC with follicular variation
3	F	52	1.8	5	Due to depth limitation, PAI only showed more signals in upper-half of the tumor than CDFI	Left lobe PTMC
4	F	55	1.5	5	PAI showed more intra-nodular signals than CDFI	Left lobe PTMC
5	F	62	1.2	7	PAI showed similar vascular information with CDFI	Right lobe PTMC
6	M	39	1.3	3	PAI showed more peri-nodular signals than CDFI	Left lobe PTMC
7	F	38	1.5	11	PAI showed similar vascular information with CDFI	Left lobe PTC with large area of intra- tumor necrosis
8	F	23	1.3	9	PAI showed more signals in tumor and anterior thyroid capsular	Left lobe PTC, with invasion of anterior thyroid capsular and peripheral muscles. Ki67: 1%, VEGF+ CD34: ++
9	F	37	1.5	13	PAI showed more signals than CDFI	Right lobe PTC, with invasion to thyroid capsular and peripheral tissues.

						CD34+++ Ki67 2%, VEGF+
10	M	43	Left lobe: 2.5	4	PAI showed similar vascular information with CDFI	Left and right lobe PTMC. Ki67 5%, VEGF+, Calectin-3+, CydinD1+, CD34++
			Right lobe: 3.5	7	CDFI showed more vascular information	

Based on the above table, PAI results from 7 out of 10 thyroid cancerous cases reveal more abundant vascular information than CDFI results either inside lesions or in thyroid capsular regions. Among three cases where PAI showed similar results with CDFI (case No. 5, No.7, No. 10), the lesion in case No.10 was relatively deeper than other lesions (2.5 cm depth for left lobe and 3.5 cm depth for right lobe), and thus the local fluence was too low to generate PA signals with enough amplitudes. In case No. 7, from histological diagnosis we could see that there was a large area of intra-tumor necrosis, indicating that few vessels existed inside the lesion. As a result, only few PA signals showed up inside the lesion.

4.5 Summary and discussion

In this study, PA/US dual mode imaging was applied to evaluate thyroid nodules. From 10 cases of thyroid cancers and 3 cases of healthy thyroids, we found that PAI is able to provide abundant vascular information. With the aid of US imaging, the vascular information provided by PAI can be clearly located. After comparing PAI results with CDFI results, we found that

in most cases, PAI could provide more vascular information than CDFI. This is mainly due to the difference existing in the mechanisms of two imaging modalities: CDFI utilizes Doppler effect and thus highly depends on the velocity and the direction of blood flow. In vessels where the blood flow velocity is very low, CDFI may not be able to reveal the correspondent vascular information. Different from CDFI, PAI depends on the existence of optical absorptive components such as hemoglobin, and thus is insensitive to the blood flow velocity. As a result, for small vessels where the blood flow is very slow, PAI is more sensitive than CDFI.

There are also limitations in PAI. First of all, because PAI highly depends on the local fluence in the imaged region, if light attenuates too much before it arrives at the regions of interest, only few PA signals can be generated. For example, in Fig4.3-Fig4.5, we could clearly see that as the imaging depth increased, PA signals became weaker. Few signals from the carotid in Fig4.2 also suggests that if highly absorptive tissue exists above the regions of interest (muscle layer in this case), PAI will be affected. Second, since PA signals are essentially ultrasound waves, they can be reflected at tissue boundaries where the mismatch of acoustic impedances exists. For example, in trachea regions in Fig4.2 and Fig4.5, where optical absorptive components were not expected, PA signals also showed up. Third, a handheld US linear array has a limited reception angle. However, since thyroid nodules locate in relatively shallow (~2 cm from the probe) regions, the quality of PAI is not significantly affected.

Our study demonstrates that the combination of PAI and US imaging has multiple advantages: First, PAI can provide important complementary information such as vascular information to US imaging. Second, because physicians are familiar with traditional US imaging, the imaging process is convenient especially when combined with a high-end clinical US system. The high-quality anatomical information provided by the high-end clinical US system can aid in interpreting PAI results more accurately.

In the future, to add more diagnostic value, studies including both malignant and benign thyroid nodules should be carried out. Moreover, multi-spectral PAI can be investigated to perform functional analysis such as exploring the difference of SO_2 between benign and malignant lesions. Additionally, 3D PAI can also be developed to reveal more comprehensive information of lesions.

CHAPTER 5 3D PA/US FUNCTIONAL IMAGING OF BREAST CANCERS

In this chapter, 3D PA/US functional imaging on breast cancer was investigated. The common imaging modalities for diagnosis of breast cancer are first reviewed. Next, the 3D PA/US functional imaging system updated from 2D PA/US imaging system described in Chapter 2 is introduced. With the updated 3D PA/US functional imaging system, we carried out the clinical study where 24 patients with either benign breast tumors or malignant breast tumors were enrolled. Quantitative analysis was performed on the SO_2 values obtained from 3D PAI results of 24 patients. We found that the SO_2 values in both intra-tumor regions and peri-tumor regions of malignant cases were significantly higher than those of benign cases. These results demonstrate that 3D PA/US functional imaging has the potential in aiding diagnosis of breast cancer with a robust quantitative analysis.

5.1 Background

Among the female population worldwide, breast cancer is most common and accounts for around 14.6% of all new cancer cases in the United States in 2019[66]. It is important to detect breast cancer in the early stage (T1 stage) because it can lower mortality and burdens on society as a whole[67]. Two most widely used imaging modalities for detecting breast cancer are X-ray mammography and breast ultrasonography (US)[68]. Ultrasound is noninvasive and

is suitable for detecting lesions especially in dense breasts[69]. Mammography is superiorly sensitive to the microcalcifications[70] but is radioactive and not suitable for dense breasts. Both of the US detection and X-ray screening are playing important roles in diagnosis of breast cancers, however, to further improve the diagnosis accuracy of breast cancer especially the diagnosis accuracy of early stage ones is still desired because it can reduce the unnecessary biopsy of benign lesions[71].

During the past decade, PAI of breast cancer has gained lots of interest for the following reasons: 1) PAI utilizes optical contrast in imaged tissue and thus can reveal complementary biological information for other imaging modalities; 2) PAI is highly sensitive to vessels due to the strong optical absorption of the intra-vascular hemoglobin[7,72,73]. Microvascular information is of vital importance because it is highly related to tumor angiogenesis and metastasis [74,75]; 3) When employing multispectral PAI, functional information such as SO_2 can be obtained, providing essential information for evaluating metabolism levels of lesions as well as therapeutic response. Owing to these unique advantages, PAI has made significant progresses in clinical studies of breast cancer[29,39,76-78].

Among all the PAI systems developed for breast cancer imaging, the combination of PAI with handheld US systems has attracted lots of interest especially in clinical studies[14,29,79,80]. The integration has the advantage of operational convenience because the operators are already very familiar with traditional US imaging. In addition, by overlaying PAI results on

traditional US imaging results, vascular structure in PAI can be well located with anatomical structure obtained in US imaging. Due to the above advantages, integrating PAI with handheld US has achieved many progresses in diagnosis of breast cancer[11,29]. One of the most prominent studies was a multi-central study reported in 2018[11]. In this study, 2105 subjects were enrolled for multispectral PA/US imaging. The results demonstrate that PA/US can increase the specificity in diagnosis of breast cancer compared with pure US[11]. In another study enrolling 7 breast cancerous patients and 6 healthy volunteers, optically absorptive components including oxy-hemoglobin (Hb), deoxy-hemoglobin (deHb), total hemoglobin (tHb) were resolved[29]. The comparison between breast cancerous cases and healthy breast cases reveals that Hb, deHb and tHb are more abundant in invasive carcinoma than in unaffected breast tissue and peritumoral tissue.

Most of the above pioneer clinical studies relied on 2D PA/US imaging. However, with 2D imaging, important values from other cross-sections of lesions may be missed. Instead, with the aid of 3D imaging, more comprehensive information of tumor can be obtained. Specifically, when combining 3D US imaging with 3D functional PAI, volumetric functional information such as volumetric mean SO_2 value can be calculated. Moreover, with the aid of 3D US imaging, intra-tumor regions and peri-tumor regions can be analyzed separately, which may potentially improve the diagnosis accuracy of breast cancer[81]. Additionally, with the analysis of the imaged regions as a whole, variance between different cross-sections can be

reduced and direct quantitative analysis can be applied without having to select 2D B-scan slices. Furthermore, 3D morphological distribution of vessels can contribute to a more comprehensive assessment of blood supply in and surrounding lesions. Although the feasibility of 3D PA/US imaging has been verified by either scanning a linear probe or by utilizing a 2D array [82-84], few of them has been applied to breast imaging.

In this study, we developed a 3D PA/US functional imaging system, which was updated from the 2D PA/US imaging system described in Chapter 2. With the 3D PA/US functional imaging system, we performed 3D PA/US functional imaging on patients with either benign breast tumors or malignant breast tumors. The main purpose of this study is to explore the potential value of quantitative analysis with 3D PA/US functional imaging in achieving a higher diagnosis accuracy of early breast cancer.

5.2 3D PA/US functional imaging system

The dual-mode imaging system in this study was based on a high-end clinical US machine (Resona 7, Mindray Bio-Medical Electronics Co., Ltd., China)[47] , which had the ability to perform parallel data acquisition required by PAI as introduced in Chapter 2. PA images were reconstructed in real time with the delay and sum algorithm. The linear probe (L9-3U, Mindray Bio-Medical Electronics Co., Ltd., China) with 192 elements and a center frequency of 5.8 MHz was employed for acquisition of PA and US signals. To perform

multispectral PAI, an OPO tunable laser (Spitlight 600-OPO, Innolas laser GmbH) which could generate 700-850 nm laser pulses at 10 Hz was integrated with the US system. In our study, 750 nm and 830 nm were used for PA functional imaging. 750 nm and 830 nm were chosen because deHb has stronger absorption at 750 nm and Hb has stronger absorption at 830 nm[85] (see Fig5.2). The higher difference in absorption between deHb and Hb would be beneficial for SO_2 calculation. Additionally, the power of the OPO laser is spectrally varied as shown in Fig5.2. At 750 nm and 830 nm, the pulse energy is still high enough to achieve good signal to noise ratio (SNR).

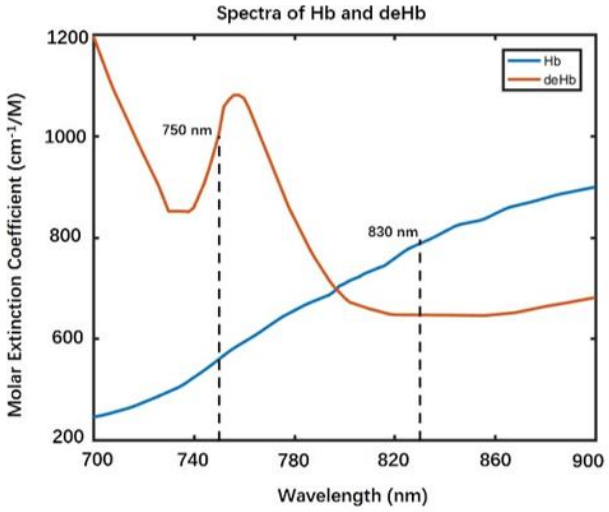

Fig5.1 Spectra of Hb and deHb between 700 nm and 900 nm[85].

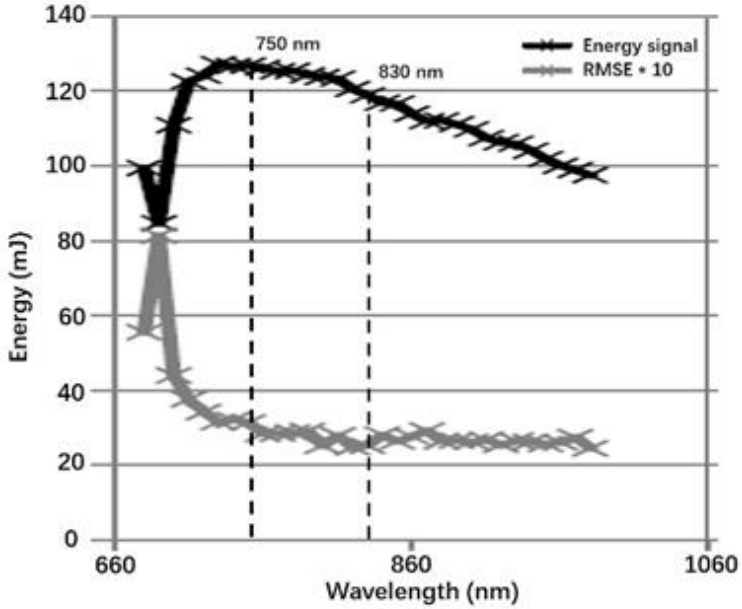

Fig5.2 Energy-wavelength curve of the OPO laser.

To achieve PA/US real time imaging at two wavelengths, a time division multiplexing approach was employed. SO_2 map was represented together with PA images at two wavelengths at 5 Hz frame rate. The photographs of the imaging system and the 3D scanning device are presented in Fig5.3 (a) and Fig5.3 (b) respectively.

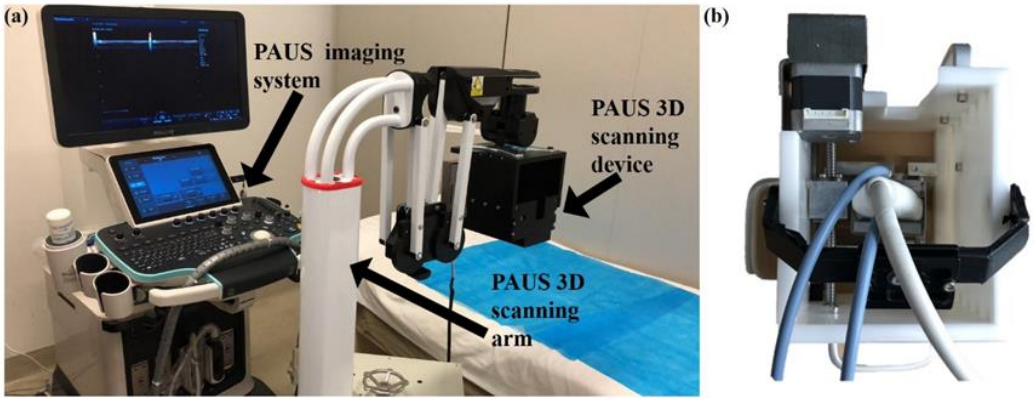

Fig5.3 (a) 3D PA/US dual mode imaging system. (b) 3D scanning device.[86]

The 3D scanning device fixed on the 3D scanning arm included a probe holder and an electric motor (Fig5.3 (a)). By scanning the probe across the breast skin surface, a local 3D PA/US functional imaging can be performed. The electric motor moved at a steady velocity (1mm/s) during 3D imaging, while a set of 2D US and PA images at 750 nm and 830 nm were acquired at 0.2 mm step intervals simultaneously (see Fig5.4).

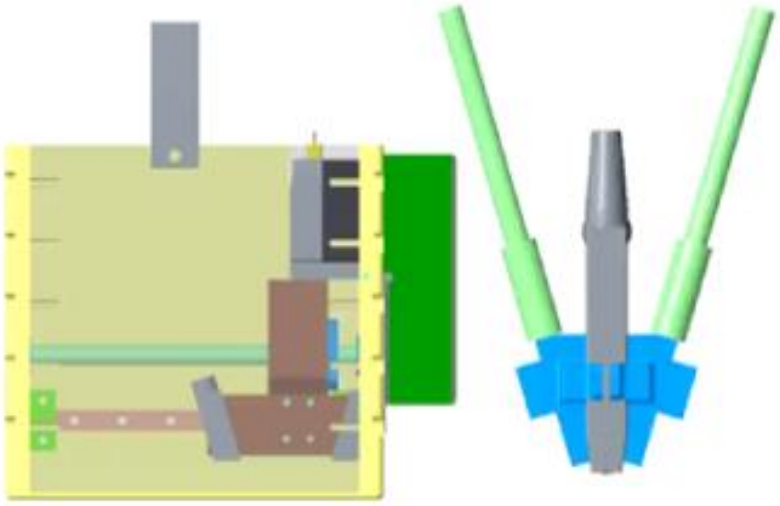

Fig5.4 Design of 3D imaging device in SOLIDWORKS.

The total scanning length was 4 cm and the total scanning time was 40 seconds. After the scanning ended, the 3D imaging results were downloaded and analyzed off line.

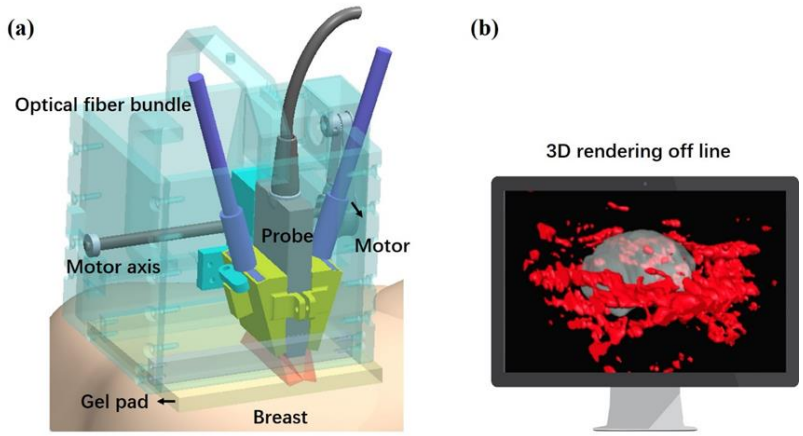

Fig5.5 (a) Schematic diagram of 3D scanning device. (b) 3D rendering of vascular networks co-registered with the tumor surface.[86]

To render 3D PA/US images (Fig5.3 (b)), we first imported a set of 2D SO_2 maps into Amira (version 6.0, Visage Imaging) to obtain the 3D SO_2 map. Next, we extracted SO_2 values larger than 40% and less than 100% from the 3D SO_2 map to obtain vascular networks. A threshold of 40% was set because according to previous studies, SO_2 values in breast tumors normally do not go below 40%[78,87,88]. Besides, due to the fact that the patients with malignant breast tumors enrolled in this study were all at T1 stage (see Section 5.4), abnormal SO_2 values caused by necrosis would not present in this study. To render tumor regions together with 3D vascular networks, the surfaces of the tumor regions were first marked manually based on US images and then co-registered with the 3D vascular networks with a certain degree of transparency.

5.3 Quantification analysis strategy

The dominant endogenous photo absorbers in the near-infrared range are Hb and deHb[8]. At location $\boldsymbol{r}$, PA signals at optical wavelength λ_i can be described as Eq. (5.1)[89]. In this equation, Γ is the Grüneisen parameter of the tissue. $F(\lambda_i, \boldsymbol{r})$ is the optical fluence at optical wavelength λ_i. $C(Hb, \boldsymbol{r})$ and $C(deHb, \boldsymbol{r})$ are the concentrations of Hb and deHb, respectively. $\varepsilon_{Hb}(\lambda_i)$, $\varepsilon_{deHb}(\lambda_i)$ are the known molar extinction coefficients of Hb and deHb at wavelength λ_i.

$$PA(\lambda_i, \boldsymbol{r}) = \Gamma F(\lambda_i, \boldsymbol{r})(C(Hb, \boldsymbol{r})\varepsilon_{Hb}(\lambda_i) + C(deHb, r)\varepsilon_{deHb}(\lambda_i)) \quad (5.1)$$

Due to the fact that at 750 nm and 830 nm, both of the absorption coefficient $\mu_a(\lambda)$ and the reduced scattering coefficient $\mu_s'(\lambda)$ of the background breast tissue are similar[90,91], the optical fluence $F(\lambda_{750nm}, \boldsymbol{r})$ and $F(\lambda_{830nm}, \boldsymbol{r})$ were assumed to be approximately same after normalization with the real-time recorded illumination power of laser pulses at each wavelength. Given the definition of SO_2 as follows,

$$SO_2(\boldsymbol{r}) = C(Hb, \boldsymbol{r})/(C(Hb, \boldsymbol{r}) + C(deHb, \boldsymbol{r})) \quad (5.2)$$

the SO_2 at each pixel can be derived from PA values at 750 nm and 830 nm, as shown in Eq. (5.3)[92]. Negative SO_2 values were excluded in the later analysis due to the lack of physical meaning.

$$SO_2(\boldsymbol{r}) = \frac{PA(\lambda_{750nm},\boldsymbol{r})\varepsilon_{deHb}(\lambda_{830nm}) - PA(\lambda_{830nm},\boldsymbol{r})\varepsilon_{deHb}(\lambda_{750nm})}{PA(\lambda_{750nm},\boldsymbol{r})(\varepsilon_{deHb}(\lambda_{830nm}) - \varepsilon_{Hb}(\lambda_{830nm})) + PA(\lambda_{830nm},\boldsymbol{r})(\varepsilon_{Hb}(\lambda_{750nm}) - \varepsilon_{deHb}(\lambda_{750nm}))} \quad (5.3)$$

To analyze intra-tumor regions and peri-tumor regions separately, tumor contours in 2D US slices were first marked manually by experienced physicians. 3D tumor boundaries were then obtained from a set of 2D US slices. To automatically extract peri-tumor regions, we proposed a method based on automatically calculating the least volume ellipse (LVE) enclosing the 3D tumor regions in MATLAB (MathWorks, Inc.)[93]. Similar methods have been verified in semi-automatically estimating tumor volumes in CT[94]. Due to the uniqueness of LVE enclosing the 3D tumor regions, the analysis process is robust and repeatable. After obtaining the LVE, the extensional ellipse was calculated by extending each length of three axes of the original LVE by 1.2 times. We defined regions inside the extensional ellipse and outside the tumor regions as the tumor surrounding regions (Fig5.6). After obtaining the intra-tumor region and the tumor surrounding region of each tumor, volumetric mean SO_2 in each region was calculated through dividing the sum of SO_2 values within the range of 40% and 100% by the pixel numbers where SO_2 values were within the same range. Similarly, we also calculated volumetric mean SO_2 values in symmetrical regions of lateral healthy breasts.

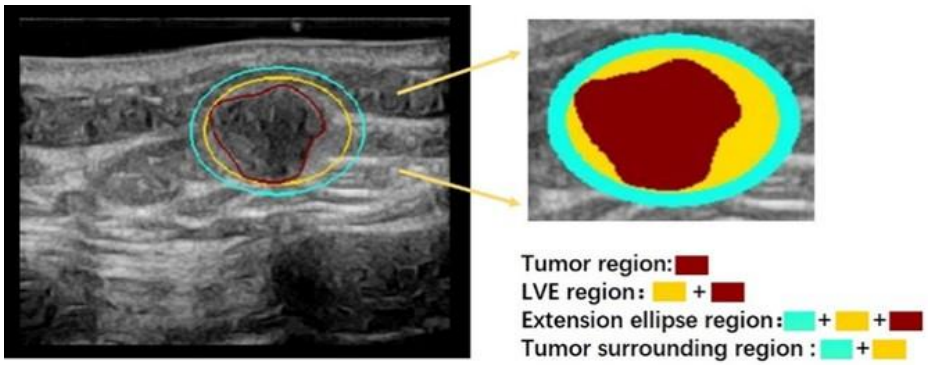

Fig5.6 Representation for definitions of tumor and tumor surrounding regions.[86]

5.4 Patients enrollment and imaging procedure

Patients with breast tumors were consecutively recruited from the outpatients and inpatients of breast surgery department at Peking Union Medical College Hospital (PUMCH) in from November 2017 to January 2018. The enrollment criteria included: 1) the maximum diameter of the lesion was smaller than 2 cm; 2) the patients received a BIRADS rating from 3 to 5 with indication for surgery or biopsy; 3) tumor boundaries were clear in US imaging. Our study protocol was approved by the institutional ethics committee of Peking Union Medical College Hospital. Written informed consent was obtained from all participants.

Imaging examinations via US and/or X-ray mammography, MRI by experienced radiologists were first performed on all patients. After the conventional US imaging was performed, 2D and 3D PA/US dual mode imaging were performed. It should be noted that patients with BIRADS 3 were all found to have an increasing size of tumor in follow-up visits and thus were highly suspicious before biopsy. The flow chart of the imaging procedure was

summarized as Fig5.7 shown.

In total, 16 patients with T1 stage invasive breast cancers (IBCs) and 8 patients with either breast fibroma or breast adenosis were included in the following analysis. In addition to 16 T1 stage IBCs and 8 benign lesions of these 24 patients, PAI results of 22 contralateral healthy breasts were also analyzed, with 14 of them from patients with T1 stage IBCs, and 8 of them from patients with benign lesions. Two contralateral breasts were excluded due to the existence of lesions inside.

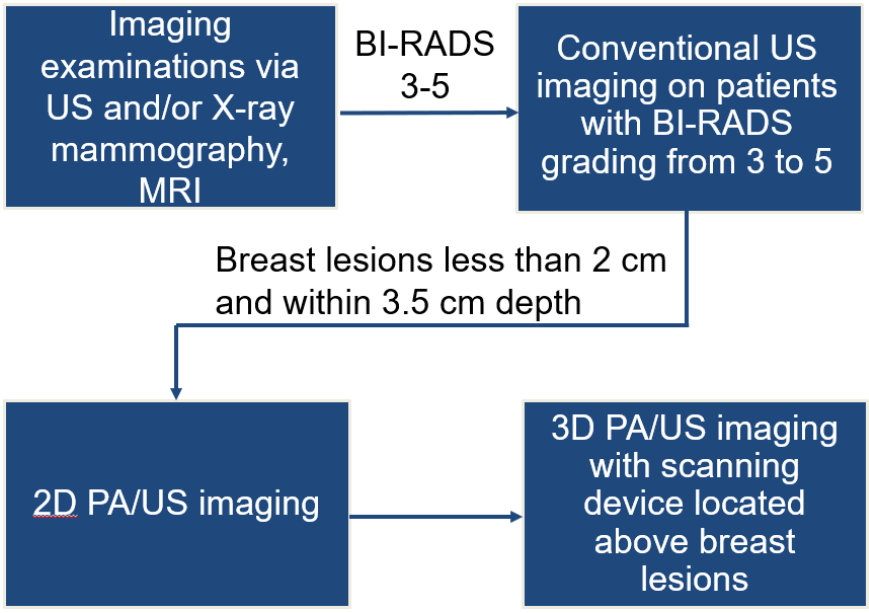

Fig5.7 Flow chart of the imaging procedure

5.5 Statistical analysis

Detailed information of these 24 patients was listed in Appendix A. All of the imaging

results were grouped into three categories: benign group (either fibromas or breast adenosis, n=8), malignant group (T1 stage IBCs, n=16) and normal group (contralateral healthy breasts, n=22).

Because tumor size is also closely related to the malignancy of lesions, to reduce cofounding effects of tumor sizes, subgroup analyses were carried out. In each subgroup, only tumors with similar size were included. For example, 5 IBCs and 5 benign tumors with largest diameters ranging from 1 to 1.5 cm were included in one subgroup. For tumors with largest diameters between 1.6 cm and 2.0 cm, due to the mismatch in sample size between IBCs (10) and benign tumors (2), 2 out of 10 IBCs were randomly selected to form a subgroup with the two benign tumors. In total, there were 45 combinations to make sure each of 10 IBCs were selected at least once. Hence, we performed subgroup analyses 45 times for the size group where largest diameters of tumors were between 1.6 cm and 2.0 cm. Detailed information of tumor sizes and correspondent sample sizes in each subgroup was summarized in Table5.1.

Nonparametric two tails Mann-Whitney U-test was used to calculate the statistical significance between either two groups among benign, malignant and healthy groups. This statistical method was chosen because our sample size to small to meet the normal distribution requirement from traditional t-test statistical method. A P value of 0.05 was considered to indicate 95% statistical significance. We used the Hodges-Lehmann estimator to calculate the difference between two groups and the 95% confidence interval. The statistical analysis was

performed with MATLAB (MathWorks, Inc.).

Table5.1 Tumor size and correspondent sample size[86]

Size(cm)	Sample size of T1 stage IBCs	Sample size of benign tumors
[0.5, 0.9]	1	1
[1, 1.5]	5	5
[1.6, 2]	2(out of 10)	2

5.6 Results

5.6.1 Statistical results

Statistical results of the volumetric mean SO_2 from 3 groups (16 T1 stage IBCs, 8 benign lesions and 22 contralateral healthy breasts) were shown in Fig5.8.

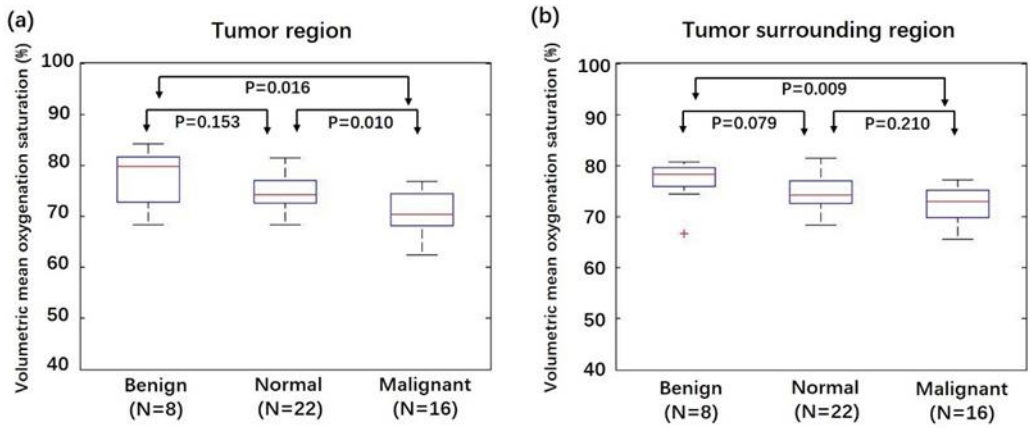

Fig5.8 (a) Box plots of volumetric mean SO_2 values of the benign, normal and malignant groups in tumor regions. (b) Box plots of volumetric mean SO_2 values of the benign, normal, malignant groups in tumor surrounding regions.[86]

As shown in Fig5.8 (a), in tumor regions, the SO_2 volumetric mean values of the

malignant group was 7.7% lower (95% confidence interval: 2.1%, 12.4%) than that of the benign group (P=0.016) and was 3.9% lower (95% confidential interval: 2.2%, 5.5%) than that of the normal group (P=0.010). In peri-tumor regions (Fig5.8(b)), the SO_2 volumetric mean values of the malignant group was 4.9% lower (95% confidence interval: 1.6%, 8.4%) than that of the benign group (P=0.009). Differences of SO_2 volumetric mean values between other groups such as the benign group and the normal group were not significant at the 95% level.

In the analyses of 47 subgroups with the control of tumor sizes, SO_2 volumetric mean values in both tumor regions and peri-tumor regions were found to be significantly lower in malignant tumors than in benign tumors. In tumor regions, the SO_2 volumetric mean value of the malignant group was at least 7.0% lower (95% confidence interval: 1.4%, 14.0%) than that of the benign group ($0.005 \leqslant P \leqslant 0.028$). In tumor surrounding regions, the SO_2 volumetric mean value of the malignant group was at least 4.0% lower (95% confidence interval: 0.5%, 9.3%) than that of the benign group ($0.010 \leqslant P \leqslant 0.028$).

By varying the SO_2 threshold both inside tumors (Fig5.9(a)) and in tumor surrounding regions (Fig5.9(b)), we obtained receiver operating characteristic (ROC) curves for differentiating malignant tumors from benign tumors.

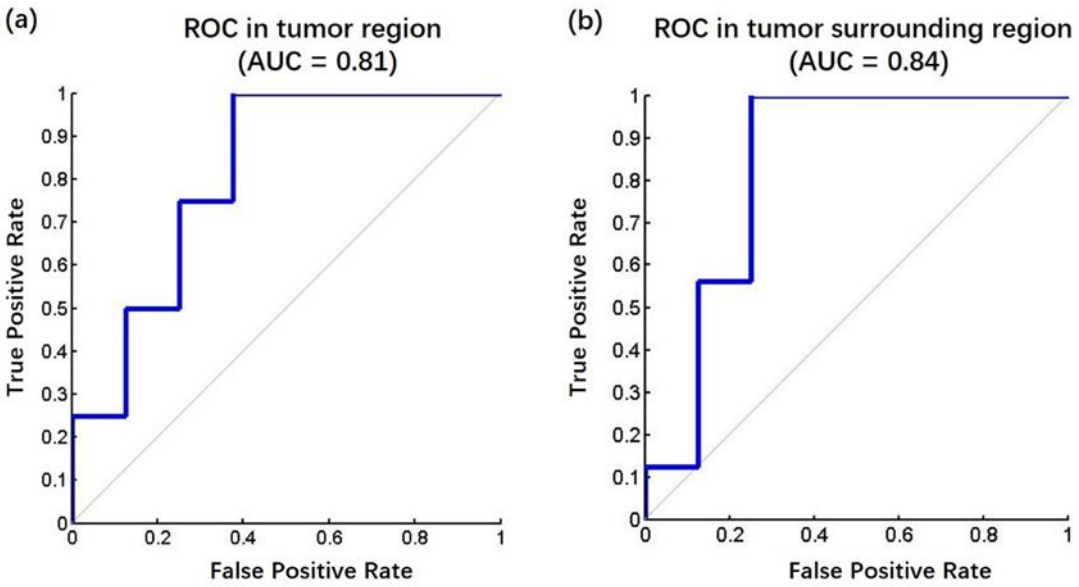

Fig5.9 ROC for differentiating malignant tumors from benign tumors by varying the SO_2 threshold in both (a) tumor regions and (b) tumor surrounding regions.[86]

With a cut off value of 78.2% for SO_2 value inside tumors, a sensitivity of 100%, a specificity of 62.5% were obtained. The area under the ROC curve (AUC) was 0.81. With a cut off value of 77.9% for SO_2 value in tumor surrounding regions, a sensitivity of 100%, a specificity of 75% and an AUC of 0.84 were obtained.

Similarly, for all 47 subgroup analyses with the control of tumor size, with a cut off value of 78.2% for SO_2 value inside tumors, an average sensitivity of 100%, an average specificity of 62.5% and an average AUC of 0.86 were achieved. With a cut off value of 77.9% for SO_2 value in tumor surrounding regions, an average sensitivity of 100%, an average specificity of 62.5% and an average AUC of 0.85 were achieved. These results show that the physiological information PAI provide has the potential to differentiate benign tumors from malignant ones

and thus to provide important complementary information to traditional US imaging.

We also performed statistical analysis on vasculature density in peri-tumor regions and intra-tumor regions because we did see a trend during the clinical study that the vessel density in malignant cases were higher than benign cases. Statistical results are shown as below:

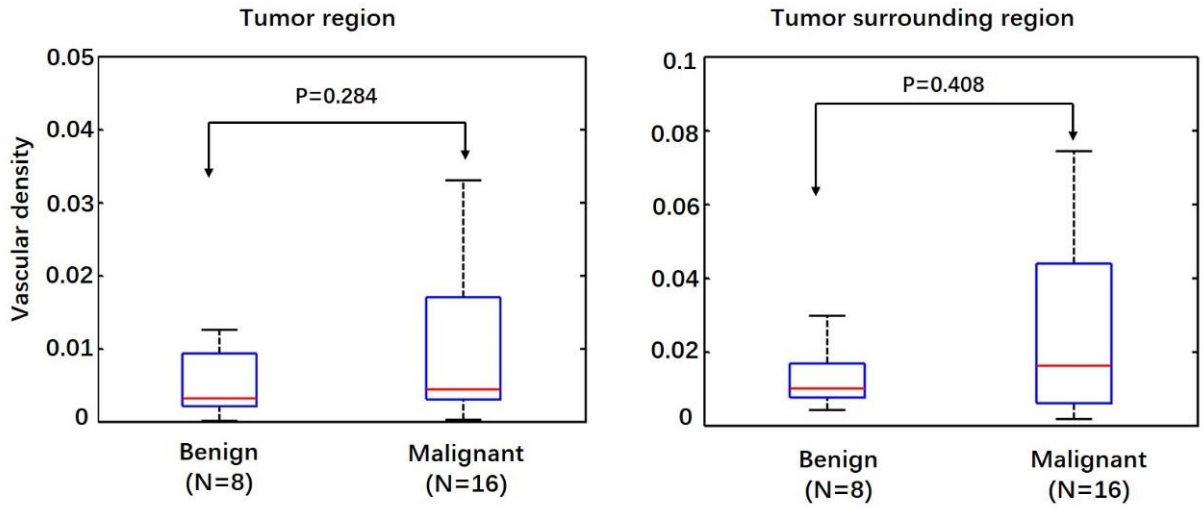

Fig5.10 Vascular density in tumor regions and tumor surrounding regions

From statistical result, we could see that although there is a trend that the malignant group has a higher vascular density than the benign group, there is no significant difference between two groups at 95% significant level. One potential reason is that the probe we used did not have a high sensitivity, which is extremely important for PAI because PA signals in deep tissue can be much weaker than traditional US signals. Another reason is that the sample size in our study is not big enough to achieve a statistical significance.

In addition, we found that the variance of malignant group was much higher than the benign group. This result suggests that the physiological information of malignant tumors may vary a lot from case to case.

5.6.2 PA/US imaging results

Representative imaging results of invasive breast cancers and benign breast lesions are shown in this section. The SO_2/US fused imaging results of a malignant tumor (IBC) and a benign tumor (fibroadenoma) are shown in Fig5.11 (a) and Fig5.11 (b), respectively. In the imaging result of the malignant tumor (Fig5.11 (a)), more abundant vasculatures and lower SO_2 values showed up in and surrounding tumor regions, while only a few vasculatures and relatively higher SO_2 values were revealed in the benign lesions (Fig5.11(b)). Based on the pure US imaging results, it was difficult to confidently grade the malignant tumor because it had a clear margin and a regular shape, which are typical characteristics of benign tumors.

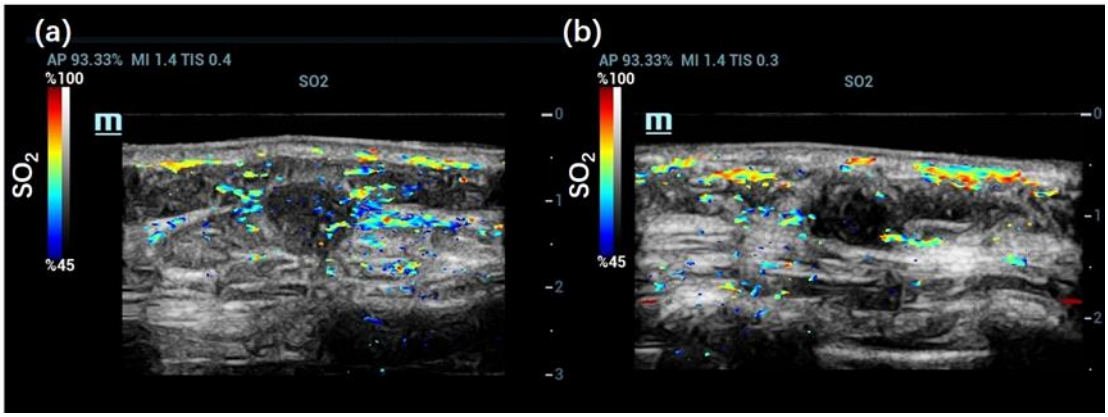

Fig5.11 2D SO_2/US imaging results of (a) an invasive breast cancer and (b) a breast fibroadenoma.[86]

In addition to 2D SO_2/US imaging results, X-ray mammography and CD31 immunochemistry (IHC) vascular staining results of the same cases are shown in Fig5.12. The malignant tumor could hardly be detected from X-ray results (Fig5.12 (a)) because neither obvious calcification nor clear margins showed up. From the X-ray results of the benign tumor (Fig5.12 (b)), it was also difficult to identify the lesion. Consistent with the 2D PA/US imaging results, more CD31 vascular staining showed up in and surrounding the malignant tumor (Fig5.12 (c)) than the benign one (Fig5.12 (d)) according to IHC vascular staining results.

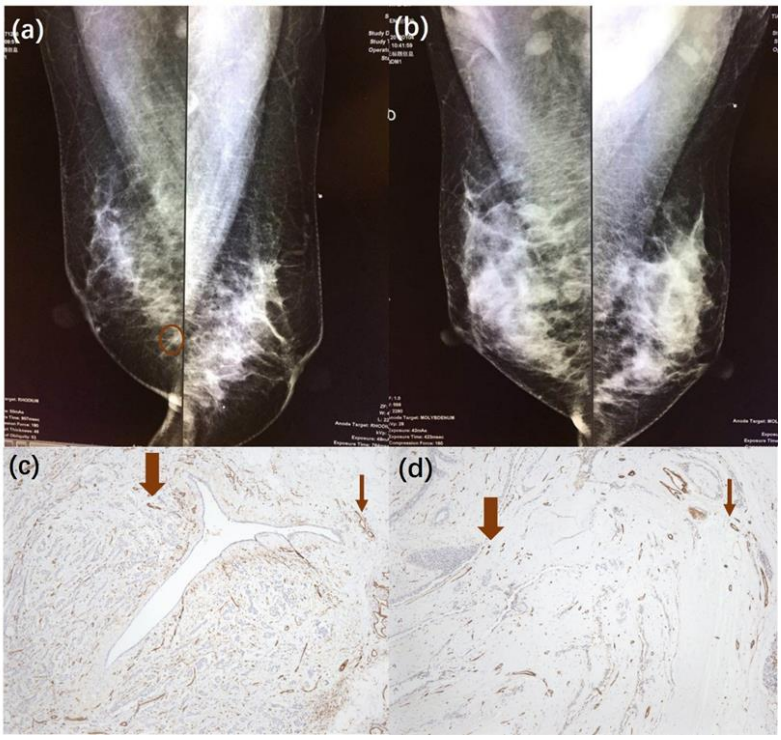

Fig5.12 X-ray mammography results of the same (a) invasive breast cancer and (d) breast fibroadenoma as in Fig5.11. CD31 immunochemistry (IHC) vascular staining results of the same (c) invasive breast cancer and (d) breast fibroadenoma as in Fig5.11. Both the tumor area (thick brown arrow) and the surrounding area were depicted (thin brown arrow).[86]

The 3D vascular networks of the same tumors shown above are presented in Fig5.13 (a, b). Similar with 2D imaging results, more abundant vasculatures showed up around the malignant tumor, whereas much less vasculatures showed up around the benign tumor. We also plotted the probability density distribution of SO_2 values in tumor regions and in tumor surrounding regions (see Fig5.13 (c, d)). The SO_2 distributions both inside and around the malignant tumor showed a lower trend than those of the benign tumor.

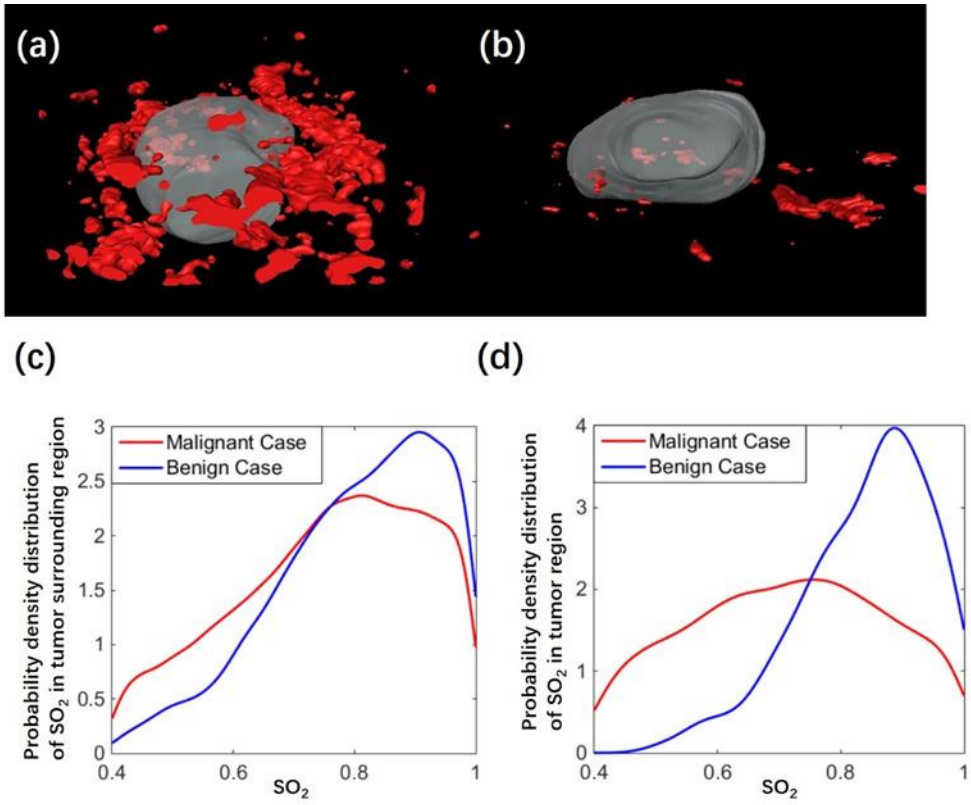

Fig5.13 3D vascular networks of the same (a) invasive breast cancer and (d) breast fibroadenoma as Fig5.11 showed. Probability density distributions of SO_2 values in the (c) tumor regions and (d) tumor surrounding regions of these two tumors.[86]

5.7 Summary and discussion

In this pilot clinical study, we performed 3D PA/US functional imaging on patients with small breast tumors (less than 2cm). From imaging results, we found that conventional US imaging could clearly display the edge of breast tumors, even for some lesions that were not easy to detect with X-Ray, as shown in Fig5.12(b). Besides, from 3D vasculature map shown in the benign case and the malignant case, we could see a trend that the vasculature was more abundant in the malignant case than the benign case. The reconstruction of 3D vasculature map could provide an intuitive assessment of the vasculature distribution of the benign case and the malignant case.

Because in this study, we mainly focused on what value could quantification of PAI on breast cancer could provide, we did not perform a statistical analysis for 2D PAI results, although we did acquire them right before 3D PAI.

From statistical results, we found that invasive breast cancers had obviously lower volumetric mean SO_2 than the benign group or the healthy group. With the SO_2 cut-off values described in Section 5.6.1, the sensitivity and specificity in differentiating T1 IBC from benign tumors were favorable.

Although we had performed an analysis for vasculature density in intra-tumor regions and peri-tumor regions, no significant difference was found between the malignant group and

the benign group even though we did see a trend in two cases shown with results of 2D imaging and 3D vasculature information. We also found that, in the malignant group, the variance of vasculature density is much larger than that of the benign group. This observation suggests the complexity of using one physiological index to evaluate malignant cases. Although the future increase of the sample size may provide a much more concrete conclusion.

Based on the above statistical analysis, we could see that with PAI added to US imaging, more functional information, such as SO_2 distributions of tumors could potentially enhance the diagnostic confidence. However, the difference of SO_2 between the malignant group and the benign group we found was still not high enough to provide a very promising diagnosis accuracy. In the future, the combination of SO_2 with patterns of PA signals may have provide a more comprehensive information. Identifying patterns of PA signals will require the machine learning algorithms including patterns recognition. And similarly, increasing the sample size may also aid in identifying a much more confident SO_2 values.

We also compared our results with several previous studies. For the imaging ability of PA/US dual mode imaging system, our self-developed system was very similar to the PA/US dual mode imaging system made by Seno Medical Instruments Inc [11]. For the US imaging, because our method was based on a high-end clinical imaging system, the imaging quality of US imaging is very beneficial for physicians to perform US imaging and identify lesions with clear margins. In comparison, the imaging system developed by Seno Medical Instruments Inc

was developed mainly for PA imaging instead of US imaging, the imaging quality of US imaging may not be good enough for clinical physicians to identify a clear margin of the lesions. Besides, although we did not show CDFI results in this Chapter, we did have the imaging ability for CDFI, as shown in the clinical study of thyroid cancer. The additional information provided by CDFI may also provide more comprehensive information for diagnosis of diseases. For functional PAI, the imaging system provided by Seno Medical could present the hemoglobin concentration map and hemoglobin concentration map, while our system can directly provide the information of oxygenation saturation. Both of these two presenting methods have their unique advantages. For the system by Seno Medical, the imaging results were optimal for separating analysis of oxygenated hemoglobin and deoxygenated hemoglobin more intuitively. While our method provided a more intuitive way for evaluation of oxygenation saturation.

Additionally, our system was able to perform 3D imaging to provide a more comprehensive information, while their system could only perform 2D imaging. From the statistical assessment, physicians would score breast lesions just as they do in US imaging. This makes the performing PAI more operator-dependent, and thus may decrease the robustness of imaging explanation. While with 3D imaging, quantification analysis can be obtained directly with few operator-dependence. This would also benefit the advancement of PAI in the future because of the relatively uniform assessing criteria. Otherwise, it would

decrease the cost-effectiveness of PAI because it will request lots of training efforts for physicians to be familiar with the whole imaging procedure.

We also compared our results with previous research. We found that our results are in agreement with a previously reported clinical study in which 2D PA/US functional imaging were performed on more than 2000 breast tumors[11] with the PA/US system developed by . Their results found that SO_2 had a lower trend in malignant tumors than in benign ones. In another clinical study based on photoacoustic mammography, SO_2 values in the malignant tumors were found lower than in the normal breasts[78], which was consistent with our results.

The potential reasons for hypoxia in malignant tumors have been widely explored [95-97]. One predominant causative factor is severe structural and functional abnormalities in the tumor microcirculation. These abnormalities include dilations, and elongated or tortuous vascular networks. In addition to the significant difference of SO_2 values inside tumors, we also found a significant difference of SO_2 values in tumor surrounding regions. The mechanism behind this observation is not clear yet. Based on previous studies of breast contrast enhanced imaging, peripheral enhancement regions of breast tumors were found to be closely related to the malignity[98,99].

Compared to 2D functional PA/US imaging[11,29], 3D functional PA/US imaging can be advantageous for several reasons. First, 3D PA/US imaging could provide results for better

evaluation of the overall features of tumors. For instance, Fig5.14 displays the average SO_2 values in different 2D slices within the tumor region of a malignant case. We could see that the SO_2 values varied largely from slice to slice, and as a result, it is hard to select an appropriate 2D slice for evaluation of the tumor.

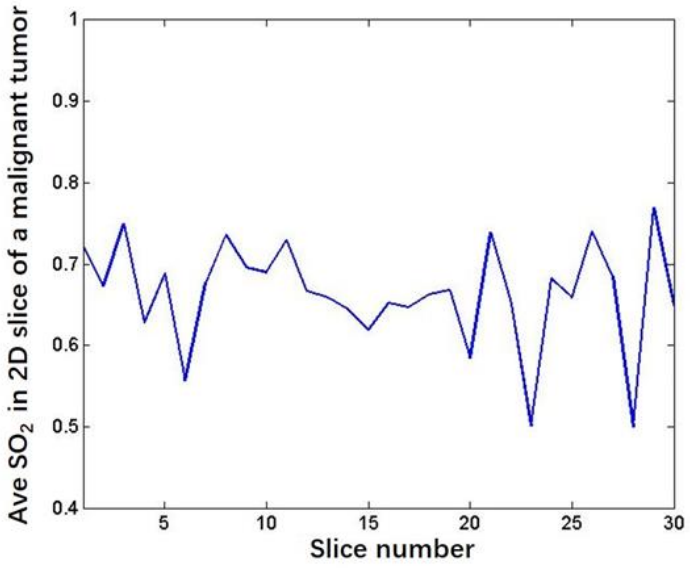

Fig5.14 Average SO_2 variation curve within different slices of a malignant tumor[86]

Second, compared to the PA scoring system dependent on manually scoring as in US imaging[11], quantification analysis with 3D PAI can avoid intra-observer difference and thus deliver a diagnostic index with better repeatability and reliability. Third, with 3D PA/US imaging, more comprehensive information including 3D distributions of vessel networks can be achieved.

There are also some limitations in this study. For example, due to the limited reception

angle of the straight linear probe, many of the reconstructed vessels tended to be parallel with the scanning direction. However, our study implies that even based on the "biased" reconstructed results, a valuable quantitative evaluation is still achievable. Besides, due to the difficulty in obtaining an accurate optical fluence map, calculation of hemoglobin concentration is not available yet. For further improvement, utilizing multiple wavelengths to assess the optical properties of background tissue may be available. With more confident optical properties, the diagnosis value of SO_2 can also be increased. Besides, it would also be possible to assess the accuracy of SO_2 when performing multi-wavelength PAI and get the optical spectrum of the regions where SO_2 values are calculated. If the measured spectrum is too different from the SO_2 values spectra based on spectra information of oxygenated-hemoglobin and deoxygenated-hemoglobin, then it is reasonable to suspect that the measurement of the SO_2 values is not accurate enough.

Finally, although our analysis demonstrates promising results that 3D PA/US functional imaging could potentially aid in diagnosis of breast tumors, an increase of overall sample size is necessary in the future for verifying a more accurate SO_2 cut-off value, which may further increase the specificity and the sensitivity.

CHAPTER 6 A COMPARISON BETWEEN SURFACE ACOUSTIC WAVES INDUCED BY LASER AND BY ARF

In this chapter, two generation mechanisms of surface acoustic waves (SAWs) are explored. The two generation mechanisms are optical excitation and acoustic radiation force (ARF) excitation, respectively. To track the propagation of SAWs, ultrafast ultrasound (US) imaging was employed. ARF-induced SAWs and laser-induced SAWs were first compared with a tissue-like phantom. Next, the frequency contents of SAWs generated by ARF and pulsed laser light were compared with the same excitation duration and different SAW bandwidths were observed. At last, the generation and the propagation of excited waves with the excitation regions below the surface were compared. Additionally, the relationship between shear wave amplitude and optical fluence were also investigated. The study presented in this chapter can potentially extend the applications of laser-induced SAWs in biomedical fields.

6.1 Background

Initially, generation of SAWs utilizing a pulsed laser beam was introduced to investigate mechanical properties of plates and thin metal films[100-102]. Typically, a laser pulse can be used to generate SAWs on the surface of the material and the subtle displacement at surface can then be detected with capacitance transducers, piezoelectric transducers, or

interferometers[102,103]. Applications of laser-induced SAWs have also been presented in studies of biological tissues[104-106]. For instance, several studies have shown that laser-induced SAWs can be utilized to investigate the stiffness of corneal ectasia[107-109]. In these studies, optical coherence tomography (OCT) was used for detection of the displacement induced by laser pulse on the corneal surface. The results demonstrate that imaging of laser-induced SAWs has the ability of measuring the stiffness of superficial tissue.

An alternative way to induce SAWs in soft tissues is to apply ARF with focused ultrasound beams at low frequencies[110-112]. In addition to imaging SAWs by OCT, ultrafast US imaging can also be employed with the same transducer used for generating ARF beams. The imaging depth of OCT is around 2 mm while the imaging depth of ultrafast US imaging can reach several centimeters. By transmission of plane or diverging waves, ultrafast US imaging is able to attain a frame rate higher than 1000 frames per second, which is high enough for capturing surface acoustic waves with velocities of several meters per seconds in typical soft tissues.

Laser-induced SAWs and ARF-induced SAWs have different characteristics. First, the generation mechanisms are different. With ARF excitation, SAWs are excited mainly due to a transfer of momentum from the propagating acoustic waves to the medium through attenuation or reflection of the ultrasonic wave[113]. Different from ARF excitation, generation of SAWs with pulsed laser light is mainly due to thermoelastic effects or ablation effects[114]. In this

chapter, we first investigated the differences of SAWs induced by ARF and SAWs induced by pulsed laser light in terms of propagation velocities and frequency components, respectively. Next, we explored the difference in wave generation between ARF excitation and laser light excitation when excitation regions were underneath the surface. Finally, we analyzed the relationship between the optical fluence and the shear wave amplitude. For both laser-induced SAWs and ARF-induced SAWs, ultrafast US imaging was employed for measurements of the propagation of SAWs.

6.2 Materials and methods

Three experiments were conducted in total with the aim of comparing two mechanisms from the following three perspectives: propagation velocity, frequency component, and wave generation when excitation regions were below the surface [115].

In the first experiment, the propagation velocities of SAWs generated in phantoms with different stiffnesses were compared. We prepared three phantoms with different stiffnesses by dissolving gelatin powder in distilled water with different concentrations: 6%, 9%, and 12% w/v. To provide optical absorption, we added 0.5% (w/v) graphite powder to solutions. Additionally, two percent (w/v) 60-120 μm silica particles were added to provide US scattering. The dimensions of each phantom were same: 6.2 cm × 5.1 cm × 5.1 cm (L × W × H).

To carry out ultrafast US imaging of SAWs, we employed a US, PA, and elasticity

imaging platform which was developed previously[116]. This platform was implemented on a programable US system (Vantage 256; Verasonics, Inc.). Laser pulse at 1064 nm wavelength with a pulse duration of 5 ns was provided by an Nd: YAG laser (Vibrant 532 I; Opotek Inc.). The laser was integrated with the imaging platform for the excitation of PA signals and photothermal SAWs. An optical fiber with a diameter of 1.5 mm was placed above the phantom for delivery of light. To acquire PA and US signals as well as provide the ARF push beam, a linear US transducer (CL 15-7; Philips Healthcare.) was employed. For acoustic coupling, we filled water between the transducer and the phantom surface. The system setup for the first experiment was shown below:

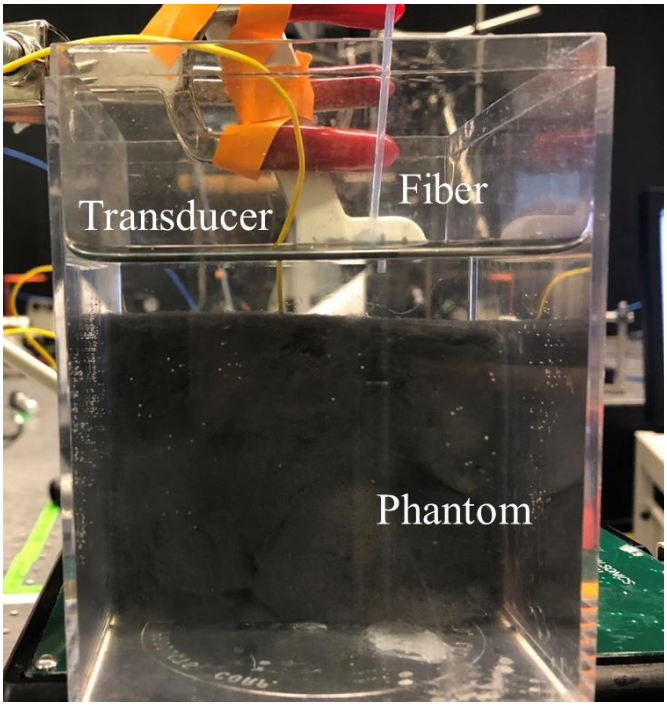

Fig6.1 The system setup for the first experiment, where the imaging target was a rubber phantom with graphite powder inside to provide optical absorption.

During the first experiment, we first performed PAI, and then ultrafast US imaging to track the laser-induced SAWs within and on the surface of the phantom. Particularly, we used the same laser pulse for generation of PA signals and for inducing subtle displacements, both of which were caused by photothermal effect. The propagation of SAWs was tracked by ultrafast US imaging starting 300 μs after the laser excitation. A total of thirty US images were captured at a frame rate of 3.3 kHz. After then, a 300 μs ARF pulse was emitted from the transducer to excite SAWs in the phantom. Another set of thirty ultrafast US images were acquired at the same frame rate right after the ARF push beam. To compare with laser-induced displacements, which mainly occurred at or near the phantom surface, ARF beam was also focused near the phantom surface (2 mm below the phantom surface).

After obtaining the ultrafast US imaging results, we calculated the SAW velocity for both mechanisms. First, displacement maps were obtained by correlating adjacent ultrafast US images along the axial direction. For calculation of SAW propagation velocities, we selected two points 0.2 mm below the phantom surface. The horizontal locations of these two points were set to be 3.57 and 4.43 mm away from the excitation region, resulting the distance between these two points being 0.86 mm. The rationale for choosing these two location was as follows: 1) To make sure that these two locations were away from the excitation region so that artifacts caused by laser or ARF pulse can be avoided; 2) To make sure that these two locations were still close enough to the excitation region so that we still obtained a high enough

signal-to-noise ratio (SNR). We then obtained the time-displacement curves at these two locations from displacement maps at different time points. The time delay of the SAWs propagating from one location to another was calculated with a correlation-based approach after interpolation with a time interval of 3 μs. Next, through dividing the distance between two points (0.86 mm) by the calculated time delay, we obtained SAW velocities.

SAWs generated here were essentially Scholte waves because the interface between water and phantom was fluid-solid interface. Based on previous research, the velocity of Scholte waves is 84% of the shear wave speed[117], thus we multiplied a factor of 1.19 to calculate the shear wave speed. We performed the laser/ARF SAW imaging on each phantom four times. To calculate the statistical significance in shear wave velocity (SWV) values, we applied a two-sided student t-test with MATLAB (MathWorks, Inc.) for both the laser-induced SAW imaging and the ARF-induced SAW imaging.

Next, in the second experiment, the spectra of ARF-based SAWs and laser-induced SAWs were compared. In this experiment, we made a phantom out of synthetic gel (Gelatin #5, Humimic Medical.). As in the first experiment, we added graphite powder with 0.5% (w/v) concentration for optical absorption. We also added 60-120 μm silica particles with a concentration of 2% (w/v) for ultrasound scattering. To match the ARF pulse duration and the optical excitation duration, another laser system (Quanta Ray; Spectra-Physics, U.S.) which could generate a 100 μs laser pulse at 1064 nm was used. For delivery of light, we placed a

300 μm diameter fiber on the edge of the transducer. At the phantom surface, the full width at half maximum (FWHM) of the laser beam was measured to be 400 μm. The optical fluence was 3.9 mJ/mm^2, well below the ANSI limit 5.5 mJ/mm^2 for the 100 μs laser pulse at 1064 nm[48].

We excited SAWs at the same location on phantom surface with the 100 μs ARF pulse and the 100 μs laser pulse separately. Ultrafast US imaging was performed immediately after the excitation pulse. The imaging frame rate was 3.3 kHz. As in the first experiment, we chose two locations for spectrum analysis. These two locations were 2.5 and 3.3 mm laterally away from the excitation region to allow attenuation of artifacts generated from the excitation center during excitation, and to maintain adequate SNR in measurements of displacement. We calculated displacement-time curves for these two regions after achieving the ultrafast US imaging results, and performed fast Fourier transform on them.

In the third experiment, the difference in SAW phenomenon with excitation location below the surface was investigated. As in the first two experiments, the phantom used was made out synthetic gel with dimensions of 4.9 cm × 4.9 cm × 3.7 cm (L × W × H). 2% (w/v) 60-120 μm silica particles were added to provide US scattering. Instead of adding gelatin powder for optical absorption, we placed a metal needle with 0.8 mm diameter 3.3 mm below the phantom surface. As a result, the excitation region was also 3.3 mm below the phantom surface. The metal needle could provide optical absorption due to the fact that metal is

generally highly absorbing[118]. The system setup is as following:

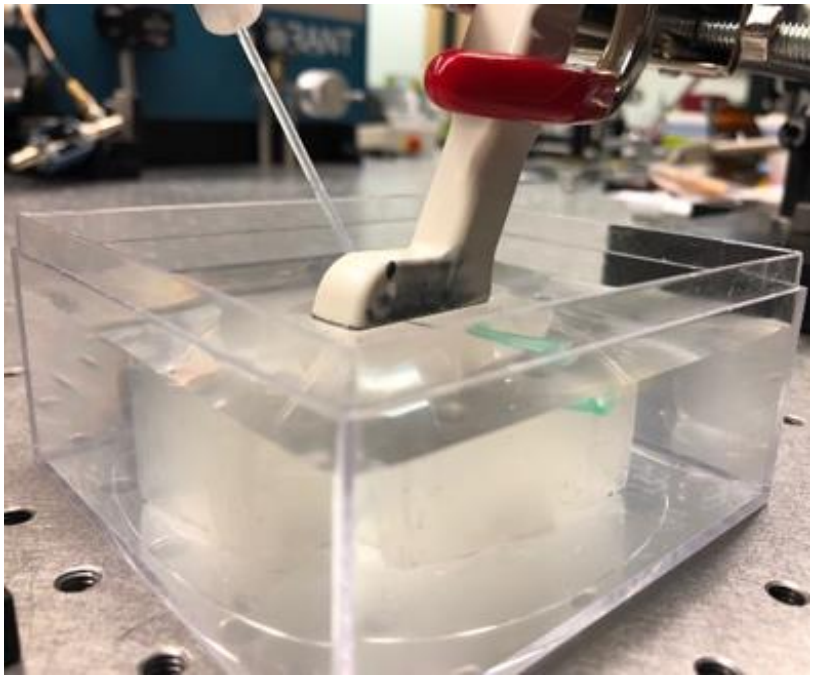

Fig6.2 System setup for the third experiment

We employed the same imaging system and the same laser system in the third experiment as in the first experiment. Fourteen ultrafast US images at a frame rate of 2.78 kHz were acquired 60 μs after the laser pulse. Next, we applied a 60 μs ARF pulse to the phantom. The US beam was focused 1.3 mm above the medal needle. Another set of fourteen ultrafast US images at a frame rate of 2.78 kHz were acquired right after the ARF pulse. In addition to investigate the difference in SAW phenomenon, we also explored the relationship between the optical fluence and the displacement amplitude. We applied three different optical fluences respectively: 46, 69, 92 mJ/cm^2. We repeatedly performed the ARF/laser SAWs imaging three

times for each fluence. The maximum amplitude of displacement was calculated 0.78 ms after the laser excitation in a region 3.3 mm below the phantom surface, same depth as the photoabsorber. Because SAW propagated in two opposite directions after excitation, there was a local maximum of displacement amplitude on both the left side and the right side of the photoabsorber. As a result, six measurements were carried out for each laser fluence in total. Detailed information of the system was listed in the following table.

Table6.1 Detailed information of the imaging system

US system	Model	Vantage 256, Verasonics
Transducer	Model	CL 15-7, Philips Healthcare
	Frequency range	15-7 MHz
Laser source	Model	Vibrant 532 I, Opotek Inc.
	Wavelength	1064 nm
	PRF	10 Hz
	Energy	40mJ/cm^2~100mJ/cm^2
	Pulse duration	5 ns
Ultrafast US imaging	Frame rate	2.78 kHz~3.3 kHz
ARF pulse	Duration	100 μs, 60 μs

6.3 Results

The co-registered PA/US imaging result of the 9% gelatin phantom in the first experiment was shown in Fig6.3[115]. PA signals in color scale demonstrated the location of laser excitation as well as the origin of photothermal expansion that induced following SAWs.

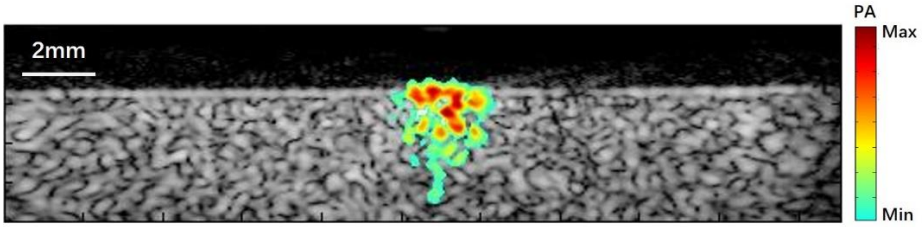

Fig6.3 Combined US (grayscale map) and PA image of the tissue-mimicking gelatin phantom.[115]

From Fig6.4, we could clearly see the propagation of laser-induced and ARF-induced SAWs in the displacement maps calculated from ultrafast US imaging results.

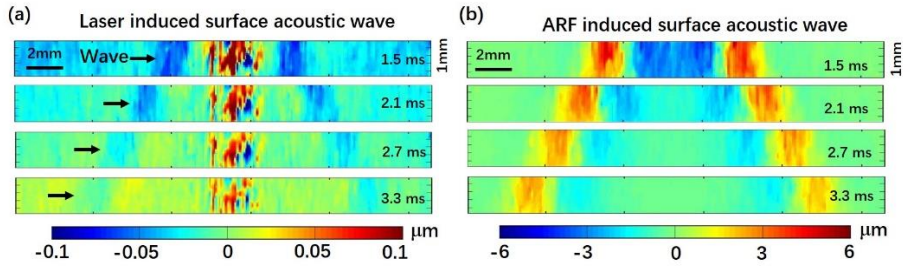

Fig6.4 Displacement maps at four different time points obtained using ultrafast US imaging for (a) laser induced SAWs and (b) ARF-based SAWs.[115]

SAW displacement was calculated at 1.5, 2.1, 2.7, and 3.3 ms after the laser/ARF excitation pulse. The displacement profiles of laser-induced SAWs and ARF-induced SAWs

were spatially matched. However, several differences also existed. First of all, the displacement at the excitation point was directed oppositely in laser-induced and ARF-induced SAWs. With laser excitation, the displacement at the excitation point was directed towards the imaging transducer while with ARF excitation, the displacement at the excitation point was directed away from the imaging transducer. The difference in the polarity of laser-induced SAWs and ARF-induced SAWs was due to the difference in the generation mechanisms. With ARF excitation, the initial displacement was caused by the push beam generated by the transducer, while with laser excitation, the initial displacement was caused by the photothermal expansion of the excited region. Secondly, the displacement amplitudes of laser-induced SAWs were much less than the displacement amplitudes of ARF-induced SAWs, with the former of which being on the order of tens of nanometers while the latter of which being several micrometers.

Fig6.5 showed the results of SWV measurements in phantoms with different stiffnesses[115].

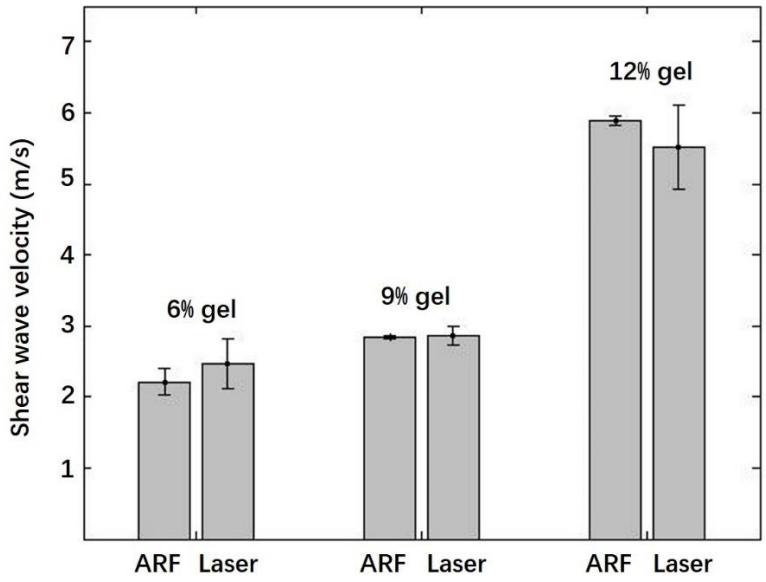

Fig6.5 SWV measurements (n=4) in gelatin phantoms of different gelatin concentrations and, therefore, different degrees of stiffness. Measurements were obtained using laser-induced SAWs and ARF-based SAWs. The mean SWV value is shown as a vertical bar, and 95% confidential interval is shown as an error bar.[115]

P values of the t test between the two methods were 0.13, 0.79, and 0.19 for 6%, 9% and 12% gelatin phantoms, respectively. There is no evidence to reject the null hypothesis that the mean values of the two measurement methods are equal. The statistical results shown in Fig6.5 demonstrate that laser-induced SAW imaging has the ability of quantifying SAW velocities and thus is capable of quantifying shear modulus of materials such as biological soft tissues with accuracy on par with ARF-induced SAW imaging.

Results from the second experiment are presented in Fig6.6 [115].

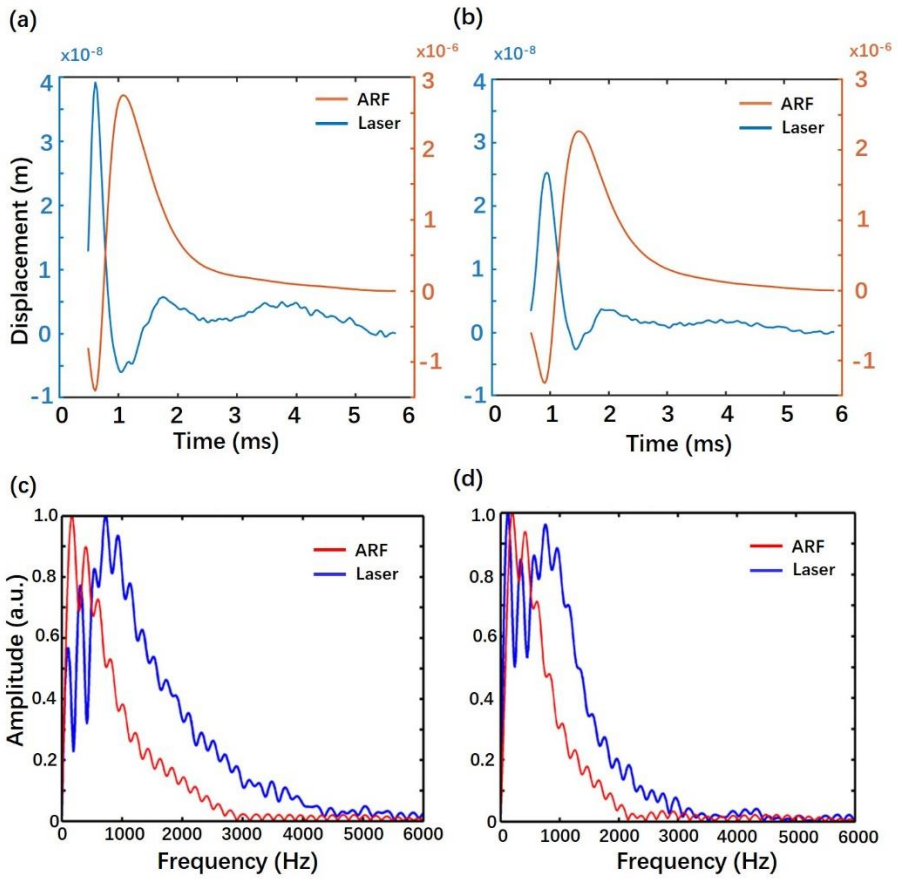

Fig6.6 Displacement-time curves of SAWs at (a) 2.5 mm and (b) 3.3 mm away from laser/ARF excitation region. The excitation occurred at time zero. Spectrums of displacement time curves at (c) 2.5 mm and (d) 3.3 mm away from laser/ARF excitation region.[115]

Fig6.6 shows the temporal behavior of SAW displacements induced by laser excitation or ARF excitation at two locations described in Section 6.2. The frequency spectrum of the displacement for both excitation sources at both positions were also plotted (Fig6.6 (c), (d)). Each displacement curve was averaged with five acquisitions using the same excitation and imaging parameters. At the first location which was 2.5 mm away from the excitation region, the center frequency of the displacement generated by laser pulse was 920 Hz with the 3 dB

bandwidth being 1310 Hz. At the second location which was 3.3 mm away from the laser excitation region, the center frequency of the displacement dropped to 767 Hz with the 3 dB bandwidth being 1062 Hz. In comparison, with ARF excitation, the center frequency and 3 dB bandwidth at the first location were 452 and 790 Hz, respectively. At the second location, the center frequency and 3 dB bandwidth dropped to 410 and 655 Hz, respectively. The slight attenuation of center frequency and 3 dB bandwidth from the first location to the second location is due to the fact that as SAWs propagate further, the higher frequency components attenuate more than lower frequency components. The difference between the center frequency and 3 dB bandwidth of laser-induced SAWs and ARF-induced SAWs were observed. Generally, given that the laser excitation region (FWHM of laser excitation beam: 400 μm) is smaller than the ARF excitation region (FWHM of ARF excitation beam: 1.34 mm), laser-induced SAWs can have a broader bandwidth than ARF-induced SAWs. This observation agrees with the theoretical relationships between the bandwidth and the spatial extent of the excitation[119]. Theoretically, the beam width for both the ARF-induced SAWs and laser-induced SAWs are determined by wavelength of excitation source and numerical aperture of the transducer or the objective lens used for generation of SAWs. For the same numerical aperture, optical wavelength can be much shorter than ultrasound wavelength. Thus, laser-based SAW imaging can provide a much smaller excitation beam. As a result, when SAW velocity is measured to infer the stiffness of the material, the broader bandwidth of SAWs

induced by laser excitation may provide better spatial resolution.

Next, we presented the results of the third experiment where we compared the wave propagation when both the laser excitation and the ARF excitation were below the surface. The location of the photoabsorber embedded 3.3 mm below the phantom surface can be seen in the PA/US imaging result (Fig6.7 (a)). Displacement maps at three time points after the laser pulse or ARF pulse are presented in Fig6.7 (b) and (d). From the displacement maps obtained with the laser-induced SAWs imaging method, both SAWs and shear waves were successfully induced.

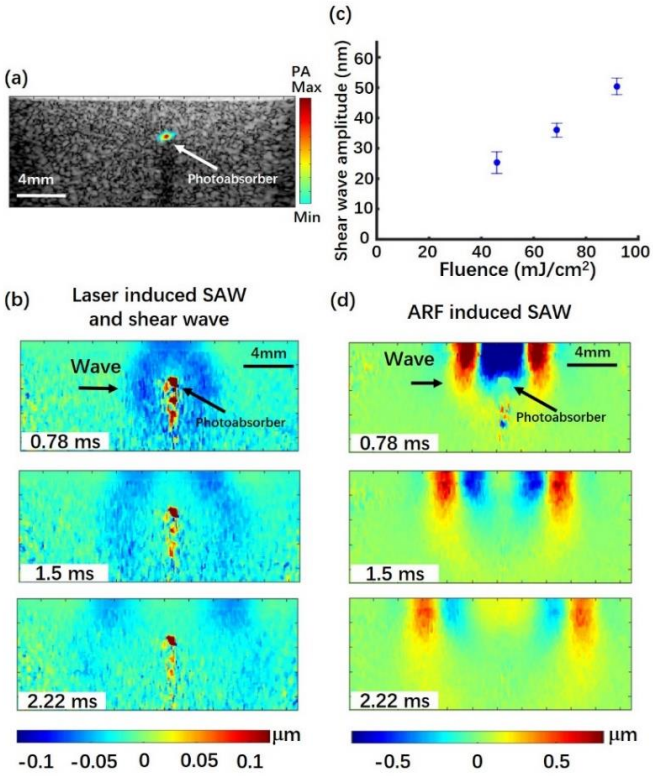

Fig6.7 (a) PA/US imaging result of the phantom with a photoaborber located 3.3 mm below

the surface. (b) Laser-induced SAW and shear wave displacement maps in the phantom at three different time points. (c) Scatter plot of mean value of shear wave displacement amplitude, measured 0.78 ms after the laser pulse, as a function of optical fluence. The error bars show standard deviation (n=6). (d) ARF-induced SAW displacement maps in the phantom at three different time points.[115]

Particularly, the SAWs and shear waves started to propagate separately at 1.5 ms after the excitation. This result demonstrates that in addition to superficial measurements of mechanical properties of materials, the applications of laser-induced SAW imaging can be potentially extended to measuring mechanical properties of materials at depth. Moreover, because of the straightforward relationship between shear wave velocities and the shear modulus of the measured material, shear wave velocities are generally more preferred than SAW velocities when deriving stiffness information of the material[120]. For ARF-induced SAW imaging, because the focus of the push beam had a small depth (2 mm below the surface), energy mainly remained in the surface region of the phantom, limiting the elastography analysis only to the surface layer.

In the third experiment, we also investigated the relationship between the optical fluence and the amplitude of laser-induced shear waves. Three optical fluences ranging from 46 to 92 mJ/cm^2 were applied. The optical fluence and the corresponding amplitude of laser-induced shear wave were presented in Fig6.7 (c). Clearly, the optical fluence has a linear relationship with the amplitude of laser-induced shear waves (R^2 = 0.93), suggesting that with higher optical fluence, larger shear wave amplitude and thus higher SNR can be achieved. However,

it's worth noticing that the energy applied here is below maximum permissible exposure for skin, which is 100 mJ/cm^2 for 1064 nm wavelength based on the American National Standard Institute[48]. According to a previous study, two regimes can generate SAWs with laser excitation: ablative regime and thermoelastic regime. In the ablative regime, amplitudes of displacements have a quadratic relationship with optical fluence. In this scenario, displacements can reach several micrometers. In the thermoelastic regime, displacements are linearly dependent on energy and can only reach tens of nanometers, which is in agreement with our observations (Fig6.7 (b), (c)).

6.4 Summary and discussion

In this chapter, we conducted three experiments to investigate differences in laser-induced SAWs and ARF-induced SAWs. In conclusion, we observed several differences in two generation mechanisms from each of the experiment. First, due to the difference in generation mechanism, the polarities of SAWs induced by laser excitation and ARF excitation are opposite. Second, the amplitudes of SAWs in two methods are different. Generally, the amplitude of ARF-induced SAWs is one to two orders of magnitude larger than the amplitude of laser-induced SAWs. The limitation of the amplitude of laser-induced SAWs is mainly due to the safety concern. When applying optical fluence higher than ANSI safety limitation, the laser excitation may cause ablation and thus may induce damage on the material. For biological tissues that cannot provide sufficient optical absorption, an external acoustically

friendly photoabsorber can be placed at the surface of the tissue to amplify SAW amplitude and simultaneously protect the underneath tissue from ablation[105]. Third, with laser excitation, it is feasible to induce perturbation within a much smaller region than with ARF excitation due to the difference in the size of the laser beam and the ARF beam. SAWs with higher bandwidth can thus be generated from laser excitation to potentially increase the spatial resolution of SAW velocity map. At last, when laser excitation region is located below the surface, both SAWs and shear waves can be generated, extending the application of laser-induced SAWs from the super facial regions to regions at depths. Besides, amplitude of laser-induced shear waves is linearly related to optical fluence.

CHAPTER 7 CONCLUSION

As an emerging technology, PAI has been proved to be a promising imaging modality. Previous clinical studies based on PAI have demonstrated the potential of PAI in multiple clinical applications, including cancer detection, arthritis evaluation, and vessels visualization.

In this thesis, the representative research of PAI systems in clinical studies has been reviewed first. After then, the development of a 2D PA/US imaging system based on a high-end handheld US imaging system is presented. The imaging capability of the system was verified by both of the phantom study and the in vivo study on the human forearm. Next, an optical fluence compensation method for handheld PA/US dual mode imaging is introduced. The efficiency of the proposed method was demonstrated through the phantom study and the in vivo study of a healthy breast.

Next, PA/US imaging of thyroid nodules was performed with the self-developed 2D PA/US imaging system. In total, 10 thyroid nodules were imaged with PA/US imaging and CDFI. The comparison between the PAI and CDFI demonstrates that PAI is able to provide more abundant vascular information than CDFI.

After then, the 2D PA/US imaging system was updated to the 3D functional PA/US imaging system. Particularly, the laser source was replaced with an OPO laser, which could

generate laser pulse at wavelengths from 700 to 850 nm. For 3D imaging, a 3D scanning device was designed to move the linear transducer across the imaging region. Additionally, the updated PA/US imaging system was able to perform real time imaging.

With the updated 3D functional PA/US imaging system, we carried out 3D functional PA/US imaging of breast tumors. A total of 24 cases including both benign breast tumors and malignant breast tumors were included in this clinical study. To perform the quantification analysis, we proposed an algorithm to analyze the volumetric mean SO_2 in intra-tumor regions and in peri-tumor regions. The statistical results showed that the SO_2 volumetric mean value of the malignant group was 7.7% lower than that of the benign group (P=0.016) and was 3.9% lower than that of the normal group (P=0.010). In peri-tumor regions, the SO_2 volumetric mean value of the malignant group was 4.9% lower than that of the benign group (P=0.009). These results demonstrate that 3D functional PA/US dual mode imaging has the potential to differentiate benign breast tumors from malignant ones. With the aid of 3D functional PA/US imaging as a complementary imaging modality, the diagnosis efficiency of breast cancer can be potentially improved.

At last, the author presented the study conducted in Georgia Institute of Technology. This study was motivated by the thought that in addition to PA signals, pulsed laser light may also induce shear waves or SAWs, the velocity of which can be used to infer stiffness information of imaged tissue. Specifically, with the aid of ultrafast US imaging, we compared laser-induced

SAWs with ARF-induced SAWs, which is more commonly applied for measurements of tissue stiffness in previous studies. Our results demonstrate that the laser-induced SAWs imaging can be applied to measure tissue stiffness with the accuracy on par with ARF-induced SAWs imaging. Additionally, the bandwidth of laser-induced SAWs can be larger than that of ARF-induced SAWs when laser beam size is much smaller than ARF beam size and as a result, laser-induced SAWs imaging has the potential to provide higher spatial resolution. At last, with the laser excitation located underneath the surface, both SAWs and shear waves can be generated, extending applications of laser-induced SAWs imaging from superficial regions to regions in depths.

7.1 The major novelties of this thesis

In this thesis, the author has presented a series of studies on handheld PA/US dual mode imaging in terms of system development, algorithm design, and clinical applications. The major novelties of this these are summarized as follows:

1. The 2D handheld PA/US imaging system and the 3D functional PA/US imaging system developed in this study can be applied to perform PA/US imaging in clinical studies. Specifically, the 3D functional PA/US imaging system offers a solution to perform quantified 3D PA/US imaging.

2. The optical fluence compensation method designed for handheld PA/US dual mode

imaging is introduced. The efficiency of the proposed method was verified with both the phantom study and the in vivo study. The results demonstrate that the proposed method could aid in regaining PA signals from deeper regions (2~3 cm).

3. 2D PA/US imaging of thyroid cancers was performed for the first time. The comparison between PAI and CDFI suggests that PAI could provide more abundant vasculature information than CDFI. As a result, PAI may have a great potential in diagnosis of thyroid cancers.

4. To perform 3D functional PA/US imaging, we proposed to scan the linear transducer across the imaged tissue and applied this method to the clinical study for the first time. For quantification analysis of 3D functional PA/US imaging results, algorithms were designed for segmentation of intra-tumor regions and peri-tumor regions and for calculation of volumetric mean SO_2 values of two regions. The statistical results demonstrate that 3D functional PA/US imaging has the great potential in differentiating benign tumors from early breast cancers.

5. The comparison between ARF-induced SAWs and laser-induced SAWs was performed for the first time. Specifically, the difference of bandwidths between ARF-induced SAWs and laser-induced SAWs was first investigated. Besides, generation of shear waves with laser excitation underneath the surface was also reported for the

first time.

7.2 The future of PA/US dual mode imaging in clinical applications

As a promising imaging technology, PA/US dual mode imaging has shown great potentials in diagnosis of diseases including cancers and arthritis. However, there are still several challenges to overcome before PA/US dual mode imaging can be applied widely in clinical environments. First of all, although physicians are very familiar with the operation of PA/US imaging based on handheld US imaging systems, the traditional US imaging transducer has a limited reception angle, and thus has a limited capability in acquiring PA signals from multiple angles. This limitation can be addressed by designing transducers with larger reception angles in the future. Second, when performing functional PA/US imaging, the knowledge of local fluence is essential for calculating concentrations of absorptive components inside tissues. However, the accurate calculation of local fluence depends highly on the knowledge of the optical properties of imaged tissues, which can vary a lot in different types of tissues. Although several methods have been proposed for extracting functional information such as SO_2 without knowing the optical properties of imaged tissues[121], they still need to be further verified in clinical studies. Furthermore, large-scale clinical studies based on PAI need to be carried out in more potential applications, such as detecting ovarian cancer and arthritis, which have shown promising results in preclinical studies. At last, the cost-effectiveness should also be considered based on the add-on value provided by PAI.

Without significant improvement from traditional modalities, it would be hard for hospitals or physicians to spend both of the time and financial resources on advancement of this technology. However, with the above aspects addressed, the author believes that PAI will become an indispensable imaging modality in the future just like other mature imaging modalities such as US, MRI, and CT.

Appendix A.1

Detailed information of 24 breast tumors

Detailed information of 24 breast tumours															
ID	Age	R/L[1]	Size(largest diameter,cm)	Pathologic diagnosis	Histological grade	ERα	PR	HER-2	ki-67	p53	EGFR	BI-RADS	SO_2 inside tumours	SO_2 in tumour surrounding regions	SO_2 in opposite healthy breasts
1	34	L	0.6	fibromas	~[2]	~	~	~	~	~	~	4a-4b	0.68	0.67	0.75
2	28	R	0.9	invasive breast cancer(carcinoma)	G2	90%	70%	1+	10%	+	0	4	0.68	0.72	0.68
3	48	L	1	invasive breast cancer(carcinoma)	G1	90%	90%	0	5%	-	-	4c	0.70	0.70	0.75
4	45	R	1	invasive breast cancer(carcinoma)	G1	80%	90%	1+	10%	+	-	4b-4c	0.75	0.75	0.72
5	31	L	1.1	fibromas	~	~	~	~	~	~	~	3-4a	0.81	0.74	0.72
6	37	R	1.1	fibromas	~	~	~	~	~	~	~	4a	0.83	0.78	0.75
7	52	L	1.2	invasive breast cancer(carcinoma)	G1	85%	80%	2+	15%	-	-	4b-4c	0.66	0.66	~
8	32	L	1.2	breast adenosis	~	~	~	~	~	~	~	3-4a	0.74	0.78	0.73
9	53	R	1.2	breast adenosis	~	~	~	~	~	~	~	4a	0.80	0.81	0.81
10	66	R	1.3	invasive breast cancer(carcinoma)	G2	90%	60%	0	10%	+	-	4c	0.62	0.75	0.81
11	31	R	1.5	fibromas	~	~	~	~	~	~	~	4a	0.84	0.80	0.79
12	58	R	1.5	invasive breast cancer(carcinoma)	G3	-	-	3+	30%	+	-	4c	0.70	0.69	0.74
13	44	L	1.6	invasive breast cancer(carcinoma)	G1	80%	90%	2+	5%	-	-	5	0.72	0.75	0.79
14	67	L	1.7	invasive breast cancer(carcinoma)	G3	90%	90%	0	12%	+	0	4c	0.74	0.77	0.76
15	50	R	1.7	invasive breast cancer(carcinoma)	G2	70%	80%	3+	60%	+	-	4c	0.75	0.73	0.73
16	49	L	1.7	invasive breast cancer(carcinoma)	G3	+	+	1+	20%	-	~	4b-4c	0.76	0.72	0.73
17	50	R	1.7	invasive breast cancer(carcinoma)	G2	95%	95%	0	5%	-	0	4b-4c	0.71	0.76	0.74
18	48	R	1.8	invasive breast cancer(carcinoma)	G2	80%	80%	1+	2%	+	~	4c	0.66	0.66	0.69
19	25	L	1.8	fibromas	~	~	~	~	~	~	~	3-4a	0.79	0.79	0.74
20	39	R	2	invasive breast cancer(carcinoma)	G2	85%	55%	2+	10%	-	+	5	0.68	0.73	~
21	30	L	2	fibromas	~	~	~	~	~	~	~	4b	0.71	0.78	0.77
22	34	L	2	invasive breast cancer(carcinoma)	G3	-	-	2+	75%	-	+	4c	0.69	0.75	0.69
23	55	L	2	invasive breast cancer(carcinoma)	G2	90%	-	1+	5%	+	-	5	0.71	0.70	0.77
24	47	L	2	invasive breast cancer(carcinoma)	G2	-	-	1+	60%	+	+	5	0.77	0.77	0.74

1: right/left

2: no data available

REFERENCES

[1] Bell A G. The production of sound by radiant energy. Science, 1881, 2(48): 242-253.

[2] Wang L V, Wu H-i. Biomedical optics: principles and imaging. 1st ed. New Jersey: John Wiley & Sons, 2012.

[3] Emelianov S, Aglyamov S, Karpiouk A *et al.* Synergy and applications of combined ultrasound, elasticity, and photoacoustic imaging. Skin, 2006, 102: 101.

[4] Wilson K E, Wang T Y, Willmann J K. Acoustic and photoacoustic molecular imaging of cancer. Journal of Nuclear Medicine, 2013, 54(11): 1851-1854.

[5] Chen Y-S, Frey W, Kim S *et al.* Silica-coated gold nanorods as photoacoustic signal nanoamplifiers. Nano Letters, 2011, 11(2): 348-354.

[6] Valluru K S, Willmann J K. Clinical photoacoustic imaging of cancer. Ultrasonography, 2016, 35(4): 267-280.

[7] Li C, Wang L V. Photoacoustic tomography and sensing in biomedicine. Physics in Medicine and Biology, 2009, 54(19): R59.

[8] Jacques S L. Optical properties of biological tissues: a review. Physics in Medicine and Biology, 2013, 58(11): R37.

[9] Kim J-w, Dang C V. Cancer's molecular sweet tooth and the Warburg effect. Cancer Research, 2006, 66(18): 8927-8930.

[10] Cairns R A, Harris I S, Mak T W. Regulation of cancer cell metabolism. Nature Reviews Cancer, 2011, 11(2): 85.

[11] Neuschler E I, Butler R, Young C A *et al.* A Pivotal Study of Optoacoustic Imaging to Diagnose Benign and Malignant Breast Masses: A New Evaluation Tool for Radiologists. Radiology, 2017: 172228.

[12] Vogel A, Venugopalan V. Mechanisms of pulsed laser ablation of biological tissues. Chemical reviews, 2003, 103(2): 577-644.

[13] Diot G, Metz S, Noske A *et al.* Multispectral optoacoustic tomography (MSOT) of human breast cancer. Clinical Cancer Research, 2017, 23(22): 6912-6922.

[14] Garcia-Uribe A, Erpelding T N, Krumholz A *et al.* Dual-modality photoacoustic and ultrasound imaging system for noninvasive sentinel lymph node detection in patients with breast cancer. Scientific Reports, 2015, 5: 15748.

[15] van den Berg P J, Daoudi K, Bernelot Moens H J *et al.* Feasibility of photoacoustic/ultrasound imaging of synovitis in finger joints using a point-of-care system. Photoacoustics, 2017, 8: 8-14.

[16] Kang J, Zhang H K, Rahmim A *et al.* Toward high-speed transcranial photoacoustic imaging using compact near-infrared pulsed LED illumination system. Photons Plus Ultrasound: Imaging and Sensing

2017, 10064: 100643B, San Francisco, 2017. International Society for Optics and Photonics, 2017.

[17] Ishihara M, Horiguchi A, Shinmoto H *et al.* Comparison of transrectal photoacoustic, Doppler, and magnetic resonance imaging for prostate cancer detection. Photons Plus Ultrasound: Imaging and Sensing 2016, 9708: 970852, San Francisco, 2016. International Society for Optics and Photonics, 2016.

[18] Deán-Ben X L, Razansky D. Functional optoacoustic human angiography with handheld video rate three dimensional scanner. Photoacoustics, 2013, 1(3-4): 68-73.

[19] Kim J, Park S, Jung Y *et al.* Programmable real-time clinical photoacoustic and ultrasound imaging system. Scientific Reports, 2016, 6: 35137.

[20] Dima A, Ntziachristos V. Non-invasive carotid imaging using optoacoustic tomography. Optics Express, 2012, 20(22): 25044-25057.

[21] Oeri M, Bost W, Sénégond N *et al.* Hybrid photoacoustic/ultrasound tomograph for real-time finger imaging. Ultrasound in Medicine and Biology, 2017, 43(10): 2200-2212.

[22] Jo J, Xu G, Cao M *et al.* A Functional Study of Human Inflammatory Arthritis Using Photoacoustic Imaging. Scientific Reports, 2017, 7(1): 15026.

[23] Irisawa K, Hirota K, Hashimoto A *et al.* Photoacoustic imaging system for peripheral small-vessel imaging based on clinical ultrasound technology. Photons Plus Ultrasound: Imaging and Sensing 2016, 9708: 970807, San Francisco, 2016. International Society for Optics and Photonics, 2016.

[24] Hai P, Zhou Y, Gong L *et al.* Quantitative photoacoustic elastography in humans. Journal of Biomedical Optics, 2016, 21(6): 066011.

[25] Choi W, Park E-Y, Jeon S *et al.* Clinical photoacoustic imaging platforms. Biomedical Engineering Letters, 2018, 8(2): 139-155.

[26] Taruttis A, Timmermans A C, Wouters P C *et al.* Optoacoustic Imaging of Human Vasculature: Feasibility by Using a Handheld Probe. Radiology, 2016, 281(1): 256-263.

[27] Knieling F, Neufert C, Hartmann A *et al.* Multispectral Optoacoustic Tomography for Assessment of Crohn's Disease Activity. The New England Journal of Medicine, 2017, 376(13): 1292.

[28] Buehler A, Kacprowicz M, Taruttis A *et al.* Real-time handheld multispectral optoacoustic imaging. Optics Letters, 2013, 38(9): 1404-1406.

[29] Becker A, Masthoff M, Jing C *et al.* Multispectral optoacoustic tomography of the human breast: characterisation of healthy tissue and malignant lesions using a hybrid ultrasound-optoacoustic approach. European Radiology, 2017, 28(2): 602-609.

[30] Ermilov S, Su R, Zamora M *et al.* Optoacoustic angiography of peripheral vasculature. Photons Plus Ultrasound: Imaging and Sensing 2012, 8223: 82230D, San Francisco, 2012. International Society for Optics and Photonics, 2012.

[31] Amidi E, Mostafa A, Nandy S *et al.* Classification of human ovarian cancer using functional, spectral, and imaging features obtained from in vivo photoacoustic imaging. Biomedical Optics Express, 2019, 10(5): 2303-2317.

[32] Okawa S, Sei K, Hirasawa T *et al.* In vivo photoacoustic imaging of uterine cervical lesion and its image

processing based on light propagation in biological medium. Photons Plus Ultrasound: Imaging and Sensing 2017, 10064: 100642S, San Francisco, 2017. International Society for Optics and Photonics, 2017.

[33] Heijblom M, Steenbergen W, Manohar S. Clinical photoacoustic breast imaging: the twente experience. IEEE Pulse, 2015, 6(3): 42-46.

[34] Manohar S, Kharine A, van Hespen J C *et al.* The Twente Photoacoustic Mammoscope: system overview and performance. Physics in Medicine and Biology, 2005, 50(11): 2543.

[35] Heijblom M, Piras D, Brinkhuis M *et al.* Photoacoustic image patterns of breast carcinoma and comparisons with Magnetic Resonance Imaging and vascular stained histopathology. Scientific Reports, 2015, 5: 11778.

[36] Toi M, Asao Y, Matsumoto Y *et al.* Visualization of tumor-related blood vessels in human breast by photoacoustic imaging system with a hemispherical detector array. Scientific Reports, 2017, 7: 41970.

[37] Kruger R A, Kuzmiak C M, Lam R B *et al.* Dedicated 3D photoacoustic breast imaging. Medical Physics, 2013, 40(11): 113301.

[38] Chuah S, Attia A, Long V *et al.* Structural and functional 3D mapping of skin tumours with non-invasive multispectral optoacoustic tomography. Skin Research and Technology, 2017, 23(2): 221-226.

[39] Lin L, Hu P, Shi J *et al.* Single-breath-hold photoacoustic computed tomography of the breast. Nature Communications, 2018, 9(1): 2352.

[40] Deán-Ben X L, Razansky D. On the link between the speckle free nature of optoacoustics and visibility of structures in limited-view tomography. Photoacoustics, 2016, 4(4): 133-140.

[41] Deán-Ben X L, Merčep E, Razansky D. Hybrid-array-based optoacoustic and ultrasound (OPUS) imaging of biological tissues. Applied Physics Letters, 2017, 110(20): 203703.

[42] Schwarz M, Buehler A, Ntziachristos V. Isotropic high resolution optoacoustic imaging with linear detector arrays in bi-directional scanning. Journal of Biophotonics, 2015, 8(1-2): 60-70.

[43] Wang Y, Wang D, Zhang Y *et al.* Slit-enabled linear-array photoacoustic tomography with near isotropic spatial resolution in three dimensions. Optics Letters, 2016, 41(1): 127-130.

[44] Wang Y, Wang D, Hubbell R *et al.* Second generation slit-based photoacoustic tomography system for vascular imaging in human. Journal of Biophotonics, 2017, 10(6-7): 799-804.

[45] Vallet M, Varray F, Kalkhoran M A *et al.* Enhancement of photoacoustic imaging quality by using CMUT technology: Experimental study. 2014 IEEE International Ultrasonics Symposium, 1296-1299, Chicago, 2014. IEEE, 2014.

[46] Plumb A A, Huynh N T, Guggenheim J *et al.* Rapid volumetric photoacoustic tomographic imaging with a Fabry-Perot ultrasound sensor depicts peripheral arteries and microvascular vasomotor responses to thermal stimuli. European Radiology, 2018, 28(3): 1037-1045.

[47] Yang M, Zhao L, He X *et al.* Photoacoustic/ultrasound dual imaging of human thyroid cancers: an initial clinical study. Biomedical Optics Express, 2017, 8(7): 3449-3457.

[48] American National Standards Institute, Laser Institute of America. American National Standard for Safe Use of Lasers. Laser Institute of America, 2014.

[49] Xu Y, Wang L V, Ambartsoumian G *et al.* Reconstructions in limited-view thermoacoustic tomography. Medical Physics, 2004, 31(4): 724-733.

[50] Yuan Z, Jiang H B. Quantitative photoacoustic tomography: Recovery of optical absorption coefficient maps of heterogeneous media. Applied Physics Letters, 2006, 88(23): 231101-231103.

[51] Kohl A, Daoudi K, Rabot O *et al.* Handheld probe integrating laser diode and ultrasound transducer array for ultrasound/photoacoustic dual modality imaging. Optics Express, 2014, 22(21): 26365-26374.

[52] Arridge S R. Optical tomography in medical imaging. Inverse Problems, 1999, 15(2): R41.

[53] Paulsen K D, Jiang H. Spatially varying optical property reconstruction using a finite element diffusion equation approximation. Medical Physics, 1995, 22(6): 691-701.

[54] Flock S T, Patterson M S, Wilson B C *et al.* Monte Carlo modeling of light propagation in highly scattering tissues. I. Model predictions and comparison with diffusion theory. IEEE Transactions on Biomedical Engineering, 1989, 36(12): 1162-1168.

[55] Wang L, Jacques S L. Hybrid model of Monte Carlo simulation and diffusion theory for light reflectance by turbid media. Journal of the Optical Society of America A, 1993, 10(8): 1746-1752.

[56] Duderstadt J J. Nuclear reactor analysis. 1st ed. New Jersey: Wiley, 1976.

[57] Zhao L, Yang M, Jiang Y *et al.* Optical fluence compensation for handheld photoacoustic probe: An in vivo human study case. Journal of Innovative Optical Health Sciences, 2017, 10(04): 1740002.

[58] Hale G M, Querry M R. Optical Constants of Water in the 200-nm to 200-μm Wavelength Region. Applied Optics, 1973, 12(3): 555-563.

[59] Sandell J L, Zhu T C. A review of in-vivo optical properties of human tissues and its impact on PDT. Journal of Biophotonics, 2011, 4: 773-787.

[60] Peters V, Wyman D, Patterson M *et al.* Optical properties of normal and diseased human breast tissues in the visible and near infrared. Physics in Medicine and Biology, 1990, 35(9): 1317.

[61] Haugen B R, Alexander E K, Bible K C *et al.* 2015 American Thyroid Association Management Guidelines for Adult Patients with Thyroid Nodules and Differentiated Thyroid Cancer: The American Thyroid Association Guidelines Task Force on Thyroid Nodules and Differentiated Thyroid Cancer. Thyroid, 2016, 26(1): 1-133.

[62] Cooper D S, Doherty G M, Haugen B R *et al.* Management guidelines for patients with thyroid nodules and differentiated thyroid cancer: The American Thyroid Association Guidelines Taskforce. Thyroid, 2006, 16(2): 109-142.

[63] Hegedus L. Clinical practice. The thyroid nodule. New England Journal of Medicine, 2004, 351(17): 1764-1771.

[64] Kim H, Kim J-A, Son E J *et al.* Quantitative assessment of shear-wave ultrasound elastography in thyroid nodules: diagnostic performance for predicting malignancy. European Radiology, 2013, 23(9): 2532-2537.

[65] Hornung M, Jung E M, Georgieva M *et al.* Detection of microvascularization of thyroid carcinomas using linear high resolution contrast-enhanced ultrasonography (CEUS). Clinical Hemorheology and Microcirculation, 2012, 52(2-4): 197-203.

[66] Turkoz F P, Solak M, Petekkaya I *et al.* Association between common risk factors and molecular subtypes in breast cancer patients. Breast, 2013, 22(3): 344-350.

[67] Desantis C E, Fedewa S A, Goding S A *et al.* Breast cancer statistics, 2015: Convergence of incidence rates between black and white women. CA: A Cancer Journal for Clinicians, 2016, 66(1): 31-42.

[68] Onega T, Beaber E F, Sprague B L *et al.* Breast cancer screening in an era of personalized regimens: a conceptual model and National Cancer Institute initiative for risk-based and preference-based approaches at a population level. Cancer, 2015, 120(19): 2955-2964.

[69] Teh W, Wilson A R. The role of ultrasound in breast cancer screening. A consensus statement by the European Group for Breast Cancer Screening. European Journal of Cancer, 1998, 34(4): 449.

[70] Carney P A, Miglioretti D L, Yankaskas B C *et al.* Individual and combined effects of age, breast density, and hormone replacement therapy use on the accuracy of screening mammography. Annals of Internal Medicine, 2003, 138(3): 168-175.

[71] Council N R. Mammography and beyond: developing technologies for the early detection of breast cancer. National Academies Press, 2001.

[72] Zackrisson S, van de Ven S M W Y, Gambhir S S. Light In and Sound Out: Emerging Translational Strategies for Photoacoustic Imaging. Cancer Research, 2014, 74(4): 979-1004.

[73] Beard P. Biomedical photoacoustic imaging. Interface Focus, 2011, 1(4): 602.

[74] Vaupel P, Kallinowski F, Okunieff P. Blood flow, oxygen and nutrient supply, and metabolic microenvironment of human tumors: a review. Cancer Research, 1989, 49(23): 6449-6465.

[75] Weidner N, Semple J P, Welch W R *et al.* Tumor angiogenesis and metastasis—correlation in invasive breast carcinoma. New England Journal of Medicine, 1991, 324(1): 1-8.

[76] Heijblom M, Piras D, Xia W *et al.* Visualizing breast cancer using the Twente photoacoustic mammoscope: What do we learn from twelve new patient measurements? Optics Express, 2012, 20(11): 11582-11597.

[77] Vaupel P, Schlenger K, Knoop C *et al.* Oxygenation of human tumors: evaluation of tissue oxygen distribution in breast cancers by computerized O2 tension measurements. Cancer Research, 1991, 51(12): 3316.

[78] Fakhrejahani E, Torii M, Kitai T *et al.* Clinical report on the first prototype of a photoacoustic tomography system with dual illumination for breast cancer imaging. PLOS One, 2015, 10(10): e0139113.

[79] Kolkman R G M, Brands P J, Steenbergen W *et al.* Real-time in vivo photoacoustic and ultrasound imaging. Journal of Biomedical Optics, 2008, 13(5): 3.

[80] Nandy S, Mostafa A, Hagemann I S *et al.* Evaluation of ovarian cancer: initial application of coregistered photoacoustic tomography and US. Radiology, 2018, 289(3): 740-747.

[81] Huang Y-H, Chen J-H, Chang Y-C *et al.* Diagnosis of solid breast tumors using vessel analysis in three-dimensional power Doppler ultrasound images. Journal of Digital Imaging, 2013, 26(4): 731-739.

[82] Fronheiser M P, Ermilov S A, Brecht H-P F *et al.* Real-time optoacoustic monitoring and three-dimensional mapping of a human arm vasculature. Journal of Biomedical Optics, 2010, 15(2): 021305.

[83] Gateau J, Caballero M Á A, Dima A *et al.* Three-dimensional optoacoustic tomography using a conventional ultrasound linear detector array: Whole-body tomographic system for small animals. Medical Physics, 2013, 40(1): 013302.

[84] Wang Y, Guo Z, Wang L V *et al.* In vivo three-dimensional photoacoustic imaging based on a clinical matrix array ultrasound probe. Journal of Biomedical Optics, 2012, 17(6): 061208.

[85] Prahl S. *Tabulated Molar Extinctin Coefficient for Hemoglobin in Water*, <https://omlc.org/spectra/hemoglobin/summary.html> (1998).

[86] Yang M, Zhao L, Yang F *et al.* Quantitative analysis of breast tumours aided by three-dimensional photoacoustic/ultrasound functional imaging. Scientific Reports, 2020, 10(8074).

[87] Cheng X, Mao J-m, Bush R *et al.* Breast cancer detection by mapping hemoglobin concentration and oxygen saturation. Applied Optics, 2003, 42(31): 6412-6421.

[88] Grosenick D, Wabnitz H, Moesta K T *et al.* Concentration and oxygen saturation of haemoglobin of 50 breast tumours determined by time-domain optical mammography. Physics in Medicine and Biology, 2004, 49(7): 1165.

[89] Luke G P, Yun N S, Emelianov S Y. Optical wavelength selection for improved spectroscopic photoacoustic imaging. Photoacoustics, 2013, 1(2): 36-42.

[90] Durduran T, Choe R, Culver J *et al.* Bulk optical properties of healthy female breast tissue. Physics in Medicine and Biology, 2002, 47(16): 2847.

[91] Cerussi A E, Berger A J, Bevilacqua F *et al.* Sources of absorption and scattering contrast for near-infrared optical mammography. Academic Radiology, 2001, 8(3): 211-218.

[92] Luke G P, Emelianov S Y. Label-free detection of lymph node metastases with US-guided functional photoacoustic imaging. Radiology, 2015, 277(2): 435-442.

[93] Todd M J, Yıldırım E A. On Khachiyan's algorithm for the computation of minimum-volume enclosing ellipsoids. Discrete Applied Mathematics, 2007, 155(13): 1731-1744.

[94] Tirumani S H, Shinagare A B, O'Neill A C *et al.* Accuracy and feasibility of estimated tumour volumetry in primary gastric gastrointestinal stromal tumours: validation using semiautomated technique in 127 patients. European Radiology, 2016, 26(1): 286-295.

[95] Vaupel P, Harrison L. Tumor hypoxia: causative factors, compensatory mechanisms, and cellular response. The Oncologist, 2004, 9: 4-9.

[96] Vaupel P, Briest S, Höckel M. Hypoxia in breast cancer: pathogenesis, characterization and biological/therapeutic implications. Wiener Medizinische Wochenschrift, 2002, 152(13-14): 334-342.

[97] Vaupel P, Kelleher D K, Höckel M. Oxygenation status of malignant tumors: pathogenesis of hypoxia and significance for tumor therapy. Seminars in oncology, 28: 29-35, 2001. WB Saunders, 2001.

[98] Liu H, Jiang Y-X, Liu J-B *et al.* Evaluation of breast lesions with contrast-enhanced ultrasound using the microvascular imaging technique: initial observations. The Breast, 2008, 17(5): 532-539.

[99] Matsubayashi R, Matsuo Y, Edakuni G *et al.* Breast masses with peripheral rim enhancement on dynamic contrast-enhanced MR images: correlation of MR findings with histologic features and expression of

growth factors. Radiology, 2000, 217(3): 841-848.

[100] Rossignol C, Rampnoux J-M, Perton M *et al.* Generation and detection of shear acoustic waves in metal submicrometric films with ultrashort laser pulses. Physical Review Letters, 2005, 94(16): 166106.

[101] Spicer J, McKie A, Wagner J. Quantitative theory for laser ultrasonic waves in a thin plate. Applied Physics Letters, 1990, 57(18): 1882-1884.

[102] Scruby C, Dewhurst R, Hutchins D *et al.* Quantitative studies of thermally generated elastic waves in laser-irradiated metals. Journal of Applied Physics, 1980, 51(12): 6210-6216.

[103] Monchalin J-P. Optical detection of ultrasound. IEEE Transactions on Ultrasonics Ferroelectrics and Frequency Control, 1986, 33: 485-499.

[104] Saavedra A C, Arroyo J, Zvietcovich F *et al.* In vivo estimation of the Young's modulus in normal human dermis. 40th Annual International Conference of the IEEE Engineering in Medicine and Biology Society (EMBC), 3456-3459, Honolulu, 2018. IEEE, 2018.

[105] Kirby M A, Pelivanov I, Song S *et al.* Optical coherence elastography in ophthalmology. Journal of Biomedical Optics, 2017, 22(12): 121720.

[106] Li C, Guan G, Zhang F *et al.* Laser induced surface acoustic wave combined with phase sensitive optical coherence tomography for superficial tissue characterization: a solution for practical application. Biomedical Optics Express, 2014, 5(5): 1403-1418.

[107] Li C, Guan G, Huang Z *et al.* Noncontact all-optical measurement of corneal elasticity. Optics Letters, 2012, 37(10): 1625-1627.

[108] Dupps W J. Biomechanical modeling of corneal ectasia. Journal of Refractive Surgery, 2005, 21(2): 186-190.

[109] Liu C-H, Nevozhay D, Zhang H *et al.* Longitudinal elastic wave imaging using nanobomb optical coherence elastography. Optics Letters, 2019, 44(12): 3162-3165.

[110] Zhang X, Yin Y, Guo Y *et al.* Measurement of quantitative viscoelasticity of bovine corneas based on lamb wave dispersion properties. Ultrasound in Medicine and Biology, 2015, 41(5): 1461-1472.

[111] Zhu J, Qi L, Miao Y *et al.* 3D mapping of elastic modulus using shear wave optical micro-elastography. Scientific Reports, 2016, 6: 35499.

[112] Zhu J, Qu Y, Ma T *et al.* Imaging and characterizing shear wave and shear modulus under orthogonal acoustic radiation force excitation using OCT Doppler variance method. Optics Letters, 2015, 40(9): 2099-2102.

[113] Sarvazyan A P, Rudenko O V, Nyborg W L. Biomedical applications of radiation force of ultrasound: historical roots and physical basis. Ultrasound in Medicine and Biology, 2010, 36(9): 1379-1394.

[114] Grasland-Mongrain P, Lu Y, Lesage F *et al.* Generation of shear waves by laser in soft media in the ablative and thermoelastic regimes. Applied Physics Letters, 2016, 109(22): 221901.

[115] Zhao L, Vanderlaan D, Yoon H *et al.* Ultrafast ultrasound imaging of surface acoustic waves induced by laser excitation compared with acoustic radiation force. Optics Letters, 2020, 45(7): 1810-1813.

[116] Yoon H, Zhu Y I, Yarmoska S K *et al.* Design and Demonstration of a Configurable Imaging Platform for Combined Laser, Ultrasound, and Elasticity Imaging. IEEE transactions on Medical Imaging, 2018.

[117] Zvietcovich F, Yao J, Rolland J P *et al.* Experimental classification of surface waves in optical coherence elastography. Optical Elastography and Tissue Biomechanics III, 9710: 97100Z, San Francisco, 2016. International Society for Optics and Photonics, 2016.

[118] Su J L, Karpiouk A B, Wang B *et al.* Photoacoustic imaging of clinical metal needles in tissue. Journal of Biomedical Optics, 2010, 15(2): 021309.

[119] Zvietcovich F, Rolland J P, Parker K J. An approach to viscoelastic characterization of dispersive media by inversion of a general wave propagation model. Journal of Innovative Optical Health Sciences, 2017, 10(06): 1742008.

[120] Royston T J, Dai Z, Chaunsali R *et al.* Estimating material viscoelastic properties based on surface wave measurements: A comparison of techniques and modeling assumptions. The Journal of the Acoustical Society of America, 2011, 130(6): 4126-4138.

[121] Tzoumas S, Nunes A, Olefir I *et al.* Eigenspectra optoacoustic tomography achieves quantitative blood oxygenation imaging deep in tissues. Nature Communications, 2016, 7: 12121.